5-1-2014

ATOMISTIC MODELING OF PHONON BANDSTRUCTURE AND TRANSPORT FOR OPTIMAL THERMAL MANAGEMENT IN NANOSCALE DEVICES

Sasi Sekaran Sundaresan
Southern Illinois University Carbondale, sasi@siu.edu

ATOMISTIC MODELING OF PHONON BANDSTRUCTURE AND TRANSPORT FOR OPTIMAL THERMAL MANAGEMENT IN NANOSCALE DEVICES

By

Sasi Sekaran Sundaresan

B.E., Anna University, 2008
M.S., Southern Illinois University, 2010

A Dissertation
Submitted in Partial Fulfillment of the Requirements for the
Doctor of Philosophy Degree

Department of Electrical and Computer Engineering
in the Graduate School
Southern Illinois University Carbondale
May, 2014

DISSERTATION APPROVAL

ATOMISTIC MODELING OF PHONON BANDSTRUCTURE AND TRANSPORT FOR OPTIMAL THERMAL MANAGEMENT IN NANOSCALE DEVICES

By

Sasi Sekaran Sundaresan

A Dissertation Submitted in Partial

Fulfillment of the Requirements

for the Degree of

Doctor of Philosophy Degree

in the field of Electrical and Computer Engineering

Approved by:

Dr. Shaikh Ahmed, Chair

Dr. Haibo Wang

Dr. Mohammed Sayeh

Dr. Ada Chen

Dr. Thushari Jayasekera

Graduate School
Southern Illinois University Carbondale
March 3rd 2014

AN ABSTRACT OF THE DISSERTATION OF

Sasi Sekaran Sundaresan, for the Doctor of Philosophy degree in ELECTRICAL AND COMPUTER ENGINEERING, presented on 11/25/2013, at Southern Illinois University Carbondale.

TITLE: ATOMISTIC MODELING OF PHONON BANDSTRUCTURE AND TRANSPORT FOR OPTIMAL THERMAL MANAGEMENT IN NANOSCALE DEVICES

MAJOR PROFESSOR: Dr. Shaikh Shahid Ahmed

Monte Carlo based statistical approach to solve Boltzmann Transport Equation (BTE) has become a norm to investigate heat transport in semiconductors at sub-micron regime, owing mainly to its ability to characterize realistically sized device geometries qualitatively. One of the primary issues with this technique is that the approach predominantly uses empirically fitted phonon dispersion relations as input to determine the properties of phonons so as to predict the thermal conductivity of specified material geometry. The empirically fitted dispersion relations assume harmonic approximation thereby failing to account for thermal expansion, interaction of lattice waves, effect of strain on spring stiffness, and accurate phonon-phonon interaction. To circumvent this problem, in this work, a coupled *molecular mechanics-Monte Carlo (MM-MC) platform* has been developed and used to solve the phonon Boltzmann Transport Equation (BTE) for the calculation of thermal conductivity of several novel and emerging nanostructures. The use of the quasi-anharmonic MM approach (as implemented in the open source NEMO 3-D software toolkit) not only allows one to capture the true *atomicity* of the underlying lattice but also enables the simulation of realistically-sized structures containing *millions of atoms*. As compared to the approach using an empirically fitted phonon dispersion relation, here, a 17% increase in the thermal conductivity for a silicon nanowire due to the incorporation of

atomistic corrections in the LA (longitudinal acoustic) branch alone has been reported. The atomistically derived thermal conductivity as calculated from the MM-MC framework is then used in the modular design and analysis of (i) a silicon nanowire based *thermoelectric cooler* (TEC) unit, and (ii) a GaN/InN based nanostructured light emitting device (LED). It is demonstrated that the use of empirically fitted phonon bandstructure parameters overestimates the temperature difference between the hot and the cold sides and the overall cooling efficiency of the system, thereby, demanding the use of the BTE derived thermal conductivity in the calculation of thermal conductivity. In case of the light-emitting device, the microscopically derived material parameters, as compared to their bulk and fitted counterparts, yielded ~3% correction (increase) in optical efficiency. A non-deterministic approach adopted in this work, therefore, provides satisfactory results in what concerns phonons transport in both ballistic and diffusive regimes to understand and/predict the heat transport phenomena in nanostructures.

DEDICATION

This work is dedicated to my Mom (S. Nirmala), Dad (S.K. Sundaresan), Family, Friends and all people who have influenced and supported me. Also I would like to dedicate this work to “Kavipperarasu” Vairamuthu, whose words have inspired me all along.

ACKNOWLEDGMENTS

I wish to express my sincere thanks and gratitude to my research advisor, Professor Shaikh Ahmed, but for whom this would not have been possible today. He has bestowed exceptional guidance and has been a beacon of light all through my difficult times. It was from him that I learnt on how to think and approach a problem.

I would like to thank my committee members Professor Haibo Wang, Professor Mohammed Sayeh, Professor Ada Chen and Professor Thushari Jayasekera for their time and interest in this work. I would like to thank all my colleagues at the Nano-electronics Research Group at Southern Illinois University Carbondale.

I would like to acknowledge the U.S. National Science Foundation (NSF Grant # 1218839) for the financial support.

I would like to thank Heidi Jung, JP Dunn and Howard Carter for supporting all through my academic years. I would specially like to thank Heidi Jung and Eric Jung for all love, affection and encouragement they have given me and making me feel at home.

I would like to thank Dr. Philomin Raj, HOD at MCC, Chennai for his guidance throughout my undergrad days. I would specially like to thank Mr. Saravanan Ponraj, CEO Kalorful Industries., for what I am today and Mr. Savari Jeffrey Roshan, CEO Mariyano Technologies., for who I am today. I would also like to thank Mrs. Geethalakshmi for all her encouragement. I would like to thank Deepika, Guru, Lavanya, Saravanan, Jeffrey, Pradeep, Vijay, Navdeep, Arun, Dinesh, Karthik, Deepak, Naren, Daniel, Jayanth, Ram, Sai, Rashmita, Mallika, Devika, Julian and Prabhakar for their unconditional love and support.

TABLE OF CONTENTS

LIST OF TABLES

LIST OF FIGURES

CHAPTER 1

INTRODUCTION

The unceasing hunger to pack more transistors on a single chip has resulted in an unprecedented level of power dissipation, and therefore soaring temperatures at the chip level. The semiconductor device size reduction beyond the sub-micrometer range leads to unique electrical and thermal phenomena, causing non-equilibrium heat generation within the system [1]. Heat conduction in crystalline dielectric solids (which include most semiconductor materials) is primarily characterized by lattice vibrations that results in traveling waves of various frequencies and velocities thereby causing energy transport in the solids. From a quantum mechanical view point, these quantized modes of vibrations occurring in rigid crystal lattice are described as discrete energy packets, called phonons.

The phonon transport in micro or nanostructures are strongly influenced by interfaces and boundaries of the confining structure that leads to significant reduction in thermal conductivity. The diminished thermal conductivity significantly impedes heat spreading in electronic and opto-electronics devices at micro or nano scales, imposing challenges to thermal management (Garimella et al., 2008). On contrary such size effects have been exploited to develop nanostructured bulk materials with better thermoelectric (TE) performance (Hsu et al., 2004; Poudel et al., 2008; Ma et al., 2008; Wang et al., 2008; Joshi et al., 2008; Yang et al., 2009; Zhu et al., 2009) [61]. Hence it is important to understand the effects of thermal conductivity in both *(a) Thermal Management*; and *(b) Thermoelectrics*.

1.1 Thermal Management

Mainstream microelectronics has been powered by Moore's Law (the number of transistors on a chip doubles every 18 to 24 months) for the past 4-5 decades, driving ICs down to 22nm and below, and promising lower costs for chip makers. Today's semiconductor devices are diversified by varied applications such as computing and communication devices, radio frequency (RF) devices, optoelectronic devices, power management subsystems, passive components, biochips, sensors, actuators, micro-electromechanical systems (MEMS), etc [3]. The need for integrating more transistors in a chip exponentially increases leading us from Moore's law to 'More-than-Moore' approach. 'More-than-Moore' approach typically allows for the integration of such non-digital functionalities to migrate from the system board level into a particular package-level (SiP) or chip-level (SoC) implementation to enable cost-optimized and value-added system solutions

With the advent of technological innovation leading to shrinking transistor size, significant benefits in the form of higher integration density, higher performance, and lower cost are observed [11] [12]. Figure 1.1 extrapolates the transistor density in Intel series of microprocessors over the years. The exponential growth in transistor density and relentless down scaling of transistor sizes, pose severe design challenges and concerns due to excessive power consumption (power density) and associated thermal problems are observed especially in case of high-performance microprocessors [13] [14]. Also some of the low-level effects which were previously considered second-order and were traditionally invisible have now surfaced to become primary concerns.

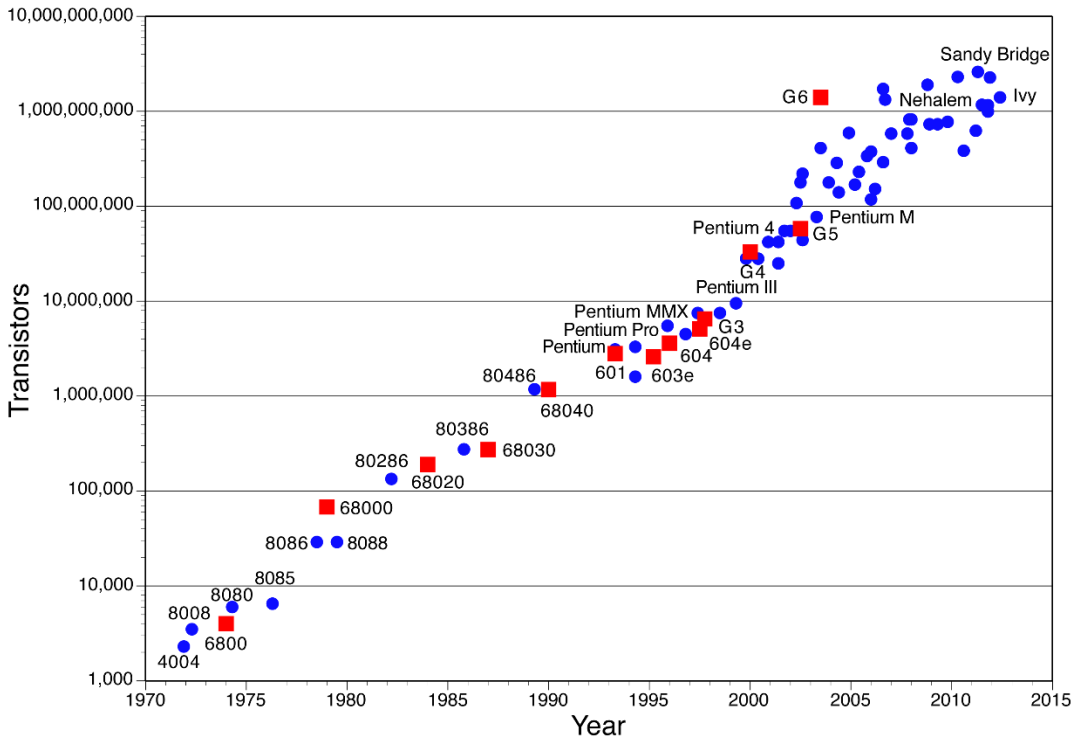

Figure 1.1 illustrates the increase in transistor density for Intel series of processors over the years

Since the transistor densities were directly proportional to power dissipation, the heat flux densities began to rival the nuclear reactor and rocket nozzle temperatures. This can be better understood from Figure 1.2 which illustrates the proportional increase in transistor density, clock speed and power density for Intel family of processors over the years. Majority of energy consumed by a microprocessor/System-on-Chip (SoC's) is dissipated as heat due to the resistive behavior of the processor/SoC circuits. The on chip temperature, which is a measure of the amount of heat energy stored in it, is directly related to the power density [4].

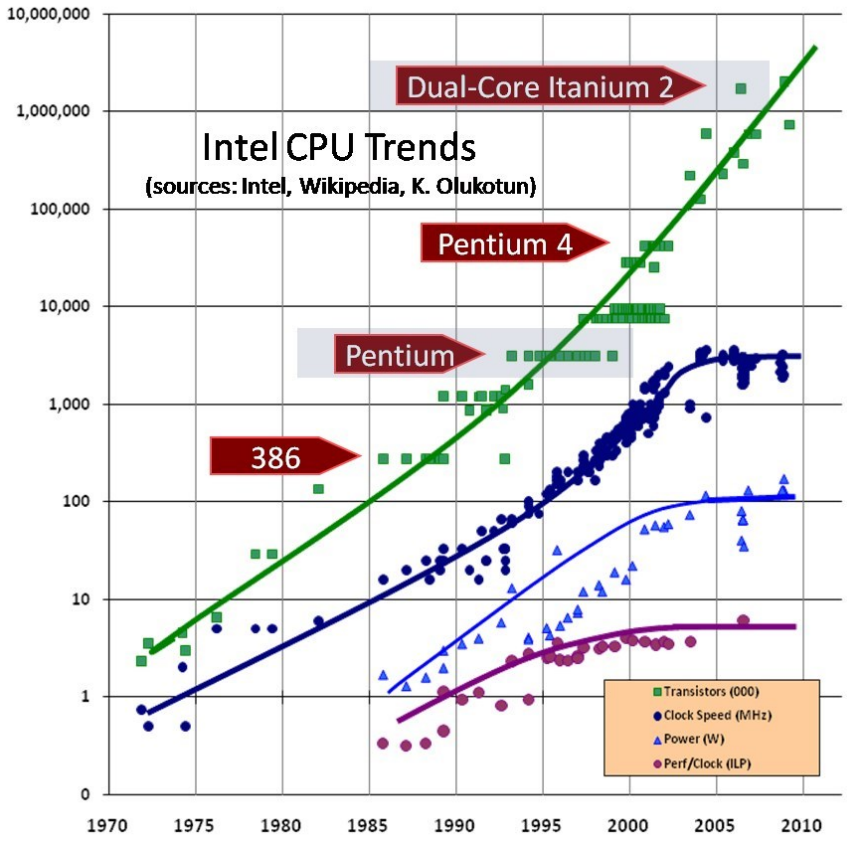

Figure 1.2 illustrates the proportional increase in transistor density, Clock speed and power density over the years [6].

Predictions of International Technology Roadmap for Semiconductors (ITRS) [6] for silicon technology in the near future is tabulated in Table 1.1. Despite the switching energy decreasing with scaling (Figure 1.3 (a)), and only considering switching power, average power density continues to increase as illustrated in Figure 1.3 (b). As the capability for system level heat removal is limited the projected allowable maximum power density (shown in Table 1.1) is approaching saturation [11].

Year of Production	2007	2010	2013	2016	2019
	Planar Bulk		Double Gate		
Supply Voltage (V)	1.1	1.0	0.9	0.8	0.7
[1]Transistor (M)	1106	2212	4424	8848	17696
[2]Size (mm^2)	310	310	310	310	310
[3]L_g (nm)	25	18	13	9	6
[4]$I_{d,sat}$ (μA/μm)	1200	2050	2220	2713	2744
[5]$I_{sd,\ leakage}$ (μA/μm)	0.2	0.28	0.11	0.11	0.11
[6]Intrinsic Delay, τ (ps)	0.64	0.40	0.25	0.15	0.10
[7]Switching Energy (fJ)	0.0634	0.0447	0.0198	0.0091	0.0036
[8]Max. P.D. (W/cm^2)	60.97	63.87	63.87	63.87	63.87

[1]Functions per chip at production (million transistors)
[2]Chip size at production (mm^2)
[3]Physical gate length (nm)
[4]Effective saturation drive current (μA/μm)
[5]Source/Drain subthreshold off-state leakage current (μA/μm)
[6]Intrinsic transistor delay for NMOS devices at 25°C (ps)
[7]Energy per device switching transition with dimensions W/L_g=3 (fJ/device)
[8]Maximum allowable average power density (W/cm^2)

Table 1.1 illustrates the high-performance logic technology trend targets [10] [11] [15]

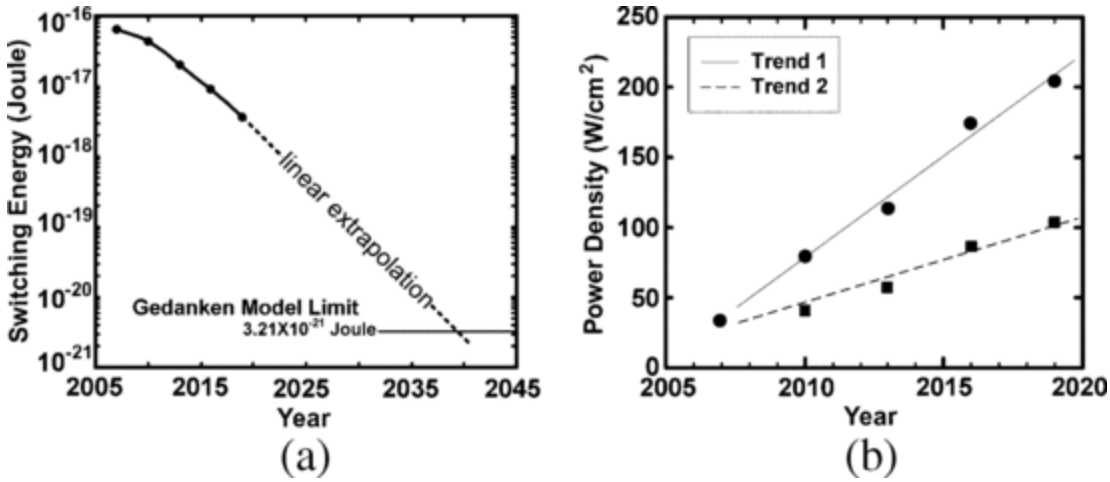

Figure 1.3(a) Trend of minimum transistor switching energy
(b) Trend of IC power density (Trend 1) with ITRS projected integration density and performance.

1.1.1 Temperature Driven Issues

Temperature not only affects the electrical functionality and performance of semiconductor devices, it also adversely affects the reliability of the semiconductor

devices. A variety of undesirable effects are associated with increase in die temperature. Though *catastrophic failure* such as the melting of the chip is a possibility, it is not often observed with today's device temperatures [4]. In reality, more significant reasons are in the form of increased leakage power and mobility degradation due to self-heating of the device and interconnects. In case of solid state lighting devices, the increase in phosphor's temperature affects the yield of quantum efficiency and thus the lumen output. Also *current crowding* and high crystal defect densities are observed due to temperatures at high voltages.

Some of the primary thermally-induced reliability concerns for transistors are: (1) Heat induced degradation of device terminal characteristics, (2) Failure due to the electrostatic discharge phenomenon, (3) Stresses induced by varying thermal expansion of different transistor constituents, and (4) Damage of metallic interconnects due to electro-migration where the atoms diffuse along a metal interconnect in the presence of a bias current [75].

Transistors exhibit static power dissipation, since they consume power even when they are idle and not switching. Even at these inactive conditions, the power dissipation can amount to a significant fraction (> 30%) of the total power consumption at current feature sizes which varies exponentially with respect to temperature. As temperature itself depends on the power consumption and the power consumption depends on the transistor density, there exists a circular dependence between them. In extreme cases, this can result in a self-reinforcing positive feedback loop that leads to thermal runaway [4]. Figure 1.4 illustrates the power consumption of Intel *Core i7* processors at active and idle states.

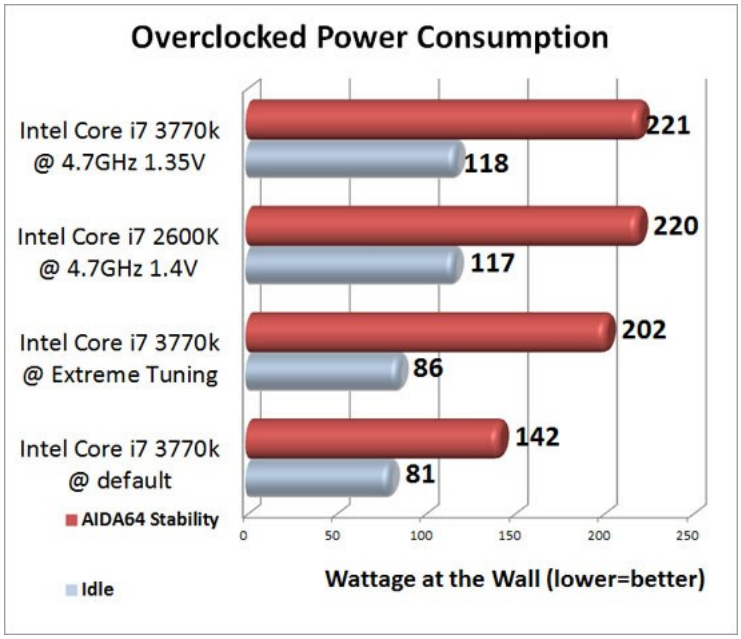

Figure 1.4 shows the power consumption of current Intel i7 processors during active and idle states [7].

In addition to switching power, thermal problems are further complicated due to leakage power which forms a significant fraction of total chip power consumption [16]. Major contribution to leakage in nanoscale CMOS comes from sub-threshold leakage, which is highly temperature sensitive [17]. Rapid scaling demands reduction in the threshold voltage since power consumption is converted into heat, operating temperature rises, which significantly increases subthreshold leakage. Also, threshold voltage decreases with temperature and results in even higher subthreshold leakage [11] [16]. Switching and static power consumption can be modeled as stated in Equation 1.1 and 1.2 [11].

$$P_{switching} = \propto C_{eff} {V_{dd}}^2 f \quad (1.1)$$

$$P_{leakage} = I_0 e^{-V_{th}/\gamma S}(1 - e^{-V_{ds}/\gamma S}) W_{eff} V_{dd} \quad (1.2)$$

Where □ is the switching activity factor, C_{eff} represents the total effective output-load capacitance of the circuit, and *f* denotes operating frequency. I_0 represents the nominal leakage current, W_{eff} is effective transistor width (transistor width that contributes to the leakage current) of the entire chip, V_{ds} is drain to source voltage, *S* is the sub-threshold swing and *γ* is a device parameter [11] [17].

Novel architectures such as SOI devices exhibit self-heating effects [8] [9]. The thermal conductivity of the buried oxide layer located beneath the thin active silicon layer, is100 times smaller than the thermal conductivity of bulk silicon, and hence it impedes the heat removal from the active devices to the heat sink. Thus, heat removal tends to be much more difficult in the active devices considering the fact that self-heating occurs in the SOI transistors. These aforementioned phenomena result in dramatic deterioration of transistor switching performance due to decrease of on-currents and increase of off-currents, thereby reducing the overall circuit performance. Also, the thermal conductivity of the thin silicon film decreases due to phonon boundary scattering which again complicates the heat removal process [75].

In case of logic circuits, such as microprocessors, the power is non-uniformly distributed resulting in portions of the chip dissipating less power (memory blocks) compared to the some other portions of the chip where the underlying local blocks are running at full speed with high activity factors. At these active spots the power density tends to be more than a magnitude higher than the average chip power density. The active portions results in hot spots with quite high local temperature. Thus, the treatment of self-heating and the realistic estimation of the power density turns out to be quite a

complex task [75].

The thermal management issues are not only restricted to electronic devices, they influence optoelectronic devices even more adversely. The efficiency of solid state lighting devices (SSLs) strongly depend on the junction temperature (Figure 1.5). Increase in junction temperature mitigates the overall efficiency of the device, reduces the forward voltage, causes the emission to shift to longer wavelengths, and reduces the device lifetime and reliability. Since LED involves opto-thermo-electro-mechanical coupling addressing the effects due to temperature becomes more complex.

1.1.2 Classification of Thermal Management

Thermal management can be classified based on the level at which the heat removal process is directed to. Primarily thermal management is broadly addressed in 3 different levels namely, system level, circuit level and device level. The system level deals with employing efficient and cheaper heat removal systems such as heat sinks, cooling fans and water based cooling solutions.

In order to evaluate system performance electro-thermal couplings, junction temperature, and associated cooling power needs to be accounted for [18].

Figure 1.5 shows that the chip power ($P_{chip} = P_{switching} + P_{leakage}$) decreases as more cooling is applied, mainly as a result of decreasing leakage power. The decrease in total system power is valid only as long as the savings in chip power dissipation remains greater than the additional power required for cooling.

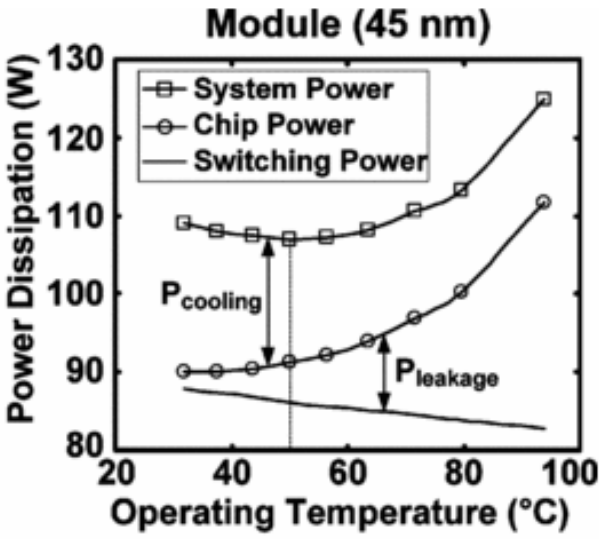

Figure 1.5 plots the power dissipation trends for system and chip power. A minimum system power for 45 nm technology is determined at ~50 C beyond which further cooling does not lead to any power saving.

ITRS [10] projects a very flat trend for air cooling capacity even in the long term and hence there isn't much room to increase the thermal management efficiency at system level.

The *circuit level thermal management* deals with architectural and micro-architectural thermal solutions. This involves employing better *scheduling algorithms* to distribute heat evenly throughout the chip by interleaving hot and cold processes in both time and space, employing multicore processors with the aim of availing spare cores to run the application, introducing novel compiler design approaches that distributes computation such that power density is minimized. But these techniques involve a trade off with space or operation time and temperature. As the chip transistor density and the application requirements sore to new heights the circuit level techniques do not offer an optimized solution for thermal management.

The *device level thermal management* aims at addressing the thermal issues

more fundamentally, it deals with reducing leakage currents or off currents thereby reducing heat generation, employing the use of materials with high thermal conductivities (k) so as to allow faster heat dissipation and numerous other possibilities. From the previous discussion it is clear that reducing the threshold voltage (V_{TH}) reduces the sub-threshold leakage thereby power dissipation and heat. Novel device architectures such as *Tunnel Transistor* can be employed to reduce leakage current. In case of LED thermal resistance is decreased to reduce self-heating. Nanostructures offer a new way of controlling phonon transport by tuning its dispersion relation, which is often referred to as phonon engineering. The concept of engineering the phonon dispersion in nanostructures is analogous to bandgap engineering for electrons, which revolutionized the electronic industry [45]. The use of thermo-electric coolers, hot spot cooling and phonon engineering promises effective heat removal from the device.

1.1.3 Market Trend

Thermal management in this context refers to the various tools and technologies deployed within electronic devices for temperature regulation purposes. The growth of the thermal management industry closely follows the development of technology in the semiconductor, microprocessor, and computer industries. For every advance in the performance of these systems, there is a corresponding increase in the operating heat generated by the system. The commercial market for these technologies involve thermal management hardware (e.g., fans, blowers, heat sinks); thermal management software (e.g., computational fluid design (CFD), computational heat transfer (CHT), power management, circuit design, and other electronic design automation (EDA);

thermal management interface products and thermal management substrates [20]. The world market for thermal management products has grown from about $6.9 billion in 2009 to $7.5 billion in 2010 and is predicted to grow to $10.2 billion by 2015, with a compound annual growth rate (CAGR) of 6.4% between 2010 and 2015 as illustrated in Figure 1.6 [19]. Of these thermal management hardware, holds over 84% of the market and other products such as interface, software and substrate technologies are worth approximately 5% each [20].

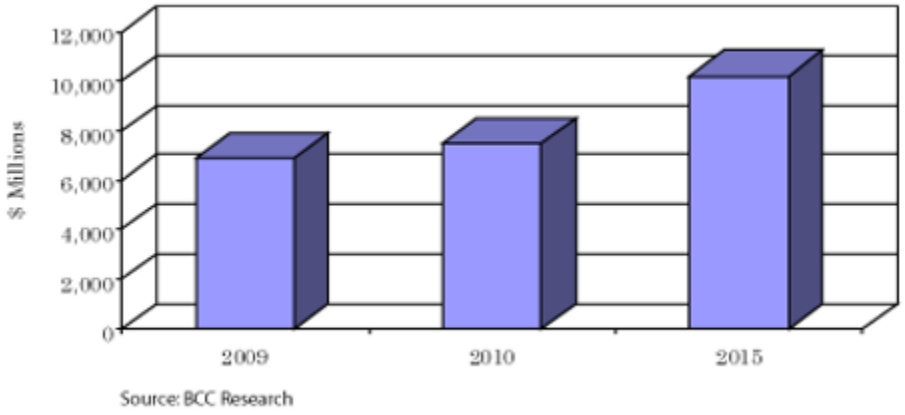

Figure 1.6 illustrates the world thermal management market trends between 2009 and 2015 [19]

1.2 Thermoelectrics

Thermoelectric materials interconvert thermal gradients and electric fields for solid-state cooling and power generation [21]. Thermo-electrics are promising in potential applications such as waste-heat recovery, power generators, air conditioning, and refrigeration. The efficiency of thermoelectric devices is quantified by the materials' dimensionless figure-of-merit, ZT (Equation 1.3), where Z is a measure of a material's thermoelectric properties and T is the absolute temperature [21] [25].

$$ZT = \left(\frac{S^2\sigma}{k}\right) T \tag{1.3}$$

Where S, σ, k are the Seebeck coefficient, electrical conductivity, and thermal conductivity, respectively. Many different material systems exhibit enhanced figures of merit of ZT > 1, as shown in Figure 1.7 [23]. Most of the materials trended in Figure 1.7 have broken the ZT ≈ 1 barrier which was the maximum ZT of any material for over fifty years [23].

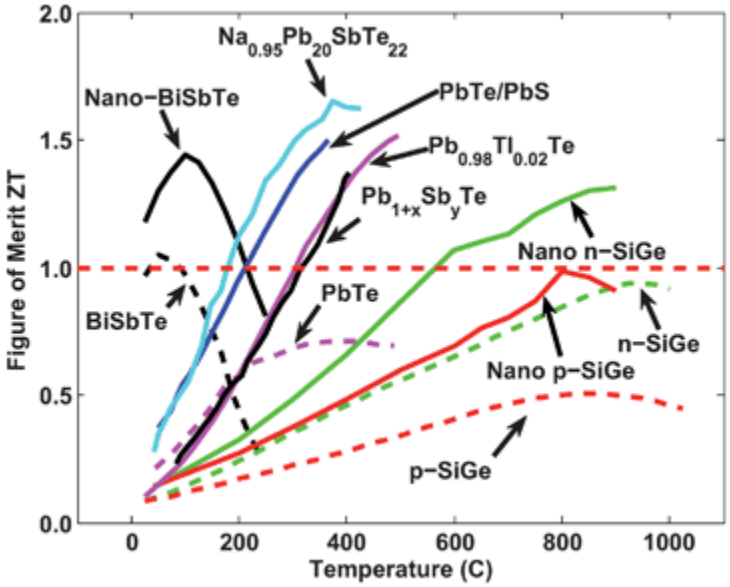

Figure 1.7 illustrates the figure of merit ZT of current state of the art thermoelectric materials as a function of temperature. Also seen from the figure is most of the alloyed materials breaching the ZT ~ 1 barrier.

The underlying principles for a thermoelectric power generator and thermoelectric cooler is governed by the Seeback effect and the Peltier effect respectively. The Seeback effect is associated with generation of voltage due to diffusion of charged carriers along a conductor when subjected to temperature difference. The Seeback effect is quantified by a Seeback co-efficient, S as dictated by

Equation 1.4.

$$S = -\frac{\Delta V_{12}}{\Delta T_{12}} \tag{1.4}$$

On contrary the Peltier effect is associated with creating a temperature difference along a conductor when subjected to a voltage difference. On applying a voltage difference the charge carriers transport heat when they flow from one end to another end. Similar to Seeback effect, Peltier effect is quantified by a Peltier co-efficient, Π as dictated by Equation 1.5.

$$\Pi = T.\frac{\Delta V_{12}}{\Delta T_{12}} \tag{1.5}$$

Both industry and research eyes on solid state TE devices owing to their enviable advantages such as (i) compactness, (ii) resistance to wear and tear, (iii) portability, (iv) no moving parts, (v) no emissions of toxic gases, (vi) low maintenance, and (vii) high reliability [29]. Thermoelectric efficiency (ZT) improvements require meticulous engineering designs and optimization in terms of, (i) materials [23], (ii) structures like superlattices, nanocomposities, etc. [22] [26], and (iii) devices [27] [28].

1.2.1 Challenges

For the past five decades the maximum figure of merit (ZT) for any material has been around unity, despite several breathtaking efforts and investing over millions of dollars in research there has been only modest progress in finding materials with enhanced ZT values at room temperature [25]. Maximizing ZT is quite challenging since all its parameters are interdependent such that optimizing one physical parameter often

adversely affects another [21]. Enhancement of ZT requires a high Seebeck coefficient, an increased electrical conductivity, and a decreased thermal conductivity, but these materials properties often counter each other [29]. For instance TE coolers with ZT of 1 operate with a *Carnot efficiency* of 10%, but with a slight increase in ZT from 1 to 4 could scale the Carnot efficiency to 30% (comparable to home refrigeration) which has remained a formidable challenge [30].

Another prime field of challenge in parallel to material development is device design. The efficiency of a TE device as compared to its stated material efficiency is always less owing to the *parasitic losses* in the device [22]. Hence extensive care needs to be asserted, while accounting for the contact and junction resistances. Issues like thermal mechanical stress, diffusion and the chemical reaction of materials at their interfaces creep in as the device operates under a large temperature difference. Secondly, the choice of the electrode materials are limited due to the requirement of very low electrical contact resistances for the electrodes owing to high electrical conductivities of TE materials. Also due to the fact that the thermoelectric devices operate under large currents and a large temperature gradient, both electrical and thermal migration are prone to occur [22].

1.2.2 Market Trend

Applications of thermoelectric devices are distributed into 2 major categories namely, thermoelectric refrigeration and thermoelectric power generation. In case of thermoelectric refrigeration the prime areas of application involves mobile refrigerators, cooled car seats, temperature regulators of semiconductor lasers, medical and scientific

instruments [22]. Currently, the world market for TE cooling devices is still limited of about $80 million to $160 million per year [30]. In case of power generation, thermoelectric generators have demonstrated their use in space applications, body temperature powered watches, vehicle waste heat recovery etc. Vehicle waste heat recovery has been a major driver for thermoelectric power generation since automobiles have efficiencies only around 20%. Figure 1.8 outlines the market trend for thermoelectric generators for the past 3 years. Figure 1.8 shows how the interest in wireless sensor applications has found a new niche market for these types of generators in recent years. Interest in consumer applications is expected to increase but still the dominant market remains as military and aerospace applications [31].

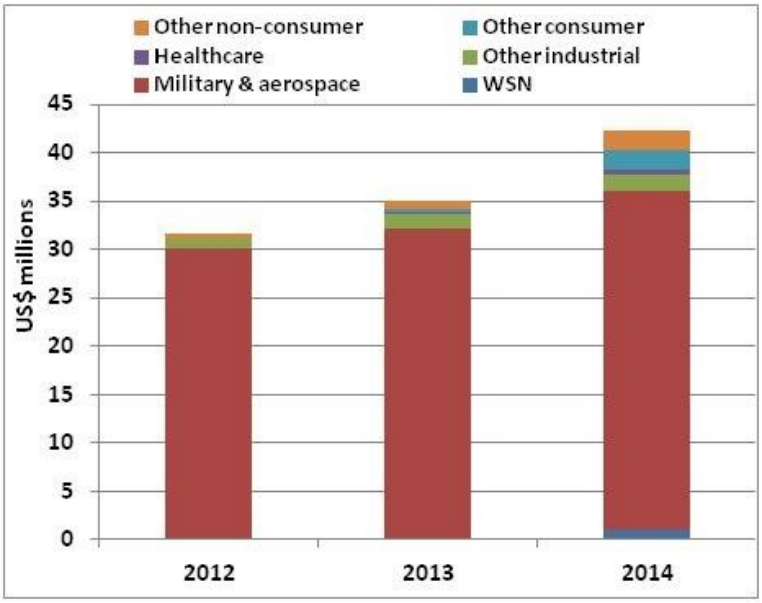

Figure 1.8 shows the US market trend on application basis for thermoelectric power generators

1.3 Engineering Thermal Conductivity

Selective modification of material properties using lower dimensional structures was introduced by Hicks and Dresselhaus in 1993 [23]. The use of low dimensional

(two-, one-, or even zero) structures significantly increased the electronic properties. Similarly the low dimensional structures promise significant reduction in lattice thermal conductivity which proved to aid the thermoelectric applications [23]. Phonon transport in micro/nanostructures is strongly influenced by interfaces and boundaries and hence leads to reduction in thermal conductivity (Cahill et al., 2003; Chen, 2005; McConnell & Goodson, 2005) [61]. This mitigation in thermal conductivity can significantly impede heat spreading in microelectronic and photonic devices, creating challenges to thermal management (Garimella et al., 2008). On the contrary, the reduction in thermal conductivity due to size effects helps to improve the performance of thermoelectric devices [61].

In case of phonon transport along the boundaries, the roughness of the boundaries can be engineered to decrease or increase the thermal conductivity. If the interface is rough the phonon undergo boundary scattering and thereby result in reduced thermal conductivity [24]. The roughness in the interface can be introduced by alloying the interface. In doing so caution needs to be exercised on interface effects on electron transport too. Also reducing the interface separation distance contributes towards reduced thermal conductivity [24].

In case of phonon transport perpendicular to the interfaces increasing the *phonon reflectivity* also aids in decreasing the thermal conductivity. Phonon reflectivity can be engineered by varying the mismatch between the material properties (density, group velocity, and specific heat and phonon spectrum) of 2 conjoint materials in a layered structure [24]. Depending upon the increase or decrease in phonon reflectivity at a boundary, the boundary or interface scattering effects can be aiding or detrimental

to thermal conductivity [24].

The *localization* of long wavelength phonon can increase phonon confinement and thereby decrease thermal conductivity. Phonon confinement is aided by huge mismatch in the dispersion relation in a superlattice or hetero-structure. The use or aperiodic or composite superlattices with different periodicities does help achieve localization [24].

Defects and dislocations also provide alternate means to reduce thermal conductivities [24]. Hence the thermoelectric materials are heavily doped to reduce their thermal conductivities.

Owing to the large number of design parameters it is extremely difficult to experimentally test every possible material and geometry combination. Hence modeling and simulation plays a very significant role in designing and optimizing TE and thermal management solutions [26].

1.4 Modeling Techniques

In recent years, modeling of non-equilibrium heat transport is executed by two (2) main approaches: a) Molecular Dynamics (MD) simulations, and, b) Boltzmann Transport Equation (BTE) based methods. Both approaches are deemed valid as long as phonons are assumed to be particles i.e. quantum wave effects can be neglected [60].

Figure 1.9 provides a general guideline for the appropriate treatment of phonon transport in nanostructures based on the dominant phonon mean free path (MFP) and wavelength at room temperature. Modeling of phonon transport using the Boltzmann

particle transport equations (BTE) is adopted only when the scattering rates of electrons or phonons vary significantly within a distance comparable to their respective mean free paths [75].

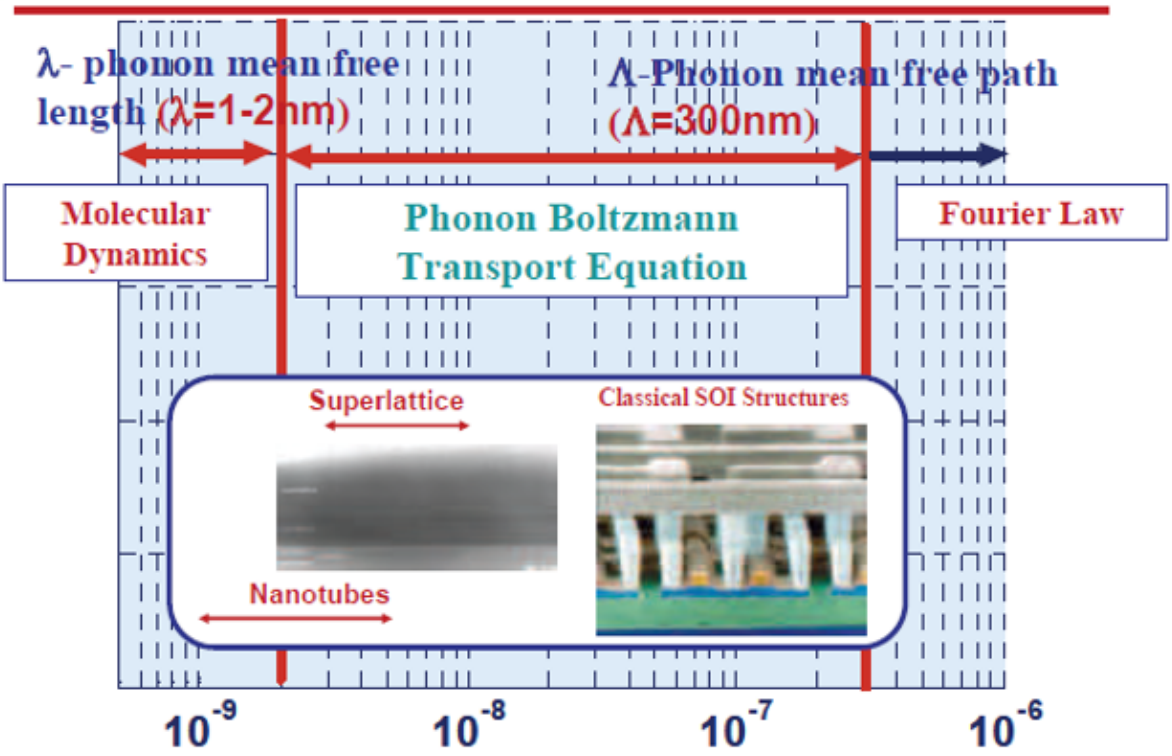

Figure 1.9 outlines the regime map for modeling phonon transport based on the characteristic length and phonon mean free path [75].

1.4.1 Molecular Dynamics

Molecular Dynamics (MD) involves the integration of the Newton's equations of motion in time for a large collection of particles that interact with one another. The force interactions in a MD approach calls for a good interatomic potential. The MD approach needs a good interatomic potential describing the underlying force interactions. The accuracy and consistency of the scheme depends upon the accuracy of the interaction

potential [60]. The critical issues with MD simulations are the information on individual phonon braches that cannot be extracted from these simulations. Also the force calculations in case of many body potentials is computationally very expensive [60].

1.4.2 BTE based Methods

Boltzmann Transport Equation (BTE) provides an alternative method to model non-equilibrium heat conduction. One of the preliminary BTE based analytical models for thermal conductivity at low temperatures was proposed by Callaway [32]. Major limiting assumptions of the Callaway model were elastic isotropy, the absence of dispersion and the inability to make any distinction between the relaxation times of longitudinal or transverse phonons. Holland [33] [34] improved upon the Callaway model by including phonon dispersion. Holland also adopted frequency and temperature dependent lifetimes for transverse and longitudinal phonons. The limitation from Holland's model is his assumption of linear dispersion relation which dictated a constant group velocity.

Later with advancement in the computing speed numerical techniques such as *(a) deterministic methods*; and *(b) stochastic or Monte Carlo based methods* were adopted. Deterministic methods solved BTE as a partial differential equation led to the development of Equation of Phonon Radiative Transport (EPRT), by Majumdar et al. [35]. Due to the ability of Monte Carlo (MC) based methods to emulate the phonon behavior and introduce more randomness as close to reality has nailed the success of MC based simulation methods. Monte Carlo simulations are explained in detail in Chapter 3 of this work.

1.5 Scope of this Work

This work primarily involves proposing a better model to predict the thermal conductivity and study its effects in both thermal management and thermoelectric regimes. The primary objectives of this work are four fold:

- To atomistically compute phonon dispersion relation using KVFF approach that accounts for crystal atomicity, anharmonic crystal interactions, geometric confinement and stress induced by hetero-structures.
- Statistical modeling of non-equilibrium heat transport based on Monte Carlo technique to solve the BTE. The proposed solver has the potential to predict thermal conductivities from bulk to nanostructures for 3 dimensional device geometries. The solver also accounts for frequency dependent mean free paths.
- Integrate the atomistically computed phonon dispersion with the Monte Carlo Phonon Transport (MCPT) kernel to better predict thermal conductivities.
- Validate the proposed solver at both ballistic and diffusive regimes
- Compute the thermal conductivities for III-V nanostructures
- To use the atomistically determined thermal conductivity in a thermal management application (LED) and a thermoelectric application (Thermoelectric Cooler).

CHAPTER 2

MULTI-SCALE MODELING TO ADDRESS NONLINEARITY IN HEAT TRANSPORT

The first and foremost step in modeling heat transport is to describe the vibration of atoms in the material lattice. These atomic vibrations contribute to the *free energy* of the system, which in turn affects the equilibrium and non-equilibrium thermodynamic properties, whereas the frequency of the vibrations determines the transport properties [36]. These atomic vibrations are superposition of vibrations of individual atoms around their equilibrium sites due to the interaction with their neighboring atoms. Hence these cumulative vibrations of atoms in the crystal form a wave of allowed wavelength and amplitude describing the dynamics of the lattice. The nature of the described wave depends on the vibrational modes of the atoms which are often referred to as polarization modes.

2.1 Lattice Dynamics

Lattice dynamics seeks to determine the modes of vibration of the crystal lattice, where the particle representation of the modes of vibration are referred to as quantum of vibrations or *phonons*. There exists 2 modes of polarization namely (1) Longitudinal, where the displacement of atoms from their equilibrium position is in the direction of propagation of the wave, and (2) Transverse, where the displacement of atoms from their equilibrium position is perpendicular to the direction of propagation of the wave. Hence for a lattice described by Cartesian coordinates there exists 1 longitudinal mode (along *x* axis) and 2 transverse modes (along *y* and *z* axes), considering the wave is propagating along the *x* axis. Since the energy transport in solids depends on the

frequency of these vibrations, it is imperative to compute the frequencies of phonons as a function of vector in the direction of propagating wave (wave vector, *K*), which is often referred to as dispersion relation. The wave vector defines the vector in reciprocal space.

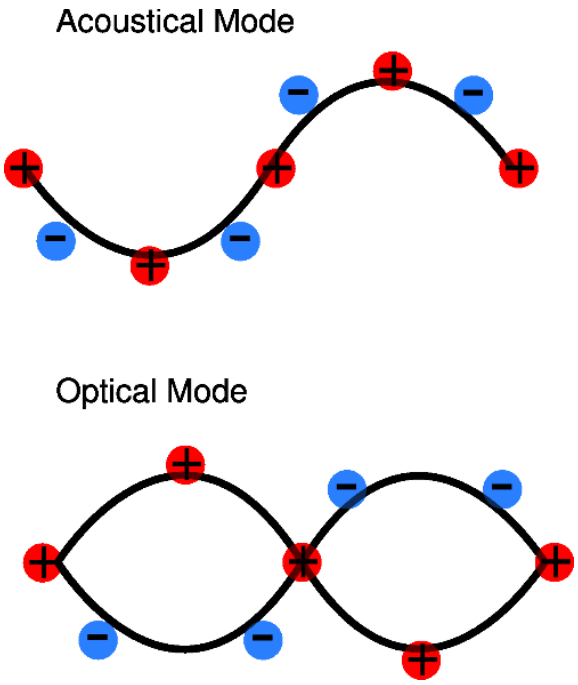

Figure 2.1 illustrates acoustic and optimal modes of vibration using a 1-D diatomic chain of atoms [37]

Also depending upon the number of atoms in the unit cell the dispersion curves are represented as acoustical or optical branches. The prime difference between acoustical and optical branches are primarily due to extended options of vibrations for atoms in the unit cell. In case of a diatomic unit cell, the 2 atoms with different masses can move *in phase* giving rise to acoustical branch or *out of phase* giving rise to optical branch as illustrated in Figure 2.1. In general, for a unit cell with *N* atoms there exist 3 acoustical branches (1 longitudinal and 2 transverse) and 3N-3 optical branches (N-1

longitudinal and 2N-2 transverse) [38].

2.2 Modeling Lattice Dynamics

A crystal structure can be modeled as spring-mass network in which masses represent the atoms and springs represent the chemical bonds connecting the atoms in the crystal lattice as illustrated in Figure 2.2 [60]. Since the atoms are connected to one another, the displacement of one or more atoms from their equilibrium positions give rise to a set of vibration waves propagating through the lattice [39]. Energy transport is primarily facilitated by these propagating lattice waves.

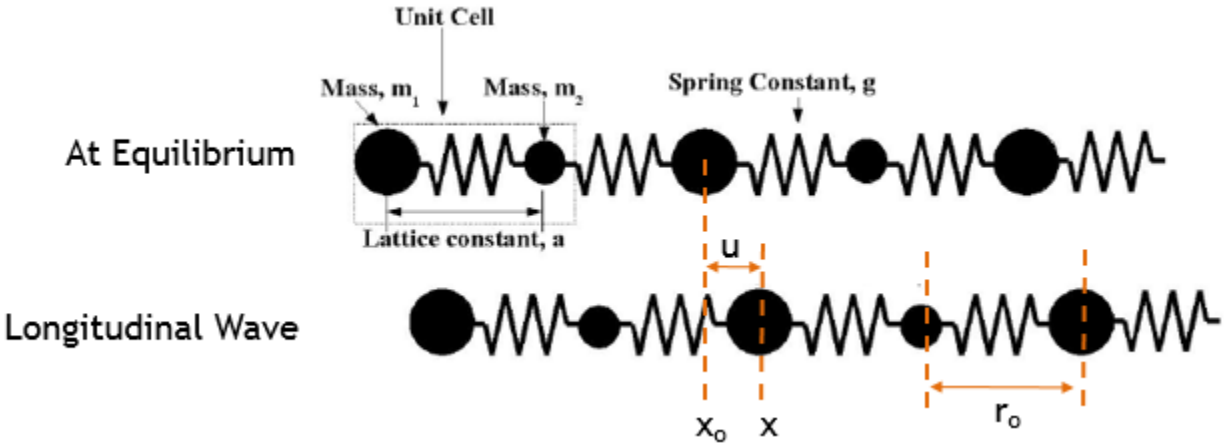

Figure 2.2 illustrates the 1-D diatomic chain of atoms as spring and mass network at equilibrium and longitudinal displacement [60].

In a rigid lattice the atoms exert forces on one another, so as to retain its equilibrium position (x_o). The exerted forces may correspond to either Van der Waals forces, covalent bonds, or electrostatic attractions. A potential energy function, U characterizes the forces between each pair of atoms, based on the distance of separation of the atoms. The net potential energy of the entire atomic lattice is the sum of all pairwise potential energies [39].

Solving a many-body problem to its completeness using either classical or quantum mechanics is a computationally breathtaking task. Hence 2 prime approximations are enforced to make it computationally viable. First approximation is that, the characterized potential energy function U considers the sum of the pairwise potential energies of the neighboring atoms only. Although the inter-atomic forces in real solids influence all the atoms in the solids, this approximation is nevertheless valid owing to the screening effect caused by the fields of distant atoms. Second approximation is that the potentials, U are assumed to be harmonic in nature which is valid as long as the atoms remain close to their respective equilibrium positions [39]. Mathematically, the Taylor expansion of U about its equilibrium value results in determining the elastic force proportional to the 1^{st} order term x, and displacement represented by a quadratic term x^2. The higher order terms are neglected on the basis that the resultant error is small as long as x remains closer to its equilibrium position x_o. The potential energy due to displacement of an atom from its equilibrium position x_o to x due to longitudinal lattice wave is illustrated in Figure 2.2 [60] [39].

2.2.1 Atomic Bonding

The first step to model the lattice vibration is to understand the atomic bonding. The atoms in the lattice are separated by equilibrium separation distance r_o, as illustrated in Figure 2.2. Since the lattice vibrations result in altering the inter-atomic separation distance r, it is imperative to understand the nature of the atomic bonding. Since the bond is not rigid and exhibits a spring like behavior it allows the separation distance r_o to vary due to lattice vibrations. The potential energy, U, of the atomic bond

is proportional to the distance of separation between 2 atoms which can be plotted as shown in Figure 2.3.

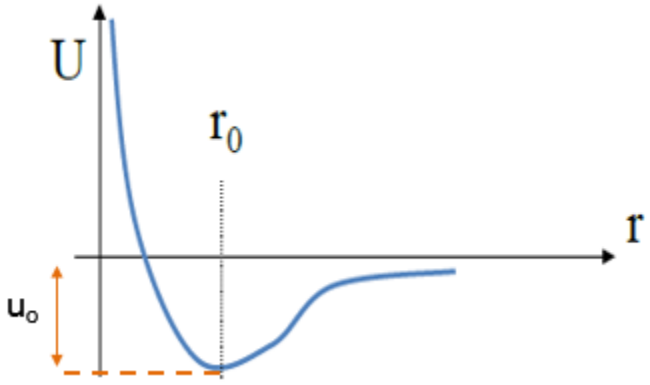

Figure 2.3 plots the potential energy as a function of inter-atomic separation distance [5] [41].

From Figure 2.3, it can be seen that the energy is minimum at the equilibrium separation distance r_o and u_o is the minimum energy required to make the potential energy zero or break the bond. Also observable from the figure is that as the inter-atomic separation distance increases the bond is broken (i.e. As $r \rightarrow \infty$ the potential energy $U \rightarrow 0$).

2.2.2 Harmonic Approximation

It can be perceived from Figure 2.3 that the represented potential energy for bonding between two atoms is not a simple function and hence to solve a many body equation with such a complex function is a mammoth task. In order to simplify the function to more idealized form, it is approximated that the atomic displacements due to lattice vibrations is very small and hence most of the displacements occur at the bottom of the potential energy well (circular shaded portion in Figure 2.4).

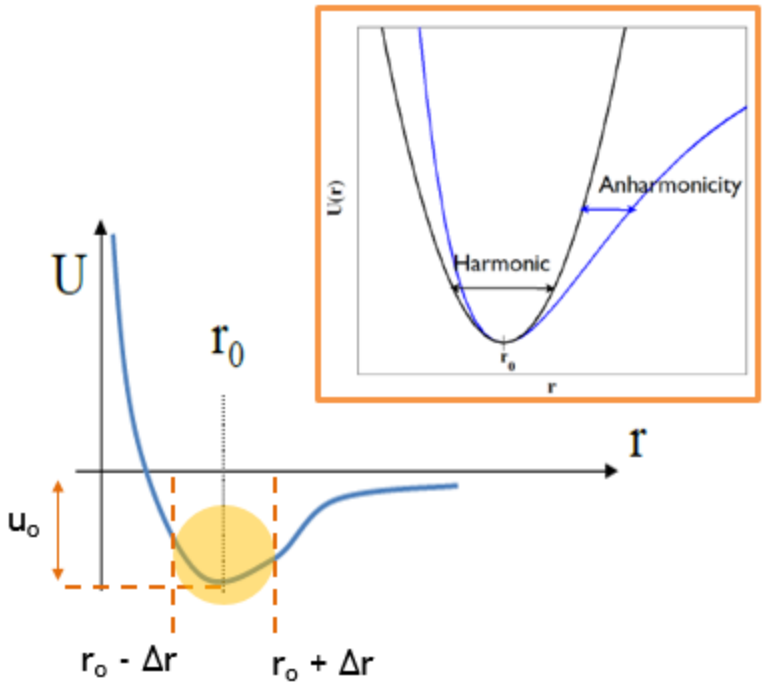

Figure 2.4 details the harmonic approximation (shaded region between $r_o - \Delta r$ & $r_o + \Delta r$) in the potential energy profile of lattice vibrations. The inset shows the parabolic consideration of harmonic assumption instead of the complex anharmonic curve.

It can be observed from Figure 2.4 that, such an approximation leads to a parabolic or spring like function which is harmonic in nature and hence often referred to as harmonic approximation. The validity of harmonic approximation is justified by that, if $r_o - \Delta r << r_o$, then the distance of separation between the atoms will be less thereby requiring a huge potential energy since the atoms will be repelled by their nucleus. On the other hand if $r_o - \Delta r >> r_o$, the atoms would move apart from each other and hence result in breaking of the bond. On these aforementioned grounds the harmonic approximation is still considered valid to model the thermal behavior of materials. Hence the potential energy for lattice vibrations which do not involve large displacements are idealized with a spring equation (Equation 2.1).

$$U = \frac{1}{2} gu^2 \tag{2.1}$$

Where, u represents the difference between actual separation r and the equilibrium separation r_o ($r - r_o$), and g represents the spring constant which describes the strength of the bond. In order to better explain the model a simple 1-D atomic chain as shown in Figure 2.2 is considered, where the atoms are represented by masses, m and separated by lattice constant, a. Hence the potential energy for a 1-D lattice is the sum of pairwise harmonic potential energy of atoms in the atomic chain containing n atoms, which is expressed as follows,

$$U^{harm} = \frac{1}{2} g \sum_n \{u[na] - u[(n+1)a]\}^2 \tag{2.2}$$

The summation in Equation 2.2 captures the relative displacement of each atom from its nearest neighbors for n atoms. The primary goal is not to determine their potential energy, but to develop an equation of motion for the atom located at $u(na)$ as shown in Equation 2.3.

$$\begin{aligned} F &= m\frac{d^2u(na)}{dt^2} = -\frac{\partial U^{harm}}{\partial u(na)} \\ &= -g\{2u_n - u_{n-1} - u_{n+1}\} \end{aligned} \tag{2.3}$$

From Equation 2.3, it can be observed that change in position of the atoms influences the potential energy. In order to solve the governing equation 2.3 a more generic plane wave solution as dictated by Equation 2.4 is considered.

$$u_n(t) \sim \exp\{i(Kna - \omega t)\} \tag{2.4}$$

Applying a plane wave solution (Equation 2.4) to governing equation (Equation

2.3) yields,

$$-m\omega^2\, e^{i(Kna-\omega t)} = -g\left[2 - e^{-iKa} - e^{iKa}\right] e^{i(Kna-\omega t)} \tag{2.5}$$

On solving Equation 2.5 for ω results in the dispersion relation (Equation 2.6). The dispersion relations (ω-K relation) consolidates the effect of dispersion due to a medium on the properties of a wave traveling within that medium. Also dispersion relation describes the rate at which the phonons of a particular frequency travel though the medium since $^{\partial\omega}/_{\partial K}$ gives the phonon group velocity, v_g).

$$\omega(K) = \sqrt{\frac{2g(1-cosKa)}{m}} = 2\sqrt{\frac{g}{m}}\left|\sin(\frac{1}{2}Ka)\right| \tag{2.6}$$

Paramount significance needs to be ascertained in order to determine the dispersion relation since it describes the fundamental properties of phonons such as frequency, polarization, group velocity and density of states. So any error in the prediction of dispersion relation shakes the very foundations of the phonons, which necessitates the use of an accurate dispersion relation by reducing the approximations to more realistic manifestations.

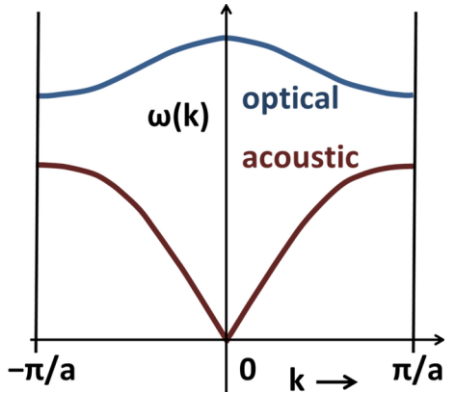

(a)

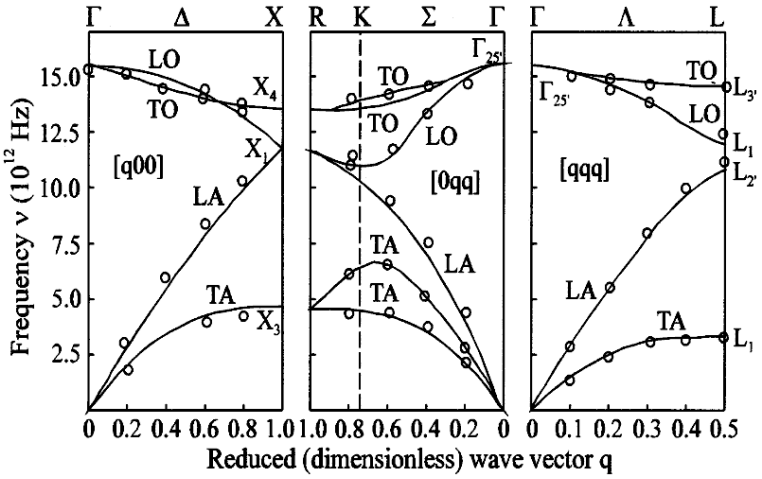

(b)

Figure 2.5 (a) shows the theoretical illustration of dispersion relation for optical and acoustic modes curtailed to 1 Brillouin zone; (b) shows the phonon dispersion for bulk silicon [42].

2.3 Need for Anharmonic Considerations

A real crystal allows expansion to a larger volume from its equilibrium than compression to a smaller volume more easily which is facilitated due to the shape of the interatomic potential curve. This statement deviates from Hooke's law since modeling lattice vibrations with harmonic approximation does not produce this property. These aforementioned effects are due to the anharmonicity that is manifested in higher order terms in potential which are ignored in harmonic approximation. Since the ionic potential is approximated with the truncation of Born-Oppenheimer (BO) energy surface at the quadratic term, the displacement of the atoms from their equilibrium positions is assumed to be small (as detailed in Figure 2.4) in comparison to the interatomic distance.

Some implications due to harmonic approximation are described as follows:

- *Infinite thermal conductivity* - harmonic approximation considers phonons as quasi-particles with an infinite lifetime and hence the crystal is assumed to vibrate forever. Hence the finite values of the thermal conductivity in solids are unaccounted for. In the harmonic approximation, the lattice waves are considered to be normal modes where the phonons do not change with time. Hence the phonons are prohibited from interacting with each other, in the absence of boundaries, lattice defects and impurities (which also scatter the phonons), resulting in improper treatment of phonon-phonon interactions.
- *Temperature independent heat capacity* - The heat capacity C_V becomes

constant at temperatures greater than Debye temperature (T > θ).

- *Absence of thermal expansion* – As per harmonic oscillations, the average position of the atom remains unchanged, irrespective of the increase in amplitude of oscillation which can be inferred from Figure 2.6 (a) and hence the harmonic theory fails to account for thermal expansion. Since the frequency of the phonons are independent of the amplitude of the oscillations, the pressure of a gas of harmonic phonons is temperature-independent. However, when the anharmonic terms are considered while modeling the potential energy of the atoms, the phonon gas acquires a finite temperature dependent pressure, resulting in thermal expansion of the crystal [43]. Taylor expansion of the potential energy of the atoms at a displacement x from the equilibrium position in the crystal lattice results in,

$$U(x) = cx^2 - gx^3 - fx^4 \ldots \quad (2.7)$$

Where, the 1st (quadratic) term represents harmonic approximation, the 2nd term represents the asymmetry in mutual repulsion of neighboring atoms, and the 3rd term represents the softening of vibrations at large amplitudes. The increase in the lattice constant in the crystal with increasing temperature is described by the thermal expansion coefficients g and f. These anharmonic terms are responsible for average displacement of atoms from its equilibrium positions as illustrated in Figure 2.6 (b).

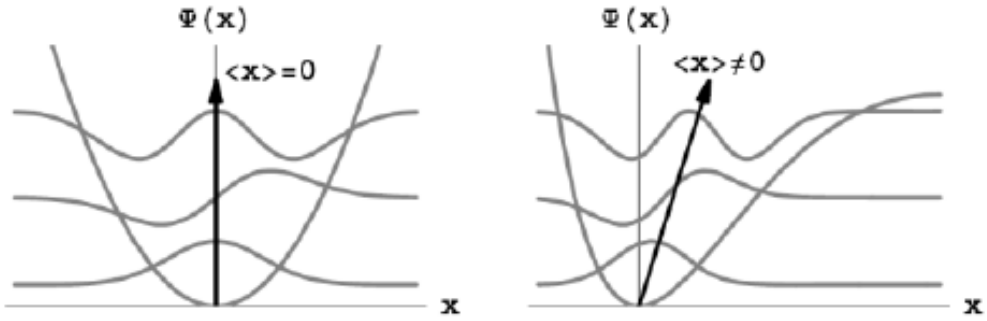

(a) (b)

Figure 2.6 (a) shows phonon wavefunctions for a harmonic potential well where the average displacement <x> is zero for all modes; (b) shows phonon wavefunctions for a anharmonic potential where the average displacement <x> increases with increase in phonon energy.

- *Adiabatic and the isothermal lattice constants are the same.*
- *The elastic constants are independent of pressure and temperature.*
- *Strain Effects* – Strain due to super-lattices or crystal defects can also cause displacement of the atoms from its equilibrium position which needs to be accounted for. Spring stiffness, g, changes with strain. The consideration of strain is of paramount importance owing to emerging advantages of engineering phonons to modify the thermal conductivities using hetero-structures [45].

Hence when the displacements of the atoms largely exceed the valid range for the harmonic potential, the harmonic approximation and any perturbative approach based on it breaks down [36]. This phenomenon is observed when the system experiences dynamical instability. Thereby describing the temperature dependence of the phonon spectra is significant and inclusion of anharmonic corrections to the free energy is mandatory to describe properly thermodynamic properties. For this

purpose this work incorporates a quasi-anharmonic Molecular Mechanics (MM) based model to compute the dispersion relation.

2.4 Multi-Scale Modeling

As the length scale approaches atomic level, the effects due to structural and surface relaxations, alloy disorder, lack of crystal symmetry, high ionicity, defects formation, amorphous interlayer, and atom clustering are all important [46]. The performance of devices at nanoscale involves characterization of multiple processes such as internal fields, electronic bandstructure effects, and dynamics of charge and phonon transport phenomena and, hence modeling of these devices pose a multi-physics problem. In order to address these needs, a multi-scale simulation approach, which essentially bridges the gap between contemporary continuum and highly accurate ab initio models and has the capability of handling realistically-sized devices containing more than 100 million atoms is required [47].

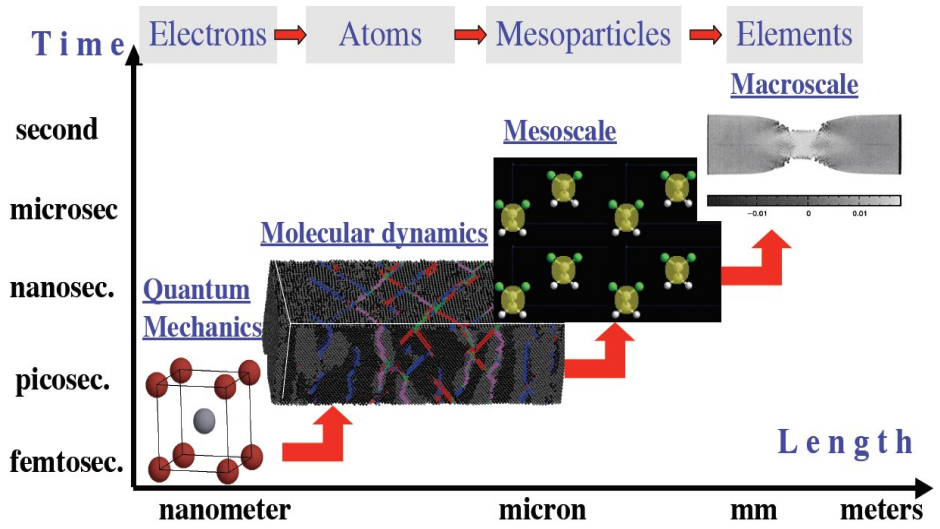

Figure 2.7 illustrates the length- and timescale for various computational methods.
Figure 1 illustrates the length and timescale for various computational methods

such as quantum mechanics–based methods, classical molecular dynamics methods, and numerical continuum mechanics methods. Quantum mechanics–based treatments are confined to very short time and length scales, on the order of a few nanometers and picoseconds owing to their computational complexity. Once empirical interactions are assumed in classical molecular dynamics schemes, the length and time scales achieved are dramatically increased, approaching micrometers and nanoseconds [46]. Finally Continuum mechanics–based simulation tools treat virtually any length scale with the only exception of lacking proper description at small scales. Novel nanoscale devices are unique examples of systems where different branches of physics (molecular dynamics, quantum electronic structure, charge and phonon transport, statistical physics and thermodynamics, classical electrostatics, and optics) meet together spanning across different spatial and time scales. Therefore, device modeling at nano scales is a multi-scale and multi-physics problem. Hence in order to model a multi-dimensional multi-physics problem, it necessitates the need to employ a multi-scale modeling approach [46].

2.5 QuADS-3D [Ref: 11]

QuADS bridges the gap (and crosses the intellectual boundary) between continuum and ab initio modeling paradigms and enable the quantum-corrected atomistic numerical modeling of non-equilibrium charge and phonon transport phenomena in realistically-sized systems containing more than 100 million atoms! QuADS is primarily being built upon extended versions of three modules: (a) Open source LAMMPS molecular dynamics code for geometry construction and modeling

structural relaxations. To enhance accuracy, ab initio ABINIT tool is used for parameterization of force and polarization coefficients and model bandstructure calculations; (b) Open source NEMO 3-D tool, which employs a variety of tight-binding models (s, sp^3s^*,$sp^3d^5s^*$), for the calculation of excitonic and phonon spectra and optical transition rates; and (c) A quantum-corrected (benchmarked against the non-equilibrium Green function formalism) 3-Monte Carlo electron–phonon transport kernel.

The simulation strategy involved is divided into different computational phases, spanning from the molecular structure of the constituting elements, to the electron and phonon band structure, transport and optical coupling, is depicted in Figure 2.8.

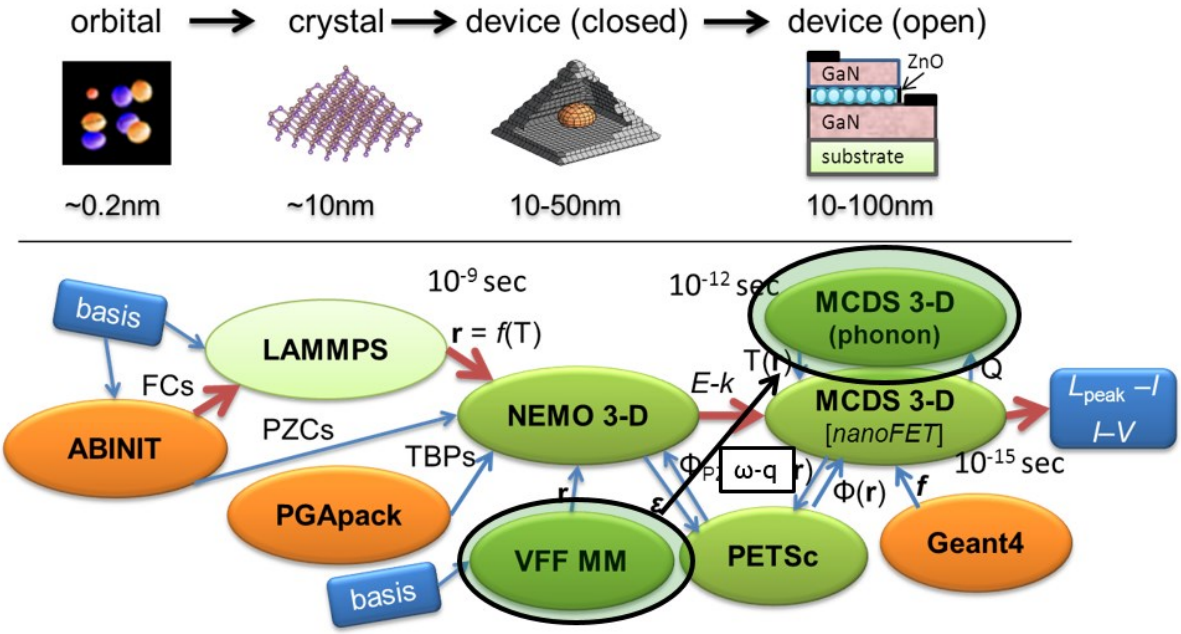

Figure 2.8 QuADS simulation platform. The circles and arrows in black points to my contribution to QuADS

The figure also shows the domains with length scales, program flow (major up-stream flow in bold arrow), the data interfaces, codes used, the associated observables, how one passes between phases, and their interdependencies, and relevant time

scales. basis: atomic basis to define a crystal, ABINIT: abinitio module, FCs: force constants, PZCs: polarization coefficients, TBPs: tight-binding parameters, LAMMPS: massively parallel molecular dynamics code, *r*: atom positions, *f(T)*: as a function of temperature, VFF MM: valence force-field molecular mechanics, NEMO 3-D: nanoelectronics modeling tool for bandstructure calculations, *E*-*k*: energy bandstructures (effective masses, bandgaps, density-of-states), PETSc: parallel linear algebra solver, *T(r)*: temperature distribution, *Q*: heat, *Φ(r)*: potential distribution, *n(r)*: charge density distribution, *L*peak −*I*: peak intensity vs. current characteristic.

This work primarily focusses on developing a 3D Monte Carlo kernel to emulate phonon transport and couple it with Molecular Mechanics based VFF tool to describe the properties of phonons accurately.

2.6 Molecular Mechanics

Molecular mechanics employs the use of classical mechanics to model molecular structures and its properties [49]. Molecular mechanics is commonly used in modeling small molecules as well as large biological/non-biological systems or material assemblies with many thousands to millions of atoms. Molecular mechanics methods are based on the following principles [49] [50],

- Each atom is simulated as a single particle, where nuclei and electrons are lumped into atom-like particles.
- The particles are described by fundamental properties such as radius (typically the van der Waals radius), polarizability, and a constant net charge (generally derived from quantum calculations and/or experiment)

- Atomic bonds are considered as spring with an equilibrium distance equal to the experimental or calculated bond length described using classical mechanics.
- Interactions are based on classical potentials.
- Interactions are pre-assigned to specific sets of atoms.
- Interactions determine the spatial distribution of the modeled particles and their energies.

Molecular Mechanics or force-field methods use classical mechanics analogous to spring mass network to predict the energy of a molecule as a function of its conformation. The potential energy of all systems in molecular mechanics is calculated using force fields [49]. Molecular Mechanics predicts the equilibrium geometries, its transition states; and relative energies between conformers or between different molecules [50].

In Molecular mechanics the total energy is expressed as sum of Taylor series expansions for energy due to bond stretching between pair of bonded atoms, and the associated additional potential energy terms resulting from bending, torsional energy, van der Waals energy, electrostatics, and cross terms as illustrated in Equation 2.8.

$$E_{Tot} = E_{stretch} + E_{bend} + E_{tor} + E_{vdw} + E_{el} + E_{cross} \quad (2.8)$$

The decomposition of the total energy term can be grouped into bonded and nonbonded terms, where bonded terms relate to atoms that are linked by covalent bonds, and nonbonded (also called "noncovalent") terms represent the long-range electrostatic and van der Waals forces. The specific decomposition of the terms depends on the force field, but a general form for the total energy in an additive force field is laid out in Equation 2.8.

2.6.1 Force Fields

The potential energy for a system of particles (typically molecules and atoms) is described by mathematical functions, whose form and parameters are referred to as Force Fields [53]. The force field describes the energy of a molecule primarily based on its atomic positions [52]. The most significant property of the force field is that, the force field form and parameters for a particular atom or group of atoms should be the same for different molecules, i.e. they should be *transferable*. But for this property, distinct force fields needs to be constructed for each different molecule, thereby making it computationally a complex task when modeling alloyed materials. For example, in case of carbon-hydrogen bonds the stretching frequencies and C-H bond lengths remain constant irrespective of the molecular environment [52].

There exists many variants of force fields based on various forms of force field employed to capture discrete interactions within and between molecules [52]. Force fields also include additional energy terms that capture various other deformations. So as to improve the accuracy of the model, some force-fields account for coupling between bending and stretching in adjacent bonds.

The mathematical form of the energy terms varies between various force-fields, of which more common forms are bond stretching, bond bending, torsional and inversion energies as illustrated in Figure 2.9.

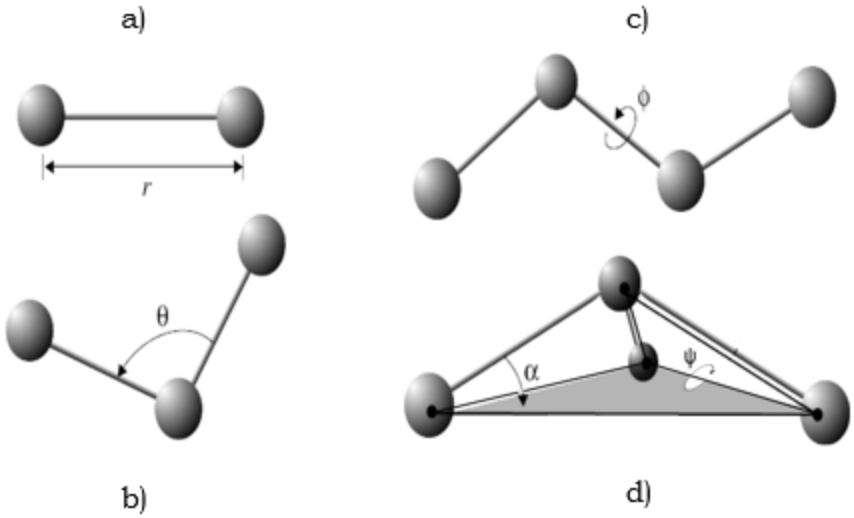

Figure 2.9 illustrates the internal coordinates for commonly described bond interactions: r governs bond stretching; θ represents the bond angle term; φ represents the torsional angle; and the out of plane represents the inversion angle

2.6.2 Valance Force Field (VFF)

In valence force field the energy of the molecule is described by accounting for internal co-ordinates, bond lengths, bond angles, torsional angles, and Cartesian co-ordinates of the atoms. Due to the simplicity and universality of the valence force field, the term force field is usually referred to a valence force field [52]. The choice of the force field employed is mostly determined by the physical nature of the problem that needs to be addressed. For example, an empirical force field is used to extrapolate the phonon dispersion over the Brillouin zone, leading to excellent description of thermodynamic quantities in case of a perfect crystal, whereas the same description deems to be invalid under defect geometries (due to built-in strain in hetero structures). Hence in order to describe a force field that is transferable in case of a deformed crystal (aperiodic), where the force field used is well beyond the valid region of harmonic approximation [55]. Thus the described field must be capable of reproducing the phonon

dispersion curves well beyond the region of validity of the usual harmonic approximation [55].

Covalent materials are attractive to use valence force fields, since the lattice potential energy is expressed in terms of the so-called valence coordinates such as, bond lengths and bond angles. The proper description of interatomic interactions in terms of valence coordinates is facilitated by the existence of highly localized bonds. Owing to the simple and graphical chemical description of valence force fields the parameterization is made easy, which adds to the advantage of using valence force fields. On applying to crystals of the diamond structure, the valence force field in its simplest form accounts for contributions arising only from independent bond stretching and independent angle changes between adjacent bonds. Under these assumptions, the valance force fields (VFF) are classified both in the harmonic (Keating 1966a) and anharmonic regimes (Keating 1966b, Vukcevich 1970, Koizumi and Ninomiya 1978) [55].

2.6.3 KVFF Approach

From above discussions it can be inferred that there exists a clear trade-off between the spectrum and complexity of these force fields and their transferability. Under elastic limit (no plastic relaxation), Keating's Valance Force Field model (KVFF) based on first nearest neighbor force field proves to strike a good balance between accuracy and efficiency for diamond and zinc-blende materials, thereby providing very good description of the elastic properties of silicon and germanium, and a reasonable description of those of III–V materials [56]. The accuracy of description of III–V materials

can be further improved by considering long-range interactions. Based on the work of *Niquet et al* [56], KVFF model can be used to model materials with wurtzite crystal structure as well.

The valence force field model of Keating involves the use of two important forms of force field namely, bond Stretching and bond bending. In order to arrive at the functional form for bond stretching interactions, the changes in energy are associated with changes in bond length between 2 atoms. The energy of a bond is considered to be the least at a reference length, hence the compression of the bonds result in overlapping of the electron clouds resulting in a rapid increase of energy, or stretching the bonds beyond equilibrium results in increase in energy until the bond disassociates. In such cases the energy due to small deviations from the equilibrium bond length can be expressed as Taylor expansion in $r\text{-}r_0$, with r_0 representing the equilibrium bond length as shown in Equation 2.9 [52].

$$E(r) = E(r_0) + \left.\frac{dE}{dr}\right|_{r=r_0} (r - r_0) + \frac{1}{2}\left.\frac{d^2E}{dr^2}\right|_{r=r_0} (r - r_0)^2 + \frac{1}{6}\left.\frac{d^3E}{dr^3}\right|_{r=r_0} (r - r_0)^3 + \cdots \tag{2.9}$$

Where r_0 represents the equilibrium bond length and r represents the actual bond length. In order to simplify the description of Equation 2.9 and restrict it to harmonic approximation Equation 2.9 is terminated at the quadratic term. Harmonic approximation is generally justified by the consideration that the forces between bonded atoms are very high in comparison to other forces, which breaks down in the case of larger deviations from r_0. A plot of this is shown in Figure 2.10 [57].

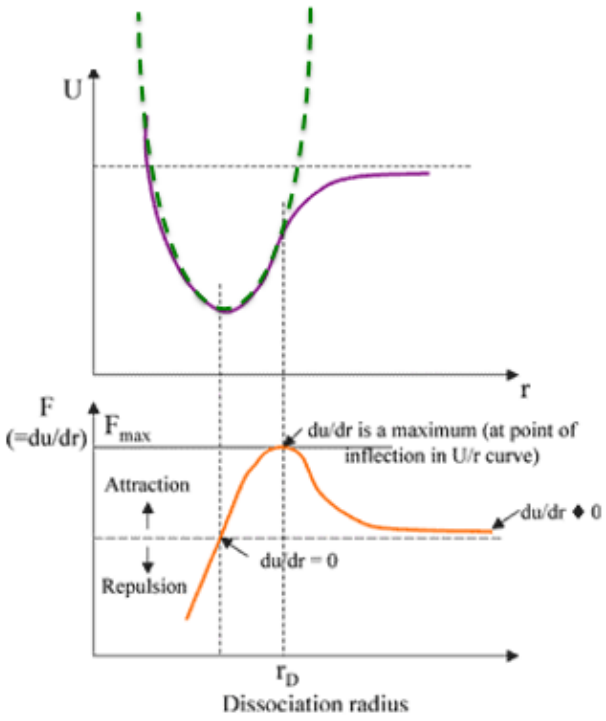

Figure 2.10 illustrates the potential energy & force profile of bond stretch interctions. The he dotted line shows the harmonic approximation to the bond stretching potential

In order to accurately account for the molecular structures and vibrational frequencies, where the deviation from r_0 is large, it is necessary to go beyond the harmonic approximation and include higher order terms usually up to the fourth order [52]. Hence to account for better accuracy, Keating VFF describes the bond stretching energy as per Equation 2.10.

$$U_{bs}^{ij} = \frac{3}{16}\,\alpha_{ij}\,\frac{(r_{ij}^2 - r_{0_{ij}}^2)^2}{\left\| r_{0_{ij}}^2 \right\|} \tag{2.10}$$

Where, α_{ij} represents bond stretching force constant. Similar to the bond stretching interactions, the bond bending interactions can also adhere to harmonic approximation, if considered till quadratic term in Equation 2.11.

$$E_{bend}(\theta) = \frac{1}{2}\, k_\theta(\theta - \theta_0)^2 + \cdots \tag{2.11}$$

Where, k_θ is the angle bending force constant, θ is the actual bond angle and θ_0 is the equilibrium bond angle. Similar to bond stretch interactions the accuracy of the energy function can be improved with inclusion of higher order terms. Hence KVFF bond bending energy turns out to be,

$$U_{bb}^{jik} = \frac{3}{8}\, \beta_{jik}\, \frac{(r_{ij}.r_{jk} - r_{0_{ij}}.r_{0_{ik}}.\cos(\Delta\theta_{jik}))^2}{\left\|r_{0_{ij}}\right\| \left\|r_{0_{ik}}\right\|} \tag{2.12}$$

Where, β_{jik} represents the bond bending force constant and $\Delta\theta_{jik}$ represents the common angle between the three atoms at their equilibrium position. Hence the total potential energy described by KVFF model is the sum of energies due to bond stretching and bond bending interactions as per Equation 2.13.

$$U = U_{bs}^{ij} + U_{bb}^{jik} \tag{2.13}$$

2.7 KVFF – MM Model: NEMO 3D

NEMO 3-D currently employs the atomistic valence-force field (VFF) with strain-dependent Keating potentials. The flow schema of NEMO-3D's dispersion relation computation based on KVFF model is laid out in Figure 2.11.

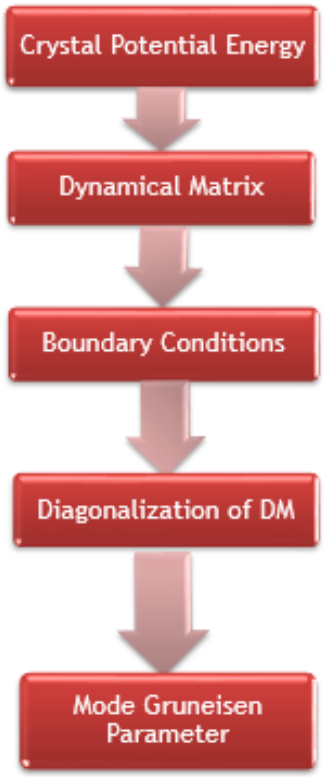

Figure 2.11 illustrates the computational flow structure of KVFF model employed in NEMO-3D

This approach computes the total elastic energy of the sample as a sum of bond-stretching and bond-bending contributions from each atom as described in equation 2.13 [46]. The equilibrium atomic positions are found by minimizing the total elastic energy of the system. The total elastic energy in the VFF approach has only one global minimum, and its functional form in atomic coordinates is quartic [46]. The conjugate gradient minimization algorithm in this case is well-behaved and stable. The flow schema of NEMO-3D's dispersion relation computation based on KVFF model is laid out in Figure 2.11.

The KVFF model approximates the crystal potential energy U, based on short range atomic interactions as stated in Equations 2.13, 2.12 and 2.10. A crystal at

equilibrium does not have any force acting on it, whereas in reality the crystal undergoes perturbations like lattice vibrations which induces a restoring force. In order to compute the restoring force Newton's classical force equation is set into motion as described in Equation 2.14.

$$F_i = mi\frac{d^2(\Delta R_i)}{dt^2} = -\frac{\partial U}{\partial(\Delta R_i)} = -\frac{1}{2}\frac{\partial}{\partial(\Delta R_i)}\sum_{i\in NA}\left[\sum_{j\in nn(i)} U_{bs}^{ij} + \sum_{j,k\in nn(i)}^{j\neq k} U_{bb}^{jik}\right] \tag{2.14}$$

In case of a zincblende crystal structure KVFF model accounts for 8 bond stretching and 12 bond bending interactions. Since solving a linear equations as matrices are computationally less expensive, the force equation is formulated with Dynamical Matrix (DM) as stated in Equation 2.15 [74].

$$F_i = D_{mn}^{ij}.R \tag{2.15}$$

Where, $i, j \in N_A$ and $m, n \in [x, y, z]$

Where, R is a column vector of displacement for each atom. The motion of the atoms with respect to a small restoring force in a given system is captured by dynamical matrix captures. The DM for an atom "i", describing its interaction with atom "j", given by Equation 2.16.

$$D(ij) = \begin{bmatrix} D_{xx}^{ij} & D_{xy}^{ij} & D_{xz}^{ij} \\ D_{yx}^{ij} & D_{yy}^{ij} & D_{yz}^{ij} \\ D_{zx}^{ij} & D_{zy}^{ij} & D_{zz}^{ij} \end{bmatrix} \tag{2.16}$$

Where the 9 components of D(ij), is given by,

$$D_{mn}^{ij} = \frac{\partial^2 U_{elastic}}{\partial r_m^i \, \partial r_n^j} \tag{2.17}$$

In case of each atom the size of D(ij) is fixed to 3 × 3 and hence for a unit cell containing NA atoms the size of the dynamical matrix is 3NA×3NA, which proves to be humungous when constructing a system containing > million atoms. Despite the greater size of the matrix it is computationally viable since it's mostly sparse. With harmonic approximation the dynamical matrix exhibits symmetry properties that can be readily utilized to reduce its assembly time by reducing the total number of calculations required to construct the dynamical matrix. When the matrix is stored for repetitive use, then only one of the symmetry blocks needs to be stored thereby reducing the overall memory requirement [74].

Thirdly the boundary conditions needs to be applied in order to calculate the eigenmodes of the lattice vibrations. Boundary conditions are classified into 2 types based on the finite or infinite nature of the system under study, such as; (i) Periodic Boundary Condition (PBC) or Born-Von Karman boundary condition which assumes infinite material extent in a particular direction and hence applied in case of bulk materials; and (ii) Finite Edge Boundary Conditions (FEBC) such as open or clamped, which assumes finite material extent in a particular direction and hence applied in case of nanostructures. Table 2.1 details the boundary condition employed based on the dimensionality of the structure used for calculation of phonon dispersion.

In case of nanostructures, the surface atoms are truncated and hence these atoms have different number of neighbors. Therefore in nanostructures the surface atoms vibrate differently when compared to the atoms inside the structure.

Dimensionality	Periodic BC	Finite Edge BC
Bulk (3D)	3	0
Thin Film (2D)	2	1
Nano Wire (1D)	1	2
Quantum Dot (0D)	0	3

Table 2.1 details the boundary condition employed in the DM based on the dimensionality of the structure. Table obtained from the work by *Klimeck et al* [74].

This effect is incorporated in DM by including a direction dependent *damping matrix* Ξ as per Equation 2.18.

$$\widetilde{D}(ij) = \Xi^{i}\ D(ij)\ \Xi^{j} \tag{2.17}$$

Finally the DM with appropriate BCs poses an eigenvalue problem that can be solved.

Finally, it is assumed that the time dependent vibration of each atom (ΔR(t)) are represented as the linear combination of phonon eigen modes of vibration u(λ,q), as per Equation 2.18.

$$\Delta R_i(t) = \sum_{q,P} u\ p\ (\lambda, q)\ e^{i(q.R_i - \omega t)} \tag{2.18}$$

On solving Equation 2.14 with Equation 2.18, the phonon dispersion relation (Figure 4.1) is obtained (Equation 2.19).

$$m_i \frac{\partial^2}{\partial t^2} \Delta R_i(t) = -\omega^2 \sum_{q,P} u\ p\ (\lambda, q)\ e^{i(q.R_i - \omega t)} \tag{2.19}$$

The modeling of Monte Carlo Phonon transport (MCPT) kernel is detailed in Chapter 3.

CHAPTER 3

MONTE CARLO PHONON TRANSPORT

The thermal behavior of a crystal can be estimated from the characteristics of phonons such as their location, velocity and polarization in the specified medium. The aforementioned phonon properties are obtained from the solution of BTE. In order to solve differential equations which involve a large number of independent variables like in the BTE, Statistical methods such as Monte-Carlo are employed as demonstrated in the fields of electron transport, structural mechanics, reliability theory, IC design and stock market forecasting. Contrary to the deterministic methods which are limited to simplified geometries, Monte-Carlo based methods are ideal for use in problems which involve complex physical geometries. Since this work involves formulating a numerical solution for BTE to predict the thermal conductivity of realistically sized structures spanning from nano to micro scale regime, it is imperative that a computationally cost effective solution is accomplished.

The distribution function *f*(r,K,t) in the BTE (3.1) is, in general, a function of seven independent variables, namely time (t), three space variables (r) and three wave vector (K) components, hence it calls for a non-deterministic approach such as MC technique to treat realistically sized structures so as to cater to low computational cost. Also, the ability of the Monte-Carlo (MC) technique to treat the individual phonon scattering events in isolation from each other, rather than using a single relaxation time for all scattering processes, makes it extremely attractive for use in solving the BTE for phonons. Mazumder and Majumdar [63] presented the first comprehensive algorithm to solve the BTE for phonons by the MC method with the inclusion of phonon dispersion

and polarization [60]. In their approach, statistical samples (phonons) are drawn from six individual stochastic spaces: three wave vector and three position vector components [63]. Lacroix *el al*, improved upon Mazumdar's work by decoupling N and U scattering processes and imposing frequency dependency on the velocity and scattering rate of governing phonons. In the latter approach sampled phonons first undergo drift (ballistic motion) and then undergo scattering events [60].

$$\frac{\partial f}{\partial t} + \nabla_{K,\omega_p} . \nabla_{\vec{r}} f = \left[\frac{\partial f}{\partial t}\right]_{scatter}$$
$$\frac{\partial f}{\partial t} + v_g \vec{K} . \nabla_{\vec{r}} f = \frac{-f - \langle n \rangle}{\tau} \quad (3.1)$$

3.1 Ensemble Monte Carlo (EMC) Schema

The Ensemble Monte Carlo (EMC) scheme adopted in this chapter is similar to the one described by [1,2,3,6], yet the current work stands out owing to its atomistically coupled dispersion relations which serves as a foundation for the aforementioned MC simulation. Some other prime advantages of this technique are [58]:

- The simple treatment of transient problems,
- The ability to consider complex geometries,
- The possibility to follow independently each scattering processes (e.g.; phonon-phonon, phonon-impurity and phonon-boundary processes).
- Efficient modeling of boundaries to account for thermal rectification.
- Study the effect of individual modes of phonon that account for thermal conductivity of a material.

- Accounts for classical size effects.

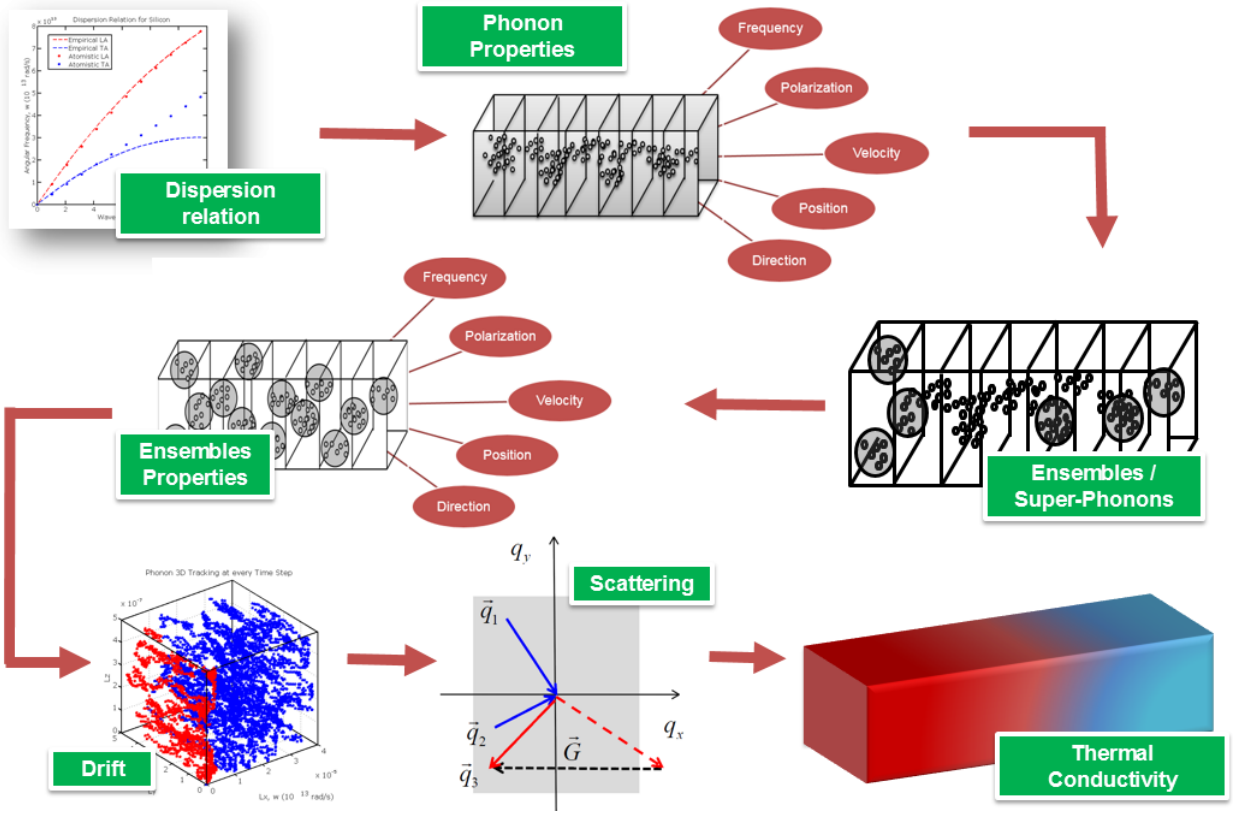

Figure 3.1 depicts a high level flow chart of various process steps involved in the current MC scheme

Figure 3.1 shows a high level overview of various process steps involved in EMC schema employed in this work. It can be inferred from the figure that the material dispersion relation serves as input to the Monte Carlo Engine. Since this work uses the dispersion relation generated by NEMO-3D, the predicted thermal conductivity accounts for changes at the atomistic scale too. From the input dispersion relation, the number of phonons and their properties such as group velocity, frequency, polarization, position and direction are determined. Since the number of phonons is of the order of ~10^9, the phonons are averaged by a weighting factor to form phonon ensembles or super-

phonons for which the new ensemble properties needs to be determined. After obtaining the number of ensembles and their properties, the ensembles are allowed to drift and scatter for a finite amount of time. During the drift phase the ensemble properties are tracked and appropriate changes are made as and when the phonon undergoes a scattering event. Finally the number of phonon ensembles in each cell is correlated to the local cell energy and thereby aids in determining the cell temperature, heat flux and thermal conductivity.

3.2 Simulation Domain and Boundary Conditions

In this work, the control volume assumes the shape of a simple rectangular parallelepiped structure (Figure 2.2) since it is analogous to the plane wall geometry commonly used in thermal problems [58]. The defined geometric volume is then divided into multiple spatial bins such that it can be interpreted as stack of cubic cells. These multidimensional stacks also provide the flexibility to model nanowires since it just involves the modification of size ratio. For MC simulations intended to predict thermal conductivity for geometric structures ranging from thin films to nanowires there exists 2 types of boundaries, they are 1) Isothermal and 2) Adiabatic.

Isothermal boundaries are preserved at constant temperature, thereby enabling them to act as a source or sink for the phonons. Any phonon that bumps into isothermal boundary during the phonon drift is thermalized or absorbed, such that it emulates the characteristic traits of a blackbody in radiation. Despite absorbing the phonons striking on their surface, the Isothermal boundaries also emit phonons into the structural volume depending on the cell temperature so as to establish thermal equilibrium. As far as this

work is concerned, having x axis as the direction of drift, the 1st and last cell stacks along the x axis act as isothermal boundaries. Also the states of phonons emitted into the computational domain are independent of state of phonons that are incident/absorbed at the boundary. As per the algorithm, any phonon that strikes the isothermal wall is stalked and deleted.

An *adiabatic* boundary is one in which the phonons are neither absorbed nor emitted, but only can be reflected. This work assumes that the lateral walls of the cells (in y and z directions) are adiabatic in nature. Despite the reflecting nature of lateral boundaries the algorithm needs to make sure that the momentum is preserved in x direction, so as to affirm that the heat flux is not perturbed in x direction [59] [60]. Figure 3.2 illustrates the geometric structure of the simulated system with spatial discretization and direction of heat flow. Figure 3.2 also illustrates that the phonons are populated in the cell stacks as per the individual cell temperature. During initialization the first cell is maintained at hot temperature (T_h) and all other cells are set to the cold temperature (T_c).

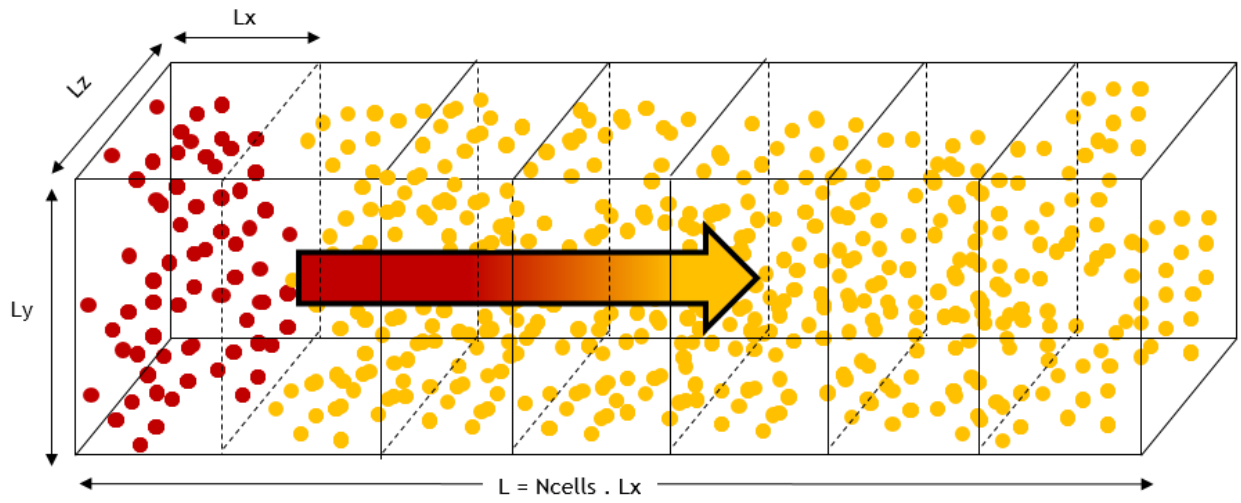

Figure 3.2 illustrates the spatial discretization of the simulated structure. The phonons initialized due to hot and cold ends are marked in red and yellow colors respectively.

Also shown is the direction of heat diffusion [58].

The MC kernel is built upon 3 prime discretization schemas namely, 1) *Spatial*, 2) *Temporal* and 3) *Spectral*.

1) *Spatial discretization* is directly related to the material geometry, where the entire structure is spatially divided to multiple spatial bins (computational control volumes) such that each bin acts as energy bin providing more granularity of the gradient in energy during the phonon drift. Generally spatial bins with Lx ~ 500 nm is used for structures at micro scale regime and can be smaller in the case of thin films or nanowires for instance.

2) *Temporal discretization* is merely time quantization of the phonon drift process, where the properties of phonons are updated after every time step so as to better capture the effects due to various scattering events. The finer the time step greater the accuracy, but it increases the computational cost considerably. The choice of time step is primarily governed by the cell size and the group velocity at a given frequency. So as to avoid phonons from drifting from the hot to cold end without colliding it is imperative that the time step (Δt) must adhere to the relation, $\Delta t < L_z/V_{gmax}$.

3) *Spectral discretization* is numerical integration of frequency space. Since the distribution function of BTE can be easily associated with energy and therefore to temperature the current algorithm is entirely based on energy considerations. For a given temperature and material, Eq. 3.2 is required to perform integration over entire frequency space for each phonon polarization which involves huge computational costs and hence the integral is reduced to summation over discrete frequency intervals thereby reducing the computational complexity. Equation 3.2 gives the *energy per unit*

volume by integrating the product of Bose-Einstein function, phonon Density of States with respect to frequency of the lattice vibrations and polarization modes of the corresponding vibration. This work employs a uniform spectral discretization with number of spectral bins (Nb) = 1000 in the range of [0,ω_{LAmax}]. Increasing the discretization further do not increase the accuracy of the results [58] [59].

$$E = V \sum_{p} \int_{\omega} \left[\frac{\hbar\omega_p}{\exp\left(\frac{\hbar\omega}{k_B T}\right) - 1} \right] \frac{K^2}{2\pi^2 v_g} \, g_p d\omega \tag{3.2}$$

In Equation 3.2 $\left[\frac{\hbar\omega}{\exp\left(\frac{\hbar\omega}{k_B T}\right)-1} \right]$ represents the Bose-Einstein function ($\langle n_{K,p} \rangle$), which describes the local thermodynamic phonons population with polarization p. The second term $\frac{K^2}{2\pi^2 v_g}$ represents the Density of States (DOS) which accounts for the number of vibrational modes in the frequency range [ω, ω + Δ ω] for polarization p and g_p corresponds to degeneracy factor (modes) for each polarization. *This work accounts for 2 modes in TA branch and 1 mode in LA branch*. On employing the spectral discretization the integral is reduced to summation over discrete frequency intervals and hence the total energy is given by Equation 3.3.

$$E = V \sum_{p=TA,LA} \sum_{b=0}^{N_b} \left[\frac{\hbar\omega_p}{exp\left(\frac{\hbar\omega_{b,p}}{k_B T}\right) - 1} \right] \frac{K_{b,p}^2}{2\pi^2 v_{g_{b,p}}} \, g_p \, \Delta\omega \tag{3.3}$$

3.3 Initialization of Phonons

Post defining the material, structure and discretization types, the most primeval step is to initialize the phonons, position them in the cells that make up the geometric domain and determining their properties. In order to initialize the phonons the equilibrium number of phonons corresponding to each cell needs to be determined [60] [64]. The numbers of phonons are obtained considering the local temperature within the cell using Equation 3.4 which is a modified expression based on Eqn. (3.3).

$$N = V \sum_{p=TA,LA} \sum_{b=0}^{N_b} \left[\frac{1}{exp\left(\frac{\hbar\omega_{b,p}}{k_B T}\right) - 1} \right] \frac{K_{b,p}^2}{2\pi^2 v_{g_{b,p}}} g_p \, \Delta\omega \tag{3.4}$$

From Equation 3.4 it can be inferred that, in order to compute the number of phonons it is essential to determine the properties of phonons such as, frequency (ω), polarization (p), group velocity (v_g), density of states ($\frac{K^2}{2\pi^2 v_g}$), position and direction.

3.3.1 Frequency and Polarization

The lattice vibrations in crystalline solids result in travelling waves of discrete frequencies (ω) which analogous to discrete energy packets as per the relation stated in Equation 3.5.

$$E = h\omega \tag{3.5}$$

These energy packets are referred to as phonons and hence it can be understood that frequency is a primary characteristic of phonons. This work determines the frequencies for phonons using 2 methods namely *(i) Empirical* and *(ii) Atomistic*

methods. Both the methods involve extracting the frequency from the dispersion relation, the only difference between them is the way to obtain the dispersion relation.

In case of Empirical methods the phonon dispersion relation is obtained from the experimental methods like neutron inelastic scattering, crystal goniometer, etc. In this work the empirical phonon dispersion relations for bulk silicon is obtained by fitting a polynomial to experimental data as formulated in Equation 3.6 [59]. The data points in the dispersion relation for Si are provided by Brockhouse [65].

$$\omega = 9280.K - 2.234 \times 10^{-7}.K^2\ (LA) \qquad (3.6)$$

$$\omega = 5240.K - 2.278 \times 10^{-7}.K^2\ (TA)$$

In case of Atomistic method, the dispersion relation is computed using KVFF approach as described in the previous chapter using NEMO 3D. NEMO 3D gives the energy values corresponding to the lattice vibrations for a given material structure. These energy values are converted to corresponding frequency values by inversion of Equation 3.5. After obtaining the ω-k relation a closest possible quadratic expression is fitted to the obtained dispersion relation data points which results in an expression similar to that of Equation 3.6.

In total there are 4 polarization modes that are generally considered, they are Transverse Optical (TO), Longitudinal Optical (LO), Transverse Acoustic (TA), Longitudinal Acoustic (LA) depending upon the axis and modes of vibration of lattice atoms as detailed in the previous chapters. *Since the group velocity of optical modes is very small they do not contribute much for the heat conduction and hence they are not considered in this work*. Since the dispersion relation corresponds to a particular polarization mode, every quadratic expression obtained corresponds to a particular

polarization mode and hence the frequencies for particular polarization modes are obtained from their corresponding dispersion relations.

3.3.2 Group Velocity and Density of states

When the dispersion relation is known the phonon group velocity and the Density of States can be determined using the Equation 3.7 & 3.8 respectively.

$$v_g(\omega, p) = \frac{\partial \omega}{\partial K} \tag{3.7}$$

The group velocity is the velocity at which the energy transport occurs or the velocity at which the lattice vibration propagate as an envelope. The group velocity is determined from the slope of the dispersion relation as illustrated in Equation 3.7. In condensed matter physics the density of states of a system describes the number of states per interval of energy [66]. From Figure 3.3 it can be inferred that each allowable wave vector (K), occupies a region of area ($\frac{2\pi}{L}$) in k space. The phonon density of states gives the number of modes available per unit frequency per unit volume of real space which is given by Equation 3.8.

$$D(\omega) = \frac{dN}{d\omega} = \frac{dN}{dK}\frac{dK}{d\omega} = \frac{KL^2}{2\pi}\frac{1}{d\omega/dK} \tag{3.8}$$

$$N(K) = \frac{\pi K^2}{(2\pi/L)^2} = \frac{K^2 L^2}{4\pi} \tag{3.9}$$

Where, N number of allowed modes for a specified volume of reciprocal space (area or volume of K space). Hence N (Equation 3.9) is given by total area of the k space divided by region occupied by each allowable wave vector i.e. ($\frac{2\pi}{L}$). In case of a

3D system the wave vector occupies a volume of $\left(\frac{2\pi}{L}\right)^3$.

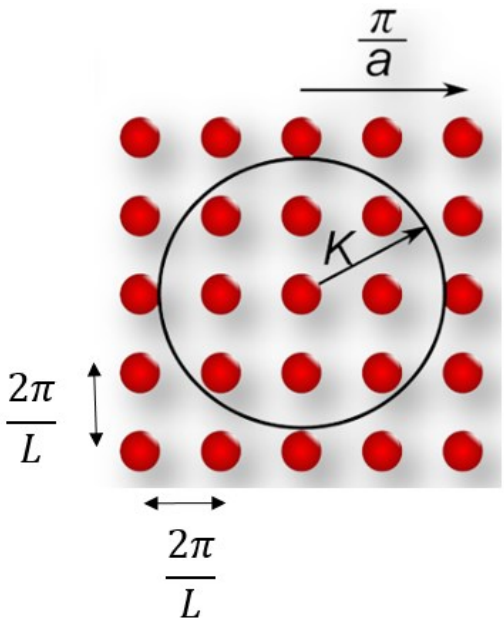

Figure 3.3 illustrates the k space in a 2D lattice.

Hence the density of states for a 3D system is given by Equation 3.10.

$$D(\omega, p) = \frac{K^2}{2\pi^2 v_g(\omega, p)} \tag{3.10}$$

After determining the group velocity ($v_g(\omega, p)$) and density of states ($D(\omega, p)$) the number of phonons in a given volume is computed using Equation 3.4 which encompasses Equation 3.7 and 3.10. Figure 3.4 plots the number of phonons as a function of their frequency. It can be observed from the figure is that the number of phonons in the media is dependent on the inherent cell temperature. Also observable is that the delta increase in phonons number decreases as we move to higher temperatures.

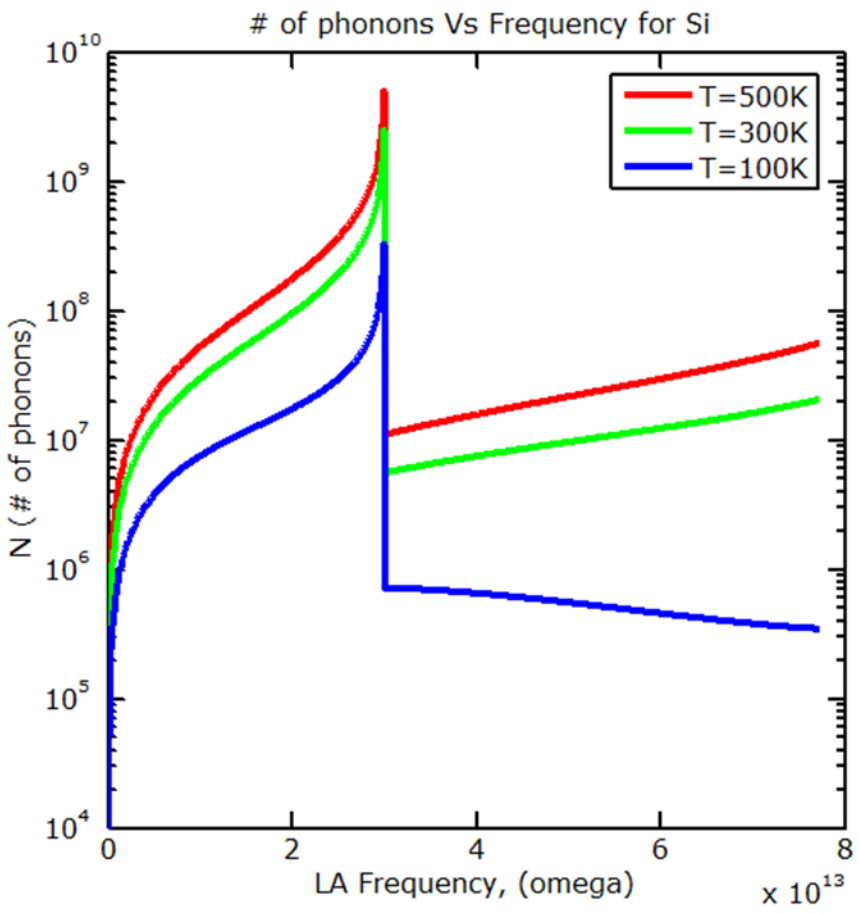

Figure 3.4 shows the number of phonons as a function of frequency and temperature.

3.4 Phonon Ensembles / Super-Phonons

It can be perceived from Equation 3.4 that the number of phonons is primarily a function of temperature and volume [58] [60]. Even for a silicon thin film at room temperature the number of phonons given by Equation 3.4 is of the order of ~10^{27} phonons per m^3, and translates to ~10^9 phonons per μm^3 [60]. These numbers are exorbitantly high from a computational point of view since tracking of seven dimensional function for 10^9 phonons requires humongous computational memory and increased processor speeds. Hence a weighting factor (W) is introduced in order to scale down the number of phonons by grouping them into ensembles or super-phonons. The

number of phonon ensembles (N_{en}) are determined by dividing the actual number of phonons (N) divided the weighting factor as shown in Equation 3.11.

$$N_{en} = \frac{N}{W} \tag{3.11}$$

Hence each super-phonon employed in the simulation actually represents an ensemble of W actual Phonons (N). So as to maintain the consistency in the simulation and to eliminate any numerical artifact the scaling factor is held constant all thought the simulation post its initialization.

3.5 Phonon Ensemble Properties

Since the individual phonons are grouped as ensembles the properties of phonons do not hold well for these super-phonons. Hence it is necessary to compute the properties for these phonon ensembles. In order to employ these super phonons to emulate heat transport properties such as, frequency (ω), polarization (p), group velocity (v_g), density of states ($\frac{K^2}{2\pi^2 v_g}$), position and direction ought to be determined.

3.5.1 Ensemble Frequency

In order to assign a frequency for a phonon ensemble the dispersion relation needs to be discretized in the frequency space. Hence the dispersion relation is sampled into N_b spectral/frequency bins in the frequency space. The number of spectral bins (N_b) considered is large such that the slope of the dispersion relation is captured precisely. In this work N_b ~ 1000 is considered, since further increase in N_b did not increase the accuracy significantly. In order to assign the frequency probabilistically to the ensembles a cumulative number density function is constructed which was

originally proposed by Mazumdar & Majumdar [68].

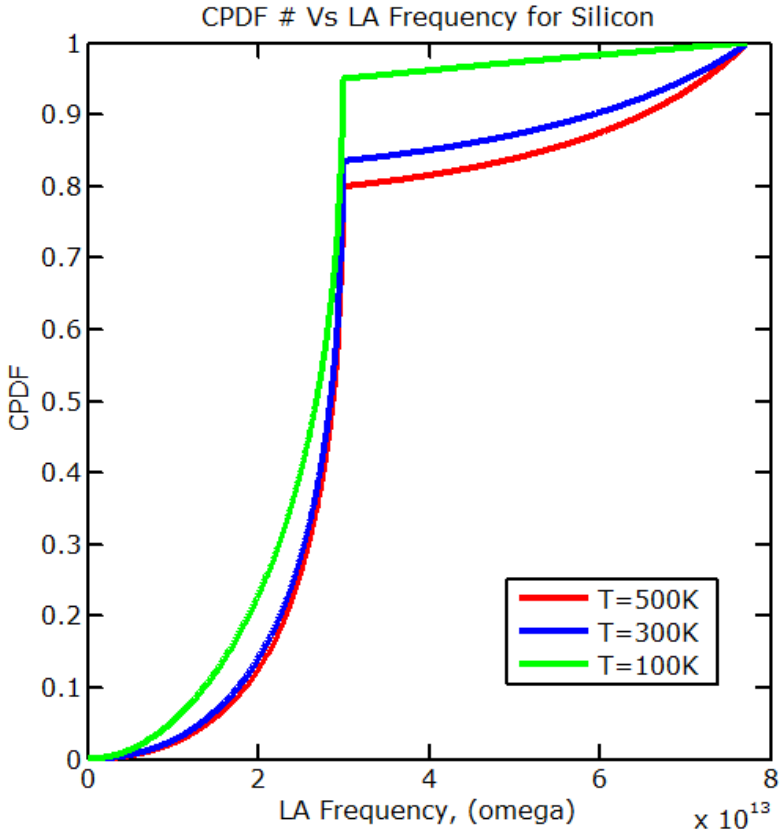

Figure 3.5 illustrates CPDF constructed as a function of varying temperature.

Normalized Cumulative Probability Density Function (CPDF) is formulated by adding up the number of phonons in the i^{th} spectral bin comprehensively and normalizing it by dividing it with total number of phonons as detailed in Equation 3.12. CPDF is computed as a function of temperature which can be inferred from Figure 3.5.

$$F_i(T) = \frac{\sum_{j=1}^{i} N_j\,(T)}{\sum_{j=1}^{N_b} N_j\,(T)} \tag{3.11}$$

Where F_i represents the probability of finding a phonon at a particular frequency interval which is referred to as the i_{th} interval which spans between the central frequency

($\omega_{o,i}$) of the i^{th} interval and the central frequency of the $(i+1)^{th}$ interval ($\omega_{o,i} + \Delta\omega$) and N_j is given by Equation 3.12.

$$N_j = \sum_p \frac{1}{\exp\left(\frac{\hbar\omega_{0,i}}{k_b T}\right) - 1} \frac{|K|^2}{2\pi^2} \left|\frac{d|K|}{d\omega}\right|_{\omega_{0,i}} \Delta\omega_i \, g_p \tag{3.12}$$

In order to assign a frequency to the phonon ensemble randomly, a random number R_f, between zero and unity, is drawn. Then a binary search algorithm is employed to obtain the i^{th} frequency interval from the CPDF for the corresponding R_f, post which the central frequency ($\omega_{o,i}$) of the i^{th} interval is determined numerically ($\omega_{o,i} = \frac{\omega_i + \omega_{i+1}}{2}$). The frequency interval is zeroed in such that $F_{i-1} < R_f < F_i$, thereby constraining the phonon into the i^{th} frequency bin. Once the spectral bin has been determined, the frequency of the phonon is calculated using Equation 3.13.

$$\omega = \omega_{0,i} + \left(2R_f - 1\right)\frac{\Delta_{\omega_i}}{2} \tag{3.13}$$

3.5.2 Ensemble Polarization

Post defining the frequency of the ensemble it is imperative to assign a polarization mode to the ensemble. In order to achieve that another probability function is drawn such that, the probability of a polarization p, in the i^{th} spectral interval is given by the ratio of number of phonons with polarization p in the i^{th} interval over total number of phonons in the i^{th} spectral interval as stated by Equation 3.14 [60].

$$P_{i,p} = \frac{N_{i,p}}{N_i} \tag{3.14}$$

This work assumes that the function is initially drawn for LA polarization mode. Hence the Equation 3.14 transforms as [58] [59],

$$P_{LA}(\omega_i) = \frac{N_{LA}(\omega_i)}{N_{LA}(\omega_i) + N_{TA}(\omega_i)} \quad (3.15)$$

After probability function a new random number R_p is drawn, such that, if $R_p <$ $P_{LA\,(\omega)}$ the phonon ensemble is assigned to the LA branch otherwise it is assigned to TA branch. Once the frequency and polarization is determined the phonon group velocity and density of states can be estimated using Equations 3.6, 3.7 and 3.9.

3.5.3 Ensemble Position

In order initialize phonons, primarily the control volume needs to discretize spatially into individual control cells. Since this work considers a rectangular parallelepiped, after spatial sampling it appears as stacked cells. So as to initialize and position the phonons spatially into each cell in Cartesian coordinates 3 random numbers are put to use. Equation 3.16 [60] is used to determine the coordinates of the phonon ensembles in the regulated volume [60].

$$r = R_1(x_{OB} - x_{OA})\hat{\imath} + R_2(y_{OB} - y_{OA})\hat{\jmath} + R_3(z_{OB} - z_{OA})\hat{k} \quad (3.16)$$

Where r, represents the 3 dimensional Cartesian coordinates of the phonon ensemble; R1, R2 & R3 are random numbers such that 0 < R1, R2 & R3 < 1; OA & OB are the body diagonal of the rectangular parallelepiped as illustrated in Figure 3.6 [60].

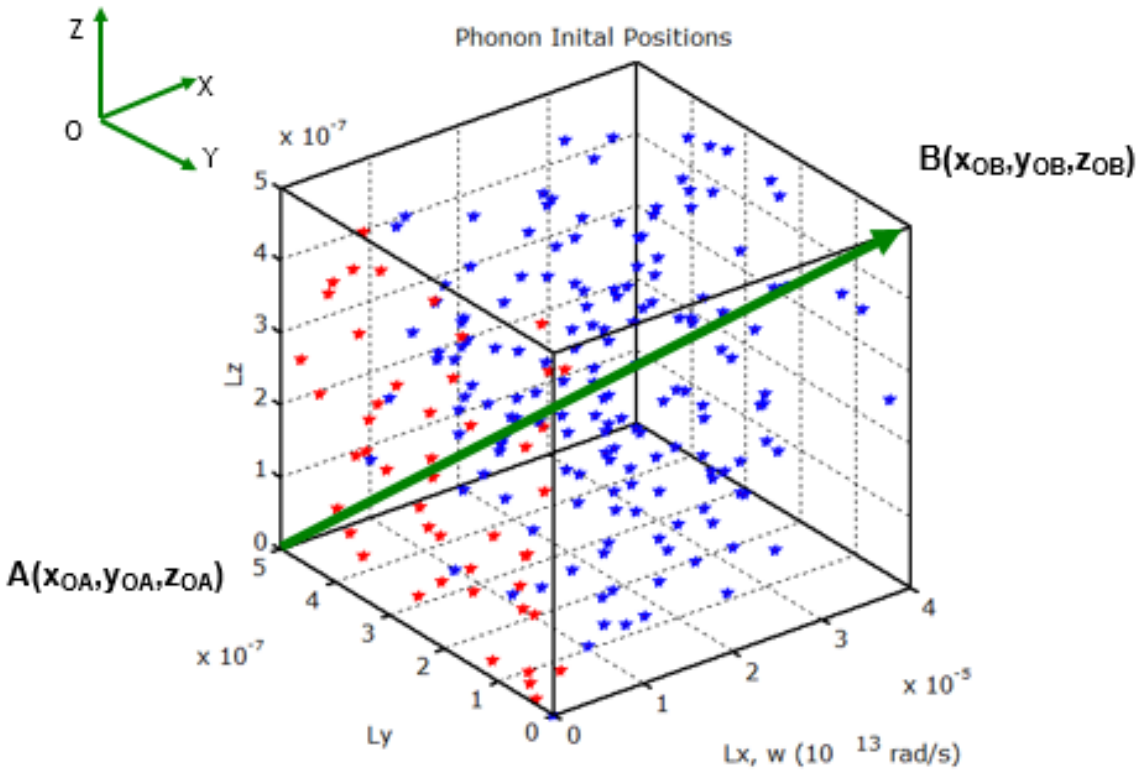

Figure 3.6 illustrates the initial position of the phonon ensembles along with the position vectors of body diagonal.

3.5.4 Ensemble Direction

Prior to initializing the phonon drift it is necessary to assign the phonon ensembles the launching angles or direction of drift. All initial launching angles are presumed to be isotropic or uniform in all directions. Phonons that are launched from the isothermal boundary can be either isotropic or diffuse (non- uniform) [59].

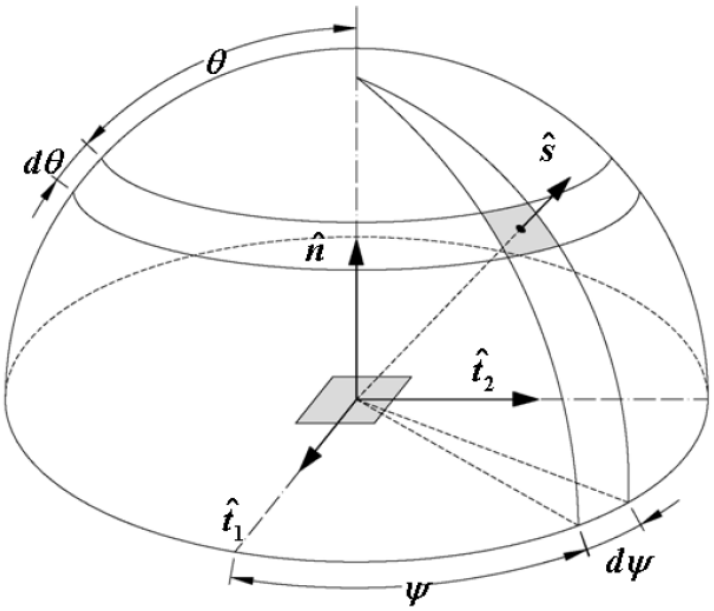

Figure 3.7 illustrates the coordinates for projection of phonons in hemispherical solid angle during phonon emission [60].

A hemispherical solid angle (as shown in Figure 3.7) is used to sample the initial launching angles, such that the total angle of emission is defined by Equation 3.17 [59].

$$\int_0^{2\pi} \int_0^{\pi/2} cos\theta \; sin\theta \; d\theta \; d\varphi = \; \pi \tag{3.17}$$

Where cosθ, represents the surface area of phonon emission at varying angles of θ. On constructing a probability density function based on Equation 3.17 yields,

$$R(\theta) = \int_0^{\theta} cos\theta' sin\theta' d\theta' = sin^2\theta \tag{3.18}$$

On considering R (θ) as a random number between zero and unity the polar angle of emission (θ) is determined (Equation 3.19) [59]. Similarly the azimuthal angle (φ) is also determined (Equation 3.20) from the probability density function [59].

$$\theta = \; \sin^{-1}\sqrt{R_\theta} \tag{3.19}$$

$$\varphi = 2\pi R_{\varphi} \tag{3.20}$$

Where R_θ and R_φ are random numbers between zero and unity. On determining the polar and zenith angle the direction of the wave vector is churned out using the following relations,

$$\mu_x = cos\theta \tag{3.20}$$

$$\mu_y = sin\varphi\ sin\theta \tag{3.21}$$

$$\mu_z = cos\varphi\ sin\theta \tag{3.22}$$

3.6 Drift

After initializing the phonon ensembles and defining their properties, the ensembles are allowed to drift from their respective position towards the colder end. The drift of phonon ensembles inside the nanostructure is emulated using an explicit 1st order time integration equation based on Equation 3.23 [58] [60].

$$r_{drift} = r_{old} + v_g.\Delta t \tag{3.23}$$

Where v_g is group velocity, Δt represent the time step for which the phonon ensembles are allowed to drift, r_{old} is the initial position of ensemble at time instant t and r_{drift} the position of the same ensemble at t+Δt instant [60]. Assuming the phonon ensemble interactions with the boundary to be isotropic the probability of the ensemble scattering angle is distributed uniformly in all directions and hence the direction cosines and the mean free path ($\lambda = v_g.\ \Delta t$) are pivotal in determining the final positions of the ensembles. The afore-mentioned dependency is elaborated in Equation 3.24, 3.25 & 3.26 [59].

$$x_{new} = x_{old} + \mu_x.\lambda \tag{3.24}$$

$$y_{new} = y_{old} + \mu_y.\lambda \quad (3.25)$$

$$z_{new} = z_{old} + \mu_z.\lambda \quad (3.26)$$

Due to the drift of phonon ensembles the ensembles may end up in different spatial bin than the one they started, thereby resulting in re-distribution of energy and hence the temperature in the spatial bins within the computational domain.

At the end of the drift phase the phonon ensembles are assigned with their final position vector with the corresponding spatial bin associated with the new position vector which is illustrated in Figure 3.8. Figure 3.8 is better understood when compared with the initial ensemble positions shown in Figure 3.6.

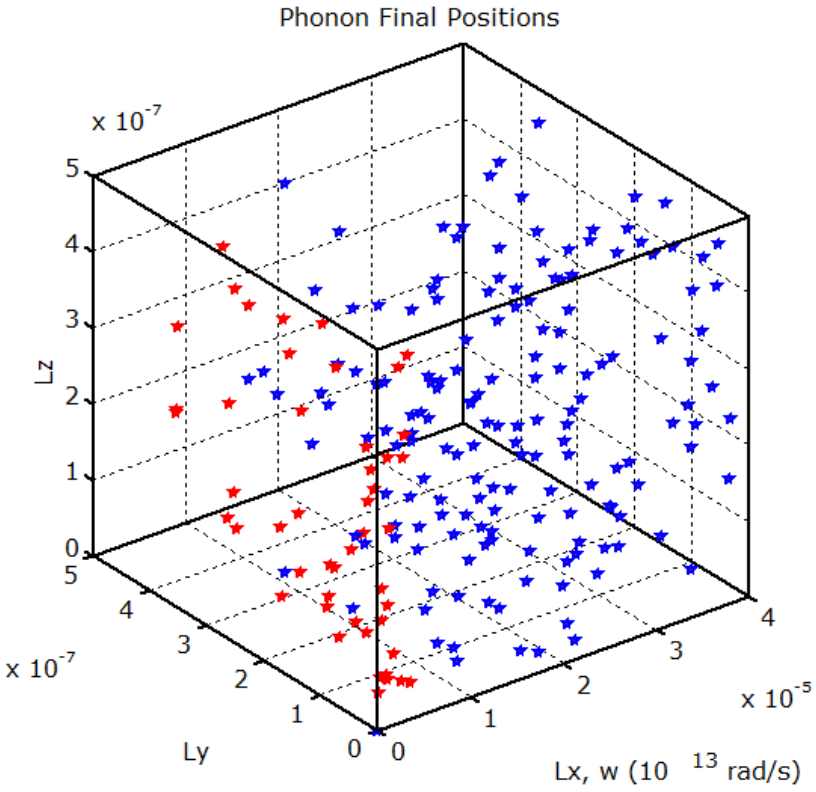

Figure 3.8 shows the final position of the phonon ensembles at the end of the drift phase.

At the end of the drift phase the energy (E) of the total computational volume is

determined by summation of the energy (E_{cell}) of local spatial bins. E_{cell} is computed by summation of Einstein's relation for all phonon ensembles contained in a local control volume/spatial bin as per Equation 3.27 [58].

$$E_{cell} = \sum_{c=1}^{N_{cell}} \sum_{n=1}^{N^*} W \,.\, \hbar\omega_{n,c} \tag{3.27}$$

Where, N^* represents the number of phonons in spatial bin and N_{cell} represents the total number of spatial bins that the control volume encapsulates. This energy E_{cell} needs to match the total energy of the nanostructure computed using Equation 3.3. Also observable from Equation 3.7 is the product of scaling factor W, since the phonons are added in packs thereby, computed cell energy is due to phonons and not due to phonon ensembles. The developed MC code also has the ability to visually track the position of phonons in 3D during the drift phase which is plotted in Figure 3.9. This visual tracking of phonons serves as a good debug tool.

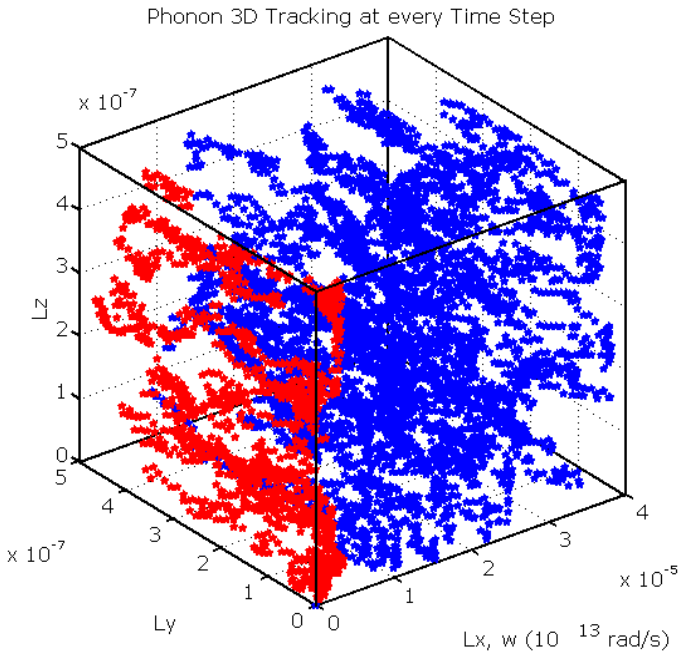

Figure 3.9 shows the position of phonons at every time step (∆t) during the drift phase inside the control volume

3.7 Scattering

As the phonon ensembles drift inside the nanostructure, they interact with the structural boundaries, atomic impurities and other phonons. Of the 3 aforementioned primary scattering events, the interactions with boundaries and crystal defects or impurities influence only the direction / momentum of the phonon ensembles without modifying the inherent frequency of the associated ensembles [58]. Hence the boundary scattering is accounted for during the drift phase itself, whereas the phonon-phonon scattering is decoupled from the drift process thereby splitting the transport and scattering operators [60]. Thus BTE is decoupled into two equations, 1) Free-Flow Equation (Equation 3.28) and, 2) spatially homogeneous Boltzmann equation (Equation 3.29) [60]. Both the equations are solved sequentially such that the solution of Equation 3.28 provides the input to Equation 3.29 [60].

$$\frac{\partial f}{\partial t} + v_g \,.\, \nabla f = 0 \tag{3.28}$$

$$\frac{\partial f}{\partial t} = \left[\frac{\partial f}{\partial t}\right]_{scatter} = \frac{f - \langle n \rangle}{\tau(\omega)} \tag{3.29}$$

Where f, represents the Boltzmann distribution function, $\langle n \rangle$ represents Bose-Einstein distribution function and $\tau(\omega)$ represents the frequency dependent relaxation time. The relaxation time computed in this work steps beyond the grey medium approximation in which the relaxation time, τ is only dependent on temperature. This work emphases the frequency dependent model developed by *Chen et al* [61].

$$\frac{1}{\tau_T(\omega)} = \frac{1}{\tau_U(\omega)} + \frac{1}{\tau_N(\omega)} \tag{3.30}$$

Equation 3.30 represents the cumulative relaxation time due to individual scattering events such as phonon-phonon scattering U process, $\tau_U(\omega)$ and phonon-phonon scattering N process, $\tau_N(\omega)$. The aforementioned scattering events are in inelastic in nature due to their inherent anharmonicity and hence resulting in change of phonon energy, frequency and hence the group velocity. On contrary the boundary scattering is elastic in nature, where only the direction of the phonon drift is affected whereas the phonon frequency remains unaltered.

3.7.1 Boundary Scattering

During the drift the phonons or phonon ensembles (packets containing W phonons) interact with boundaries elastically, resulting in altercation of the phonon ensemble momentum only. Boundary interactions are predominantly significant since at low temperature where the phonon-phonon interactions are negligible, boundary interactions offer the only resistance to heat flow. As stated in section 3.2, two types of boundaries are considered in this work namely isothermal boundaries and adiabatic boundaries. The boundaries are illustrated in Figure 3.10.

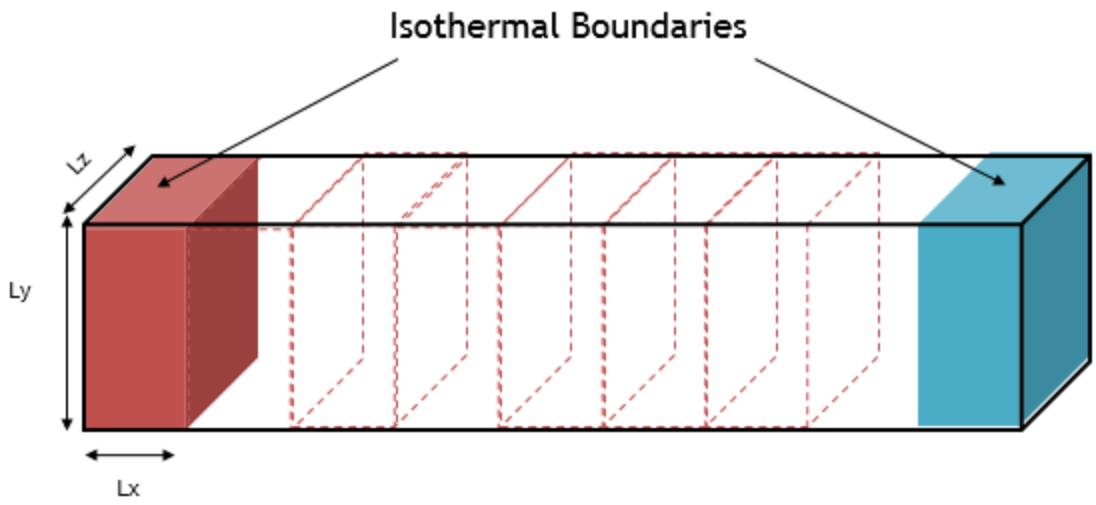

(a)

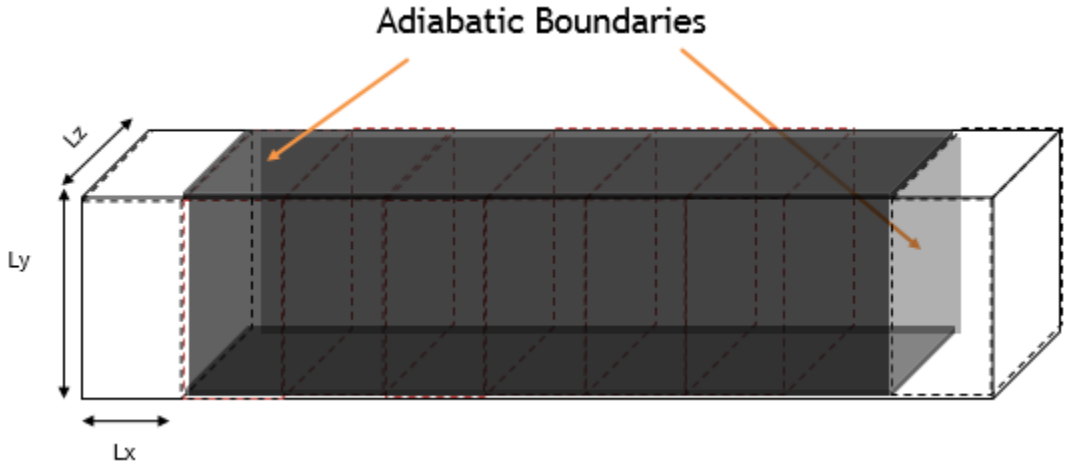

(b)

Figure 3.10 illustrates (a) Isothermal boundaries and (b) Adiabatic boundaries employed in this work

As described earlier the isothermal boundaries absorb phonons impinging on them and emit phonons at every Δt, depending on the cell temperature in order to maintain thermal equilibrium. The end faces along the x direction are assumed to be isothermal boundaries in this work. The heat is assumed to flow in the positive X direction and hence end up impinging the boundary at the cold face. Also some phonons are backscattered to the –ve x direction towards the hot face. This results in

depletion of phonons in the computational domain and hence necessitates the need to add phonons into the domain so as to maintain the heat flow during the simulation. The number of phonons emitted by the isothermal boundaries at every time step (Δt) is given by the following Bose-Einstein distribution in Equation 3.31 [60].

$$N_{face}(T) = A\,.\,\Delta t\,.\left(\sum_{p}\sum_{i=1}^{N_b}\langle n(\omega_{0,i},p,T)\rangle\langle v_g(\omega_{0,i})\,.\,\hat{n}\rangle D(\omega_{0,i},p)\Delta\omega_i\right) \tag{3.31}$$

In Equation 3.31 the Bose-Einstein function ($\langle n\rangle$) is dependent on the local boundary temperature. Also Equation 3.31 uses an averaged phonon group velocity ($\langle v_g(\omega_{0,i})\,.\,\hat{n}\rangle$) normal to the face of isothermal boundaries. Since the phonons are emitted into the computational domain using the hemispherical solid angle (Equations 3.20, 3.21 and 3.22), the phonons are emitted in all directions and hence they are required to be directionally averaged (using Equation 3.32 [60]) to compute the group velocity normal to the emitting face.

$$\langle v_g(\omega_{0,i})\,.\,\hat{n}\rangle = \begin{cases} 1/\pi\ |v_g| \\ 1/4\ |v_g| \end{cases} \tag{3.32}$$

Another facet of phonon-boundary scattering is the interaction of phonons with adiabatic boundaries. Primarily adiabatic boundaries prohibit the heat flux through the surface and hence the interacting phonons need to be reflected on striking the boundary wall.

In symmetric structure such as a rectangular parallelepiped the 4 side walls of the structure along the Y and Z direction reflect specularly or diffusively depending on the roughness of the boundary (δ). The degree of specularity for every phonon-boundary interaction is determined using a random number R_{spec} chosen between 0 and

unity. The roughness of the boundary is assumed to be 0.5 in this work. Hence if R_{spec} < roughness of boundary (δ = 0.5) the phonon is specularly reflected else it is diffusively reflected. Figure 3.11 (a) & (b) describes the specular and diffusive reflection. In case of specular reflection the phonon experiences mirror like reflection as dictated by Equation 3.33.

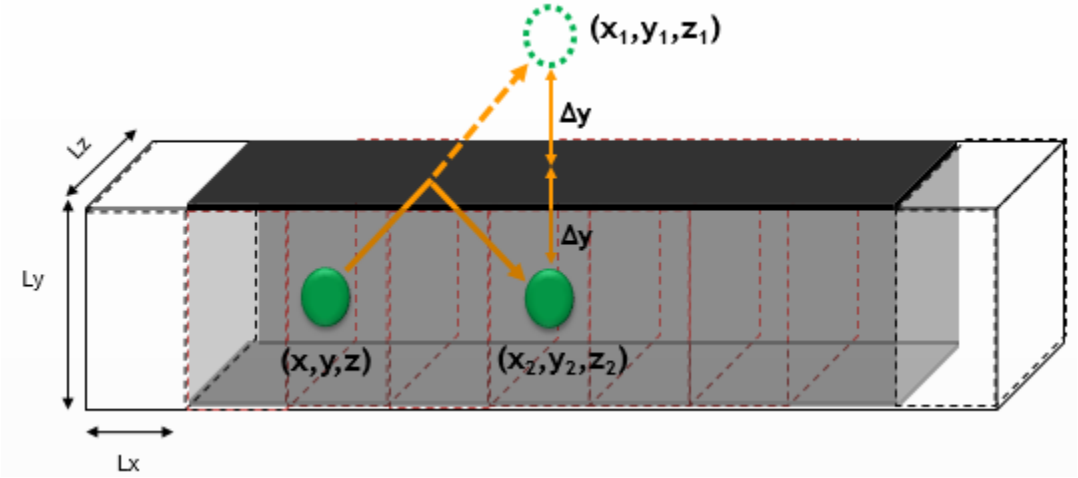

(a)

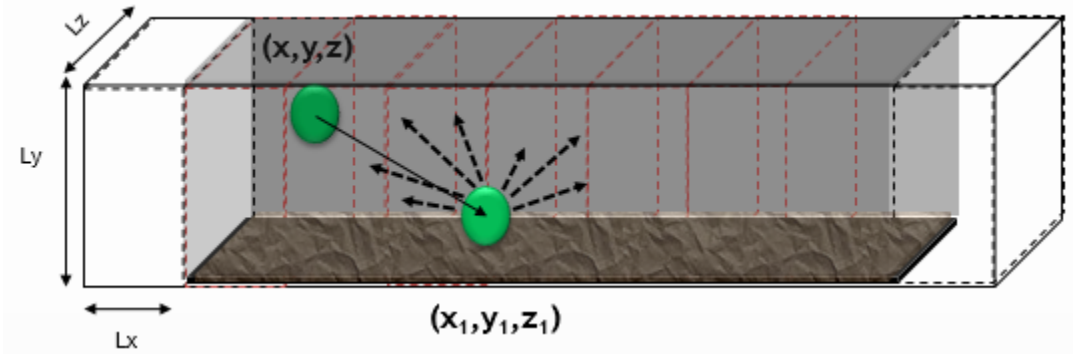

(b)

Figure 3.11 illustrates the phonon reflection (a) specularly in a smooth surface and (b) diffusively in a rough surface. Also both (a) & (b) depict a sample phonon incident and reflection paths with the probable projection angles.

Figure 3.11 (a) details the specular reflection of a single phonon inside the

simulated structure. A simple numerical scheme is employed to compute the specularly reflected final position of the phonons. In Figure 3.11 (a) (x,y,z) represent the initial position of the phonon, (x_1,y_1,z_1) represents the projected position of the phonon after the phonon drift of 1 mean free path (λ) based on Equations 3.24, 3.25 & 3.26, (x_2,y_2,z_2) represents the final position of the specularly reflected phonon by employing Equation 3.33 and Δy is the distance between the boundary of the structure (L_y in case of +ve y axis as per Figure 3.11 (a)) and the projected spatial coordinate along the axis of consideration (as per Figure 3.11 (a), it is y_2 since the phonon drifts along the +ve y axis).

$$y_2 = y_1 - (2 \,.\, \Delta y) \tag{3.33}$$

Similarly, the specular reflection along the other 3 axes –y, +z & -z are computed. In case of a diffuse reflection as illustrated in Figure 3.11 (b), the phonons are allowed to backscatter along the direction of phonon drift. For this purpose the polar angle (θ) is modified according to Equation 3.34, whereas the azimuthal angle (φ) remains the same. After determining θ, Equations 3.20 – 3.26 are followed to obtain the final diffusively reflected position for the phonons.

$$\theta = \cos^{-1}(1 - 2R_\theta) \tag{3.34}$$

3.7.2 Impurity Scattering

Phonon interacts with impurities elastically inflicting changes only to the direction of phonon propagation. The change in direction of the phonon due to impurity scattering is captured in the polar angle using Equation 3.34. The azimuthal or zenith angle is obtained using Equation 3.20. A random number (R_{imp}) between 0 and unity is drawn for

every phonon at each time step of drift and compared with a predefined probability of impurity scattering (P_{imp}). If $R_{imp} < P_{imp}$, the phonon direction is left unaltered, else new position vectors are assigned based on Equation 3.20 - 3.26 & 3.34. Impurity & boundary scattering are significant at low temperatures where the phonon mean free path grows larger than the structural size.

3.7.3 Phonon-Phonon Scattering

Phonons in the system interact with other phonons resulting in a inelastic scattering. Current work isolates the drift and elastic scattering with that of inelastic scattering processes. The phonon-phonon scattering or intrinsic scattering is primarily governed by two processes namely Normal (N) process and Umklapp (U) process. Both these process aim at restoring equilibrium to the system, since they follow energy and momentum conservation [59]. This work takes into consideration of phonon scattering events as dictated by both N and U processes so as to account for the anharmonicity of interatomic forces and inherent atomicity of the crystal lattice. The 3 phonon interactions involve either merging two phonons to form the third phonon or decomposing one phonon to two phonons as stated in Equation 3.35 [58] [59]. The N process involves conservation of momentum whereas U process does not conserve momentum and results in backscattering thereby resisting the heat conduction which is illustrated in Figure 3.12.

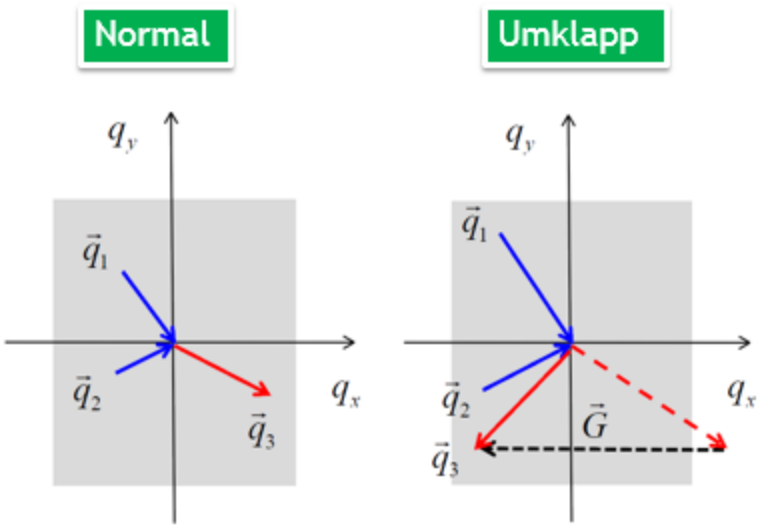

Figure 3.12 illustrates the three phonon scattering due to N and U processes. In the figure q_1, q_2, and q_3 represent the momentum vectors of 3 phonons respectively [67] [69].

Hence in case of phonons described by polarization, frequency and wave vector (p_1, ω_1, q_1) and (p_2, ω_2, q_2), the final scattering state (p_3, ω_3, q_3) is given by Equation 3.35 [58] [59].

$$\begin{cases} energy: \hbar\omega_1 + \hbar\omega_2 \leftrightarrow \hbar\omega_3 \ (N + U) \\ N\ process: q_1 + q_2 \leftrightarrow q_3 \\ U\ process: q_1 + q_2 \leftrightarrow q_3 + G \end{cases} \tag{3.35}$$

Where ω_1, ω_2, ω_3 are the angular frequencies of the interacting phonons and G is the lattice reciprocal vector. It can be observed from Equation 3.35 that the process is reversible. Capturing three phonon process and to track them individually for a realistically sized structure with ~10^6 phonons is a computational nightmare and hence Relaxation Time Approximation (RTA) is employed.

In this work the inverse of total relaxation time ($\tau_T(\omega)$), is a cumulative sum of individual inverse relaxation times for N & U scattering processes as dictated by Mathiessen rule (Equation 3.30). The relaxation times for the N & U process are

computed by expressions proposed by *Holland et al [70]* for three phonon processes. The inverse relaxation times for N and U process are given by Equation 3.36 [59], 3.37 [59], and 3.38 [59].

$$\tau_{NU}{}^{-1} = B_L\,\omega^2\,T^3 \tag{3.36}$$

$$\tau_N{}^{-1} = \begin{cases} B_{TN}\,\omega T^4 & \forall\ \omega < \omega_{1/2} \\ 0 & \forall\ \omega \geq \omega_{1/2} \end{cases} \tag{3.37}$$

$$\tau_U{}^{-1} = \begin{cases} 0 & \forall\ \omega < \omega_{1/2} \\ \dfrac{B_{TU}\omega^2}{\sinh(\hbar\omega/k_B T)} & \forall\ \omega \geq \omega_{1/2} \end{cases} \tag{3.38}$$

Where B_L, B_T, & B_{TU} are constants derived from bulk thermal conductivities obtained from *Ashegi et al* [72] and $\omega_{1/2}$ is the frequency at $k/k_{max} = 0.5$. Equation 3.36 illustrates the inverse relaxation times for N & U process of LA phonons. Equations 3.37 and 3.38 represent the inverse relaxation times of TA phonons for N & U process respectively.

In order to select the phonons/phonon ensembles that will undergo intrinsic or phonon-phonon scattering, a scattering probability is formulated using Equation 3.39 [58] [61].

$$P_{scat} = 1 - \exp\left(\frac{-\Delta t}{\tau_T(\omega)}\right) \tag{3.39}$$

Equation 3.39 is computed for each phonon/phonon ensemble to deduce the scattering probability of that particular phonon depending upon the frequency of that particular phonon between t and t + Δt. After determining the scattering probability (P_{scat}) a random number R_{scat} is drawn, such that if $R_{scat} < P_{scat}$, the phonon is scattered, else the phonon remains unperturbed. If the ensemble is scattered the frequency/energy of the ensemble is reset and hence polarization and group velocity are also required to be

recomputed. The intrinsic scattering resets the phonon energy creating an imbalance in the total energy of the structure [59]. In order to counter the imbalance created due to creation/destruction of energy during the intrinsic scattering the existing CPDF is modified in line with Equation 3.40 as proposed by *Larcoix et al [58]*.

$$F_{scat}(\tilde{T}) = \frac{\sum_{j=1}^{i} N_j(\tilde{T}) \,.\, P_{scat,j}}{\sum_{j=1}^{N_b} N_j(\tilde{T}) \,.\, P_{scat,j}} \tag{3.40}$$

Where $\tilde{T}$, is the local temperature of the cell post drift and hence each cell has its individual CPDF which can be observed in Figure 3.12. Equation 3.40 aims at restoring thermal equilibrium by enabling the phonons with higher scattering rates to have higher probabilities of being drawn towards the equilibrium [59]. To summarize the scattering process, at the end of drift phase certain number of phonons are picked from each cell based on Equation 3.39 and their properties are reset to impose the effect of scattering. Hence the energy of the control volume post scattering is obtained using Equation 3.41.

$$E''^{*} = \sum_{i=1}^{N\prime^{*}_{scat}} \hbar\widetilde{\omega\imath} + \sum_{i=1}^{N\prime^{*} - N\prime^{*}_{scat}} \hbar\omega i \tag{3.40}$$

Where, N'^{*}_{scat} is the total number of scattered phonons in the control volume, $N'^{*}$is the total number of un-scattered phonons in the control volume and $\widetilde{\omega_\imath}$ is frequency of scattered phonons at the end of scattering phase. Also the individual cell energies are obtained using Equation 3.3 and the individual cell temperatures are obtained by numerical inversion of Equation 3.3.

CHAPTER 4

RESULTS AND DISCUSSION

The accuracy in modeling the thermal transport begins at the atomic level, since the atoms are oscillating at discrete phase and frequencies. So as to pin down to a more accurate phonon dispersion relation, it is imperative to employ a model that can operate beyond harmonic approximation which is relatively much closer to reality. Henceforth this work employs a *quasi-anharmonic model* to compute the phonon dispersion relation, which serves as a foundation to comprehend the phonon transport in a system. In order to emulate the quasi-anharmonic behavior Molecular Mechanics based NEMO-3D is put into task. The following section presents the results of Keating Valance Force Field method and Monte-Carlo Simulations for Silicon (Si), Galium Nitride (GaN) and Bismuth Telluride (Bi_2Te_3) at reduced structural dimensions.

4.1 Dispersion Relation (ω-q) – NEMO-3D

Atomistic Nano-Electronic Modeling tool (NEMO-3D) is used to compute the dispersion relation using Keating Valance Force Field (KVFF) approach. In this work optical phonons are not considered owing to their low group velocity and hence they do not significantly contribute towards thermal transport. Figure 4.1 shows the comparison between empirically fitted dispersion relation and the dispersion relation computed using the KVFF approach for Longitudinal (LA) and Transverse (TA) Acoustic branches bulk Silicon. It can be observed from Figure 4.1 that the despite describing LA branch reasonably well for Si, TA branch computed using KVFF model does not flatten out at the Brillouin Zone edge when compared to empirically fitted curve.

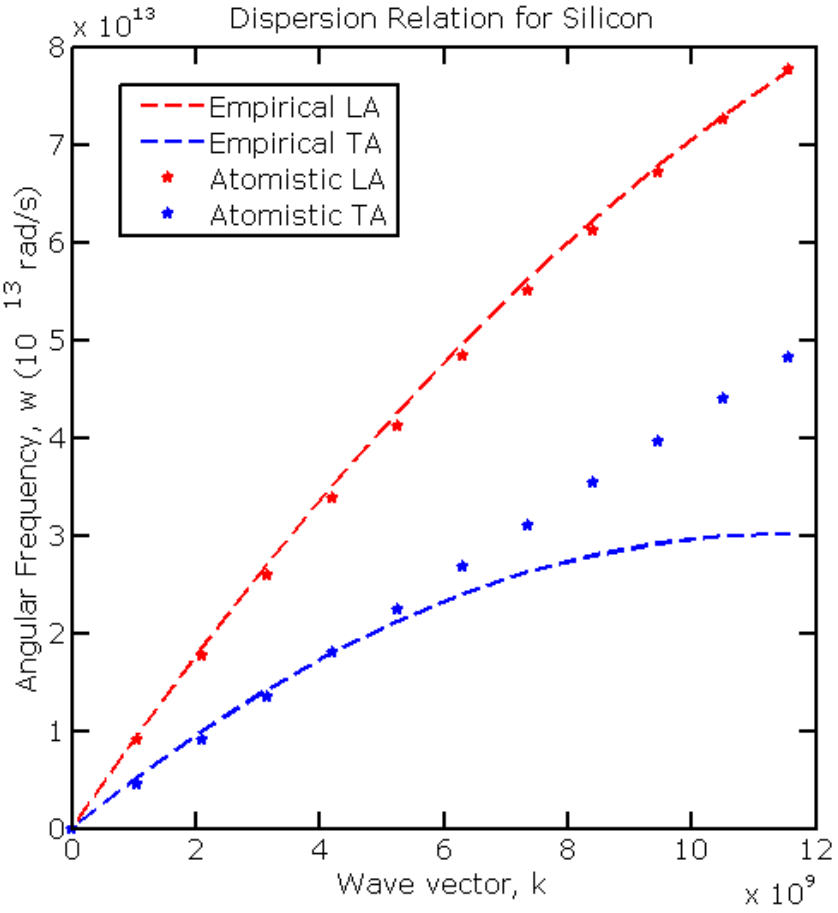

Figure 4.1 Comparison of Silicon dispersion relation between empirical and molecular mechanics (KVFF) based approach.

Since the KVFF model reproduces the Transverse Acoustic (TA) branch accurately near the Brillouin Zone center with a minor overestimation of ~7% near the zone edge, it still fits the bill, if it was to be considered as Debye approximation. Also the aforementioned arguments are valid only to zinc-blende crystal structures. Figure 4.2 illustrates the full band phonon dispersion with both optical and acoustic modes for GaN nanowire. Phonon dispersion relations are of paramount significance since the fundamental

phonon properties such as phonon group velocity, phonon density of states, etc. are extracted from these discrete dispersion modes.

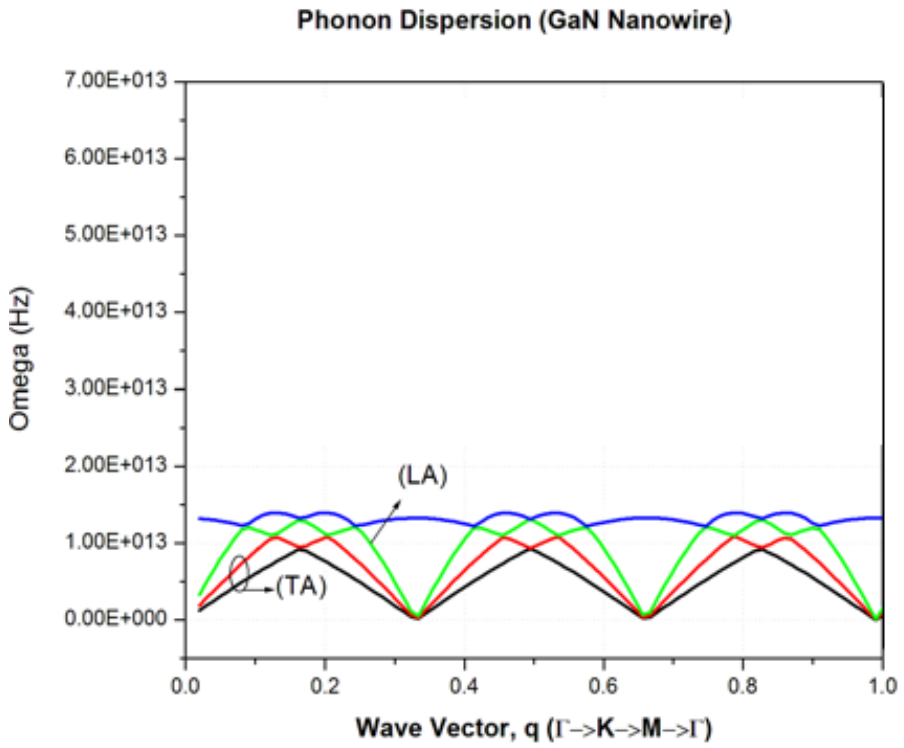

Figure 4.2 shows phonon dispersion for acoustic modes GaN nanowire.

The slope of the dispersion curve determines the group velocity. Owing to mild slope in optical modes, they result in very low group velocity and hence the optical modes are not accounted for in this work so as to model the heat transport.

4.2 Validation of MC Technique

In order to gain confidence in statistical solution of BTE, it is important that the Monte-Carlo (MC) code needs to be verified against analytical solutions for limiting scenarios. The code is primarily validated at both *ballistic* and *diffusive* regimes for Si thin films.

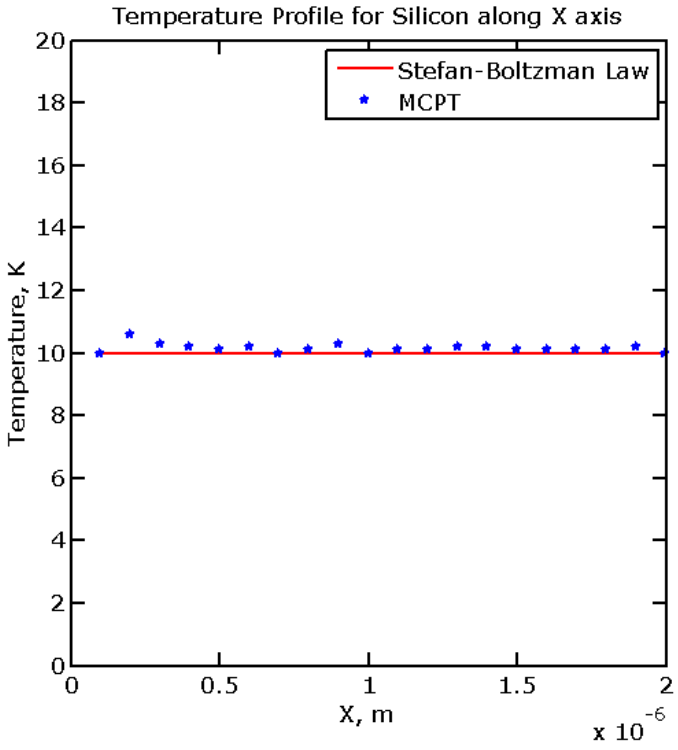
Temperature Profile for Silicon along X axis
Stefan-Boltzman Law
MCPT
Temperature, K
X, m
x 10^-6
0
2
4
6
8
10
12
14
16
18
20
0
0.5
1
1.5
2

(a)

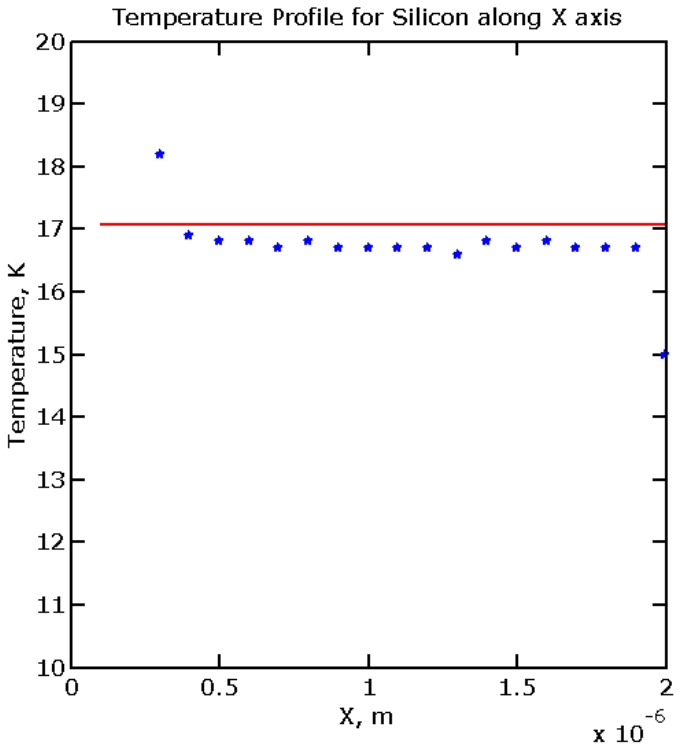
Temperature Profile for Silicon along X axis
Temperature, K
X, m
x 10^-6
10
11
12
13
14
15
16
17
18
19
20
0
0.5
1
1.5
2

(b)

Figure 4.3 illustrates the comparison between temperature profile computed using MC and SBL for Si thin film (a) when both ends are maintained at 10K and (b) when hot end is maintained at 20K and cold end at 10K.

Figure 4.3(a) exemplifies the ballistic nature in its temperature profile along the length of the thin film when both ends of the film are maintained at constant temperature (10K-10K). In case of ballistic limit when the mean free path of phonons is much larger than film thickness, the code reproduced a temperature profile that agrees to that of Stefan-Boltzman Law (SBL) [73]. It can be observed that at lower temperature the MC code agrees well with the analytical solutions at the ballistic regime. After validating at ballistic limit it is important to validate at diffusion limit as well, and for this purpose the structure is simulated with large temperature differences by maintaining hot end at 500K and cold end at 250K. Figure 4.4 illustrates the temperature profile at diffusion limit.

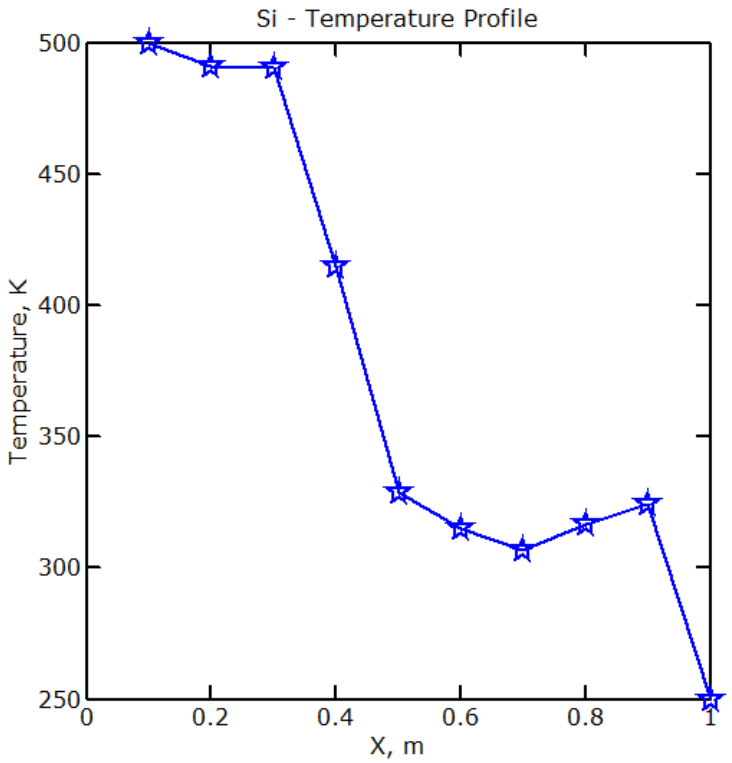

Figure 4.4 Temperature profile at diffusion limit when the hot and cold ends are maintained at 500K and 250K respectively

Since the conductivity varies with temperature according to power law in case of Si. It is evident that having a large thermal gradient across the structure will not result in a purely linear solution which is manifested in Figure 4.4. Figure 4.5 illustrates the temperature diffusion as a function on position and time steps. It can be observed from the figure that as the time increases the heat diffuses further into the colder regions which illustrates the rate at which the diffusion occurs.

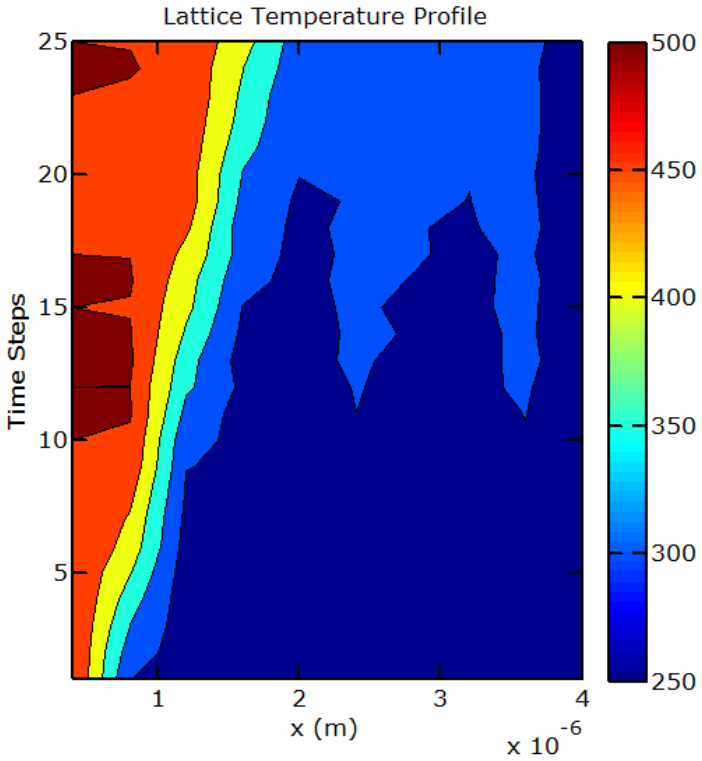

Figure 4.5 shows 2-D contour of heat diffusion as a function of time steps and length of the Si thin film

Since the drift and the phonon-phonon scattering process has been decoupled in this work, it would make more sense to have a sanity check on the phonon-phonon scattering rates. In order to ensure the correct calculation of scattering rates, as an

experiment the number of phonons in the media is increased thereby increasing the probability of phonon-phonon scattering which results in shorter Mean Free Path (λ) and lower thermal conductivity. So as to increase the number of phonons in the medium, the end temperatures are raised to 300 K and 100 K. From Figure 4.6 it can be appreciated that the as the temperature increases the relaxation time (τ) decreases, which gives us a confidence on proper treatment of the phonon-phonon scattering rates.

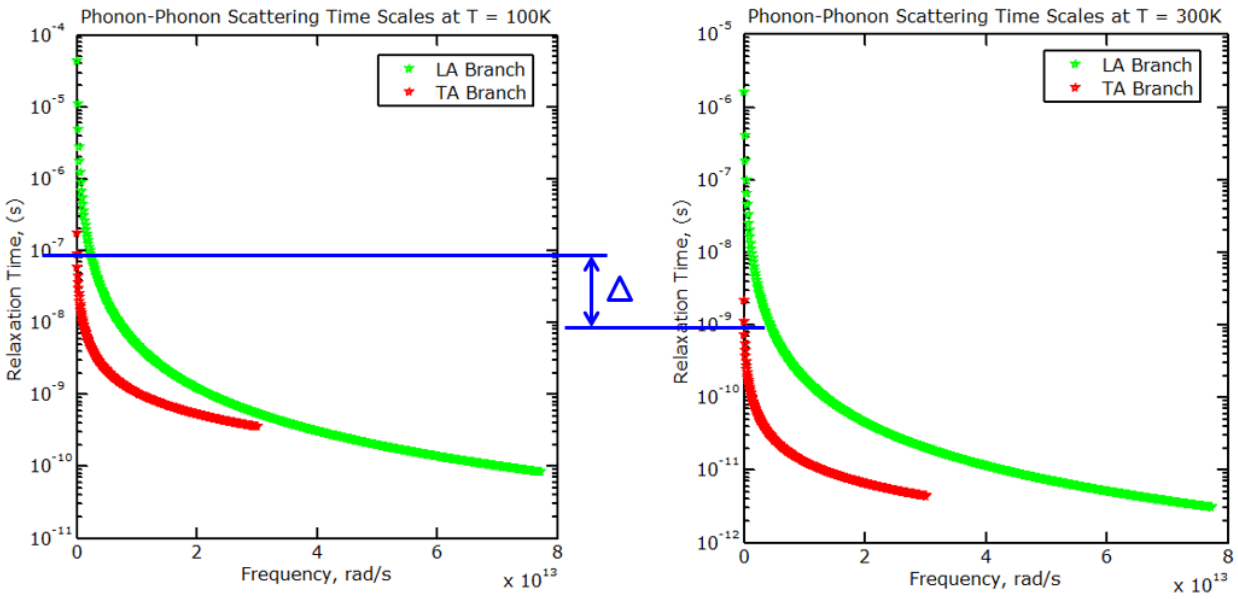

Figure 4.6 illustrates the Relaxation time (τ) for temperatures 100 K and 300 K respectively

4.2.1 Low Temperature Transient Simulations

At low temperature the phonon-phonon scattering has very little effect on heat transport in the media. This can be interpreted in much simpler way such as when the Temperature (T) decreases, the number of phonons decreases, thereby resulting in attenuated phonon-phonon scattering events. Hence in this case the U (Umklapp)

collisions are negligible and the thermal resistance is offered only by the scattering due to impurities, defects and boundaries. At temperatures below 100K these phenomena becomes more dramatic and hence needs to be carefully examined so as to estimate the thermal conductivity. At lower temperatures the phonon mean free path grows and becomes larger than the structure length, thereby allowing the phonons to drift from hot end to cold end without colliding [58]. This manifestation of ballistic regime is similar to the one observed with photons exchanged between two black plates at discrete temperatures [58].

The simulation case parameters are as follows [58],

- *Hot and cold temperatures:* T_h = 12 K, T_c = 3 K and $T_{ballistic}$ = 10 K,
- *Medium geometry:* stack of 10 cellules (Ly = Lz = $5 \cdot 10^{-7}$ m, Lx = $4 \cdot 10^{-7}$ m),
- *Time step and spectral discretization*: Δt = 5 ps and Nb = 1000 bins.

Figure 4.7 illustrates the transient calculations for Si thin film at low temperature. It can be seen that Figure 4.7 agrees with the ballistic limit when the phonons are allowed to drift for more than 3ns. This is in agreement with velocities prescribed by dispersion curves. Results for transient calculation at low temperatures obtained with our method have been already be predicted by Larcoix et al., in similar cases, using Monte Carlo technique, which gives a greater confidence on the validity of the code [58].

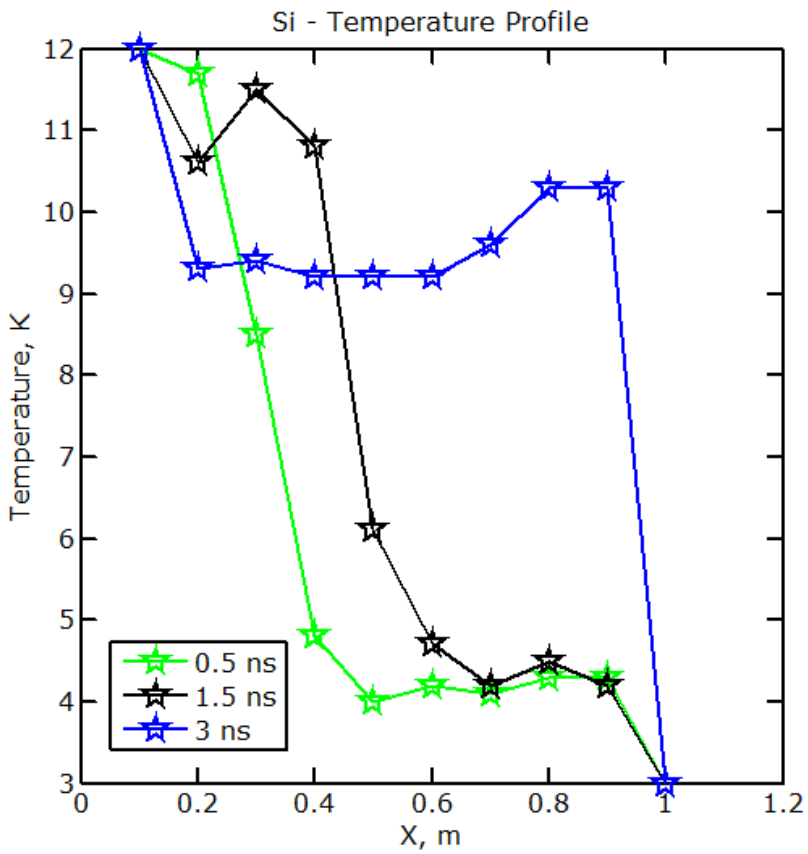

Figure 4.7 Transient calculation for silicon thin film at low temperature

4.2.2 Size Effects

Size effects appear when the characteristic length of the geometric structure is comparable to or smaller than the phonon characteristic wave length [75]. Size effects can be classified into 2 regimes; (1) *Classical regime*, is when phonons are treated as particles, and (2) the *Quantum regime*, when the wave phase information of phonons becomes significant. The characteristic length of the phonon determines the significance of one regime over the other. The most important characteristic lengths of phonon heat conduction are the Mean Free Path (MFP), the wavelength, and the phase coherence length [75]. Since MFP is proportional to the relaxation time (τ), and based

on the previous calculations at the beginning of this chapter it is known that at lower temperatures τ increases such that at a point the phonons from hot end diffuse to the colder end without colliding with other phonons exhibiting ballistic transport. Hence, when the structural size is tweaked so as to match the mean free path at any temperature, ballistic phenomena should be orchestrated [58]. The phenomenon of ballistic heat transport becomes more dramatic especially in reduced dimensional structures where the attenuated size results in large reductions in thermal conductivity compared to the bulk values which is illustrated in Figure 4.9. In case of silicon the deviation of the thermal conductivity from the bulk value reduces steeply when the structural is reduced beyond 300 nm, which is the order of magnitude for the phonon mean free path in silicon at room temperature. At these slacken dimensions the relaxation time for phonon-phonon scattering increases exorbitantly such that the phonon-phonon collisions are almost absent, at these slackened dimensions the scattering processes due to defects, impurities and boundaries offer the only thermal resistance.

So as to validate the aforementioned phenomenon the following simulation case parameters are employed [58],

- *Hot and cold temperatures:* T_h = 500 K, T_c = 250 K,
- *Medium geometry:* stack of 10 cellules,
- *Total length and time step (L, Δt):* (4 nm, $5 \cdot 10^{-3}$ ps), (40 nm, $5 \cdot 10^{-2}$ ps), (400 nm, 5·10−1 ps) and (4μm, 5 ps)

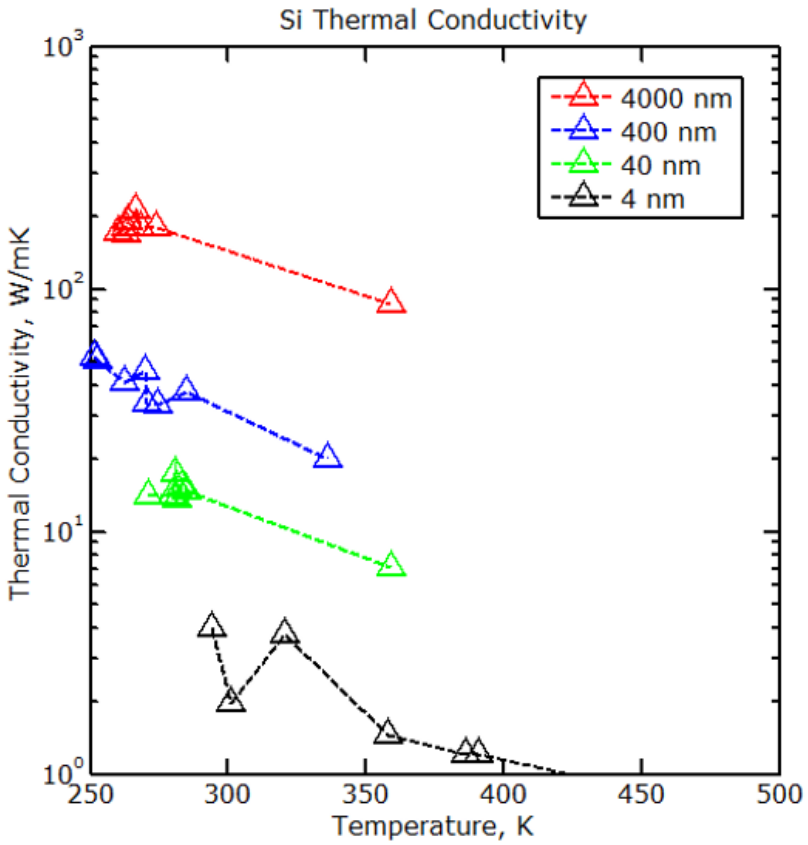

Figure 4.8 plots thermal conductivity for varying dimensions of silicon from bulk to nanowire

It can be observed from Figure 4.8 that the thermal conductivity mitigates as we go from 4um to 4nm reaffirming the ability of the code to capture the size effects.

4.3 Atomistic Coupling

As described in section 4.1 the phonon dispersion curves are computed using KVFF based Molecular Mechanics approach and used as input to the Monte Carlo Phonon Transport kernel to account for some of the an-harmonic effects (finite aperiodic boundary conditions, effects of strain, etc.,).

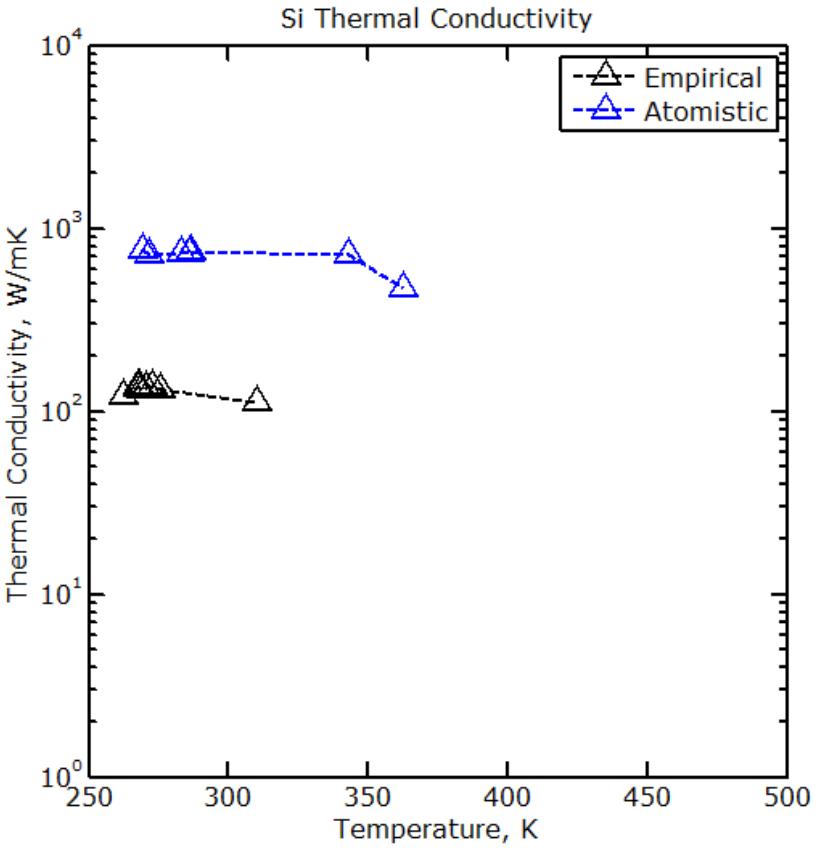

Figure 4.9 compares atomistically computed and empirically computed thermal conductivities for Silicon thin film.

Figure 4.9 shows the comparison between the thermal conductivities plotted using empirically fitted dispersion curve and atomistically computed dispersion curve. It is inferential from Figure 4.9 that the atomistically computed thermal conductivity is nearly order of magnitude higher than the empirically computed thermal conductivity (κ).

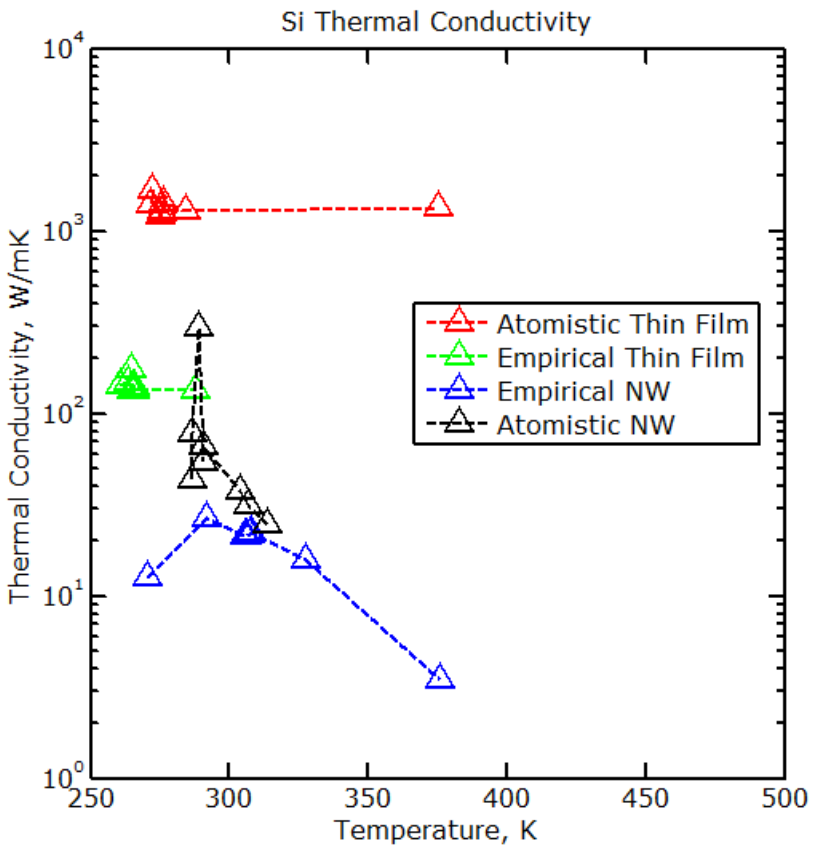

(b)

Figure 4.10 compares atomistically computed and empirically computed thermal conductivities for Silicon thin film and nanowire

Figure 4.10 compares the thermal conductivities between the atomistically and empirically computed curves for silicon thin film and silicon nanowire with dimensions L = 40 nm (L = Lx * Ncells = 4nm * 10); Ly = 5 nm and; Lz = 5 nm. Figure 4.10 interprets the effect of atomistic coupling for thin film and nanowire. In both cases it can be seen that the atomistically computed thermal conductivity (κ) is higher than its empirical counterpart.

The deviation in the thermal conductivities between the 2 simulation approaches is so huge which necessitates the need for further detailed investigation. The thermal conductivity (κ) is characterized by the following equation,

$$\kappa = \frac{1}{3}\sum_{polz}\int_0^{\infty} \hbar\omega \,.\lambda(\omega,T)\,.\frac{df(\omega,T)}{dT}\,.g(\omega).\upsilon.d\omega \tag{4.1}$$

Where,

$$\lambda(\omega,T) = \upsilon_g\,.\tau \tag{4.2}$$

Where,

$f(\omega,T)\,.g(\omega)$ - # of Phonons

υ_g – Group Velocity, and

τ – Relaxation Time

From Equation 4.1 and 4.2 it is very obvious that κ is primarily influenced by 3 major entities namely, group velocity ($v_{g)}$, relaxation time (τ) and Number of phonons in the system. Figure 4.11 shows the group velocity profile for both longitudinal (LA) and transverse (TA) acoustic modes pertaining to both empirical and atomistic simulations. From Figure 4.1 it is clear that the TA velocity for the atomistic simulation is more or less constant (~ 4000 m/s) over the entire TA frequency range unlike its empirical counterpart, for which the velocity decreases as a function of TA frequency. Also observed is that the atomistic LA group velocity at lower frequencies (< $5\,.\,10^{13}$) has a lower velocity and atomistic LA group velocity is higher at frequencies > $5\,.\,10^{13}$ when compared empirical results.

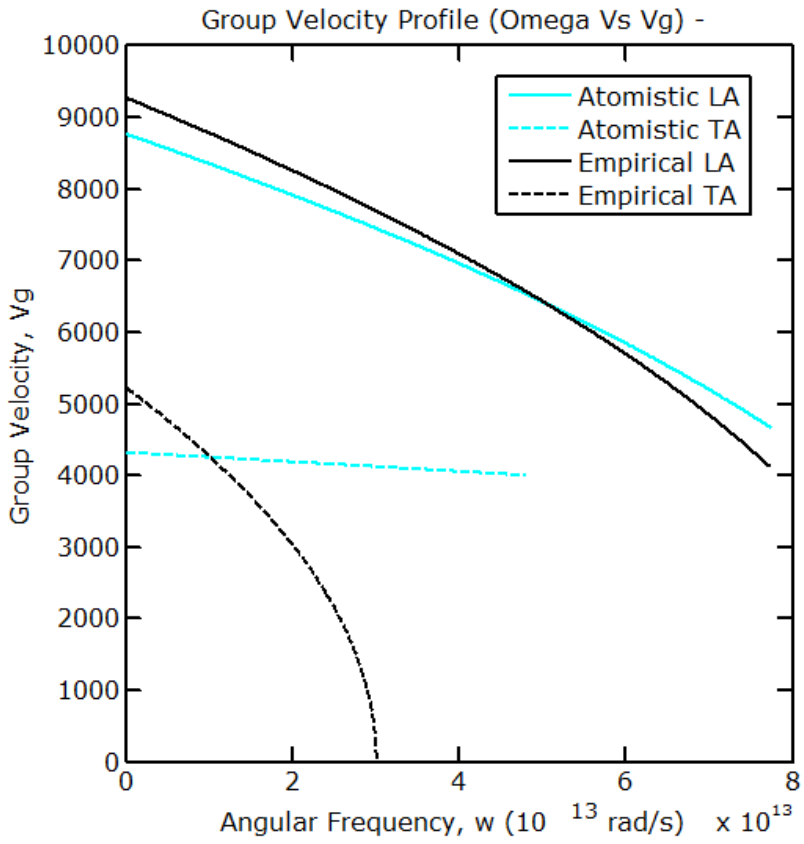

Figure 4.11 Group Velocity profiles comparing atomistic results with empirical results for both LA and TA modes

Secondly, relaxation time (τ) for atomistic simulation is marginally higher than the empirical results. From Figure 4.12 (a) it can be observed that the τ_{LA} increases by $1 . 10^{-7}$ and τ_{TA} increases by $1 . 10^{-10}$. though this is marginal, it affects the Cumulative Probability Density Function (CPDF) curve making the atomistic CPDF less probable to phonon-phonon scattering which is evident from Figure 4.12 (b).

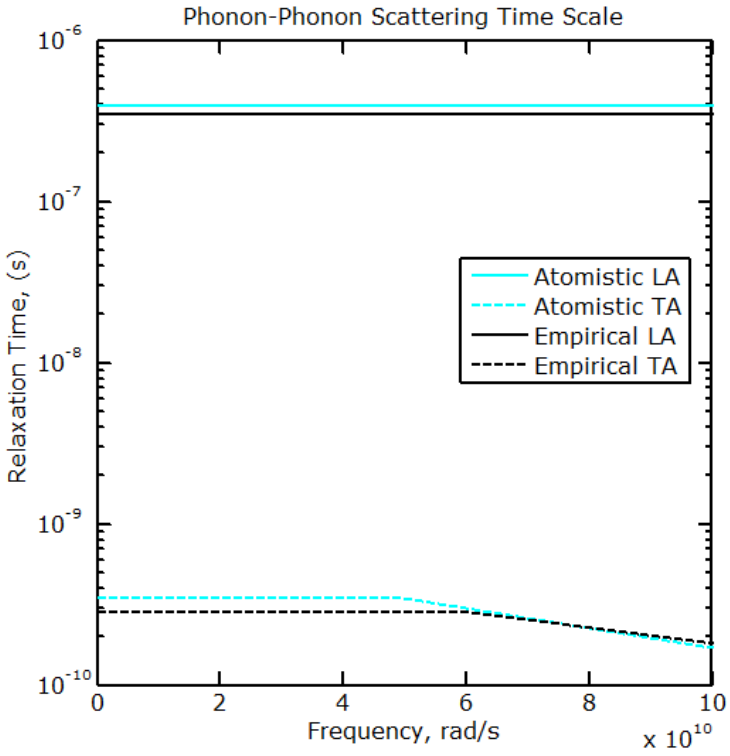
Phonon-Phonon Scattering Time Scale
Relaxation Time, (s)
Frequency, rad/s
x 10^10
Atomistic LA
Atomistic TA
Empirical LA
Empirical TA

(a)

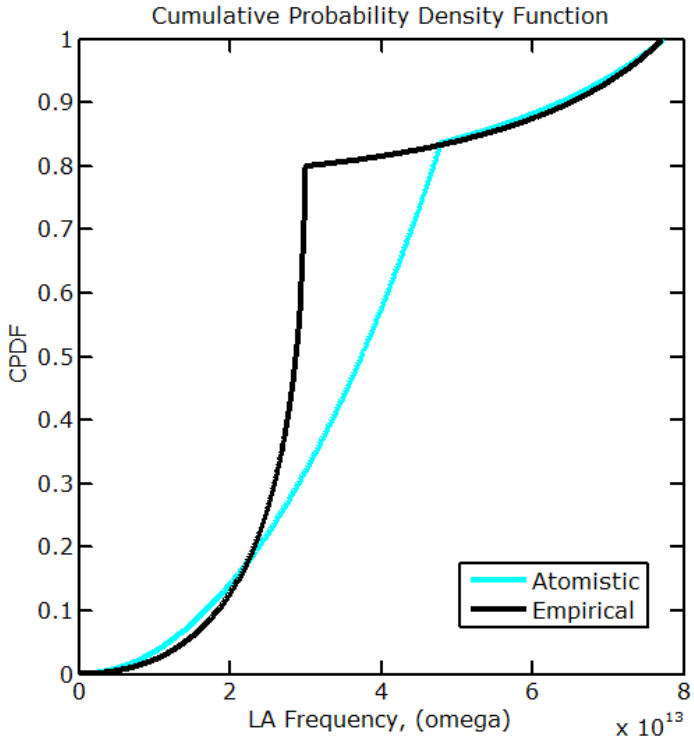
Cumulative Probability Density Function
CPDF
LA Frequency, (omega)
x 10^13
Atomistic
Empirical

(b)

Figure 4.12 (a) shows the zoomed in view of phonon-phonon relaxation time for both atomistic and empirical simulations; (b) computes the scattering probability (CPDF) for both atomistic and empirical simulations

Finally the number of phonons in the medium as a function of frequency is plotted in Figure 4.13 so as to get an insight on total number of phonons in the system. This quantity is very important since increase in number of phonons increases phonon-phonon scattering rates thereby resulting in increasing the MFP and hence the thermal conductivity (κ). From Figure 4.13 it can be seen that the number of phonons due to atomistic simulation at both hot and cold cells are ~ 10^4 orders of magnitude low when compared to empirical counterpart, thereby resulting in increased thermal conductivity as per Equation 4.

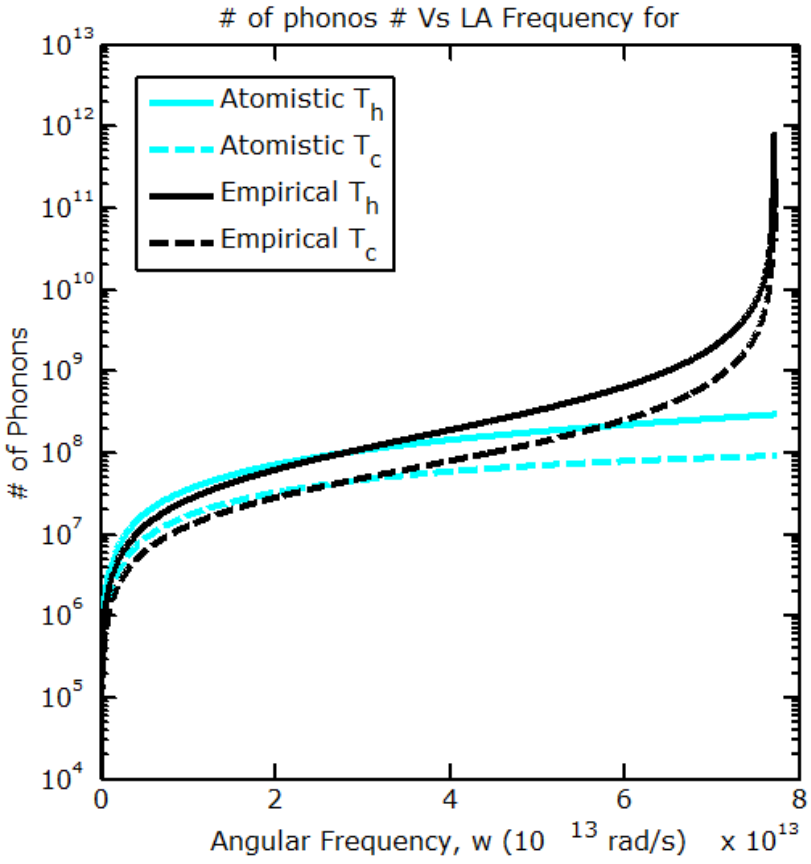

Figure 4.13 computes the total number of phonons initialized at the hot and cold cellules for both atomistic and empirical computations

From the Figures 4.11, 4.12 & 4.13 it is inferential that the group velocity and the number of phonons in the medium are the most significant contributors for the Δ imposed by the atomistic calculation on the thermal conductivity. Hence it is imperative to understand the underlying phenomenon to governing those entities. Group velocity is obtained from the slope of the dispersion relation and number of phonons is the product of Density of States (DoS) and Bose-Einstein distribution function, of which DoS is again derived from dispersion relation.

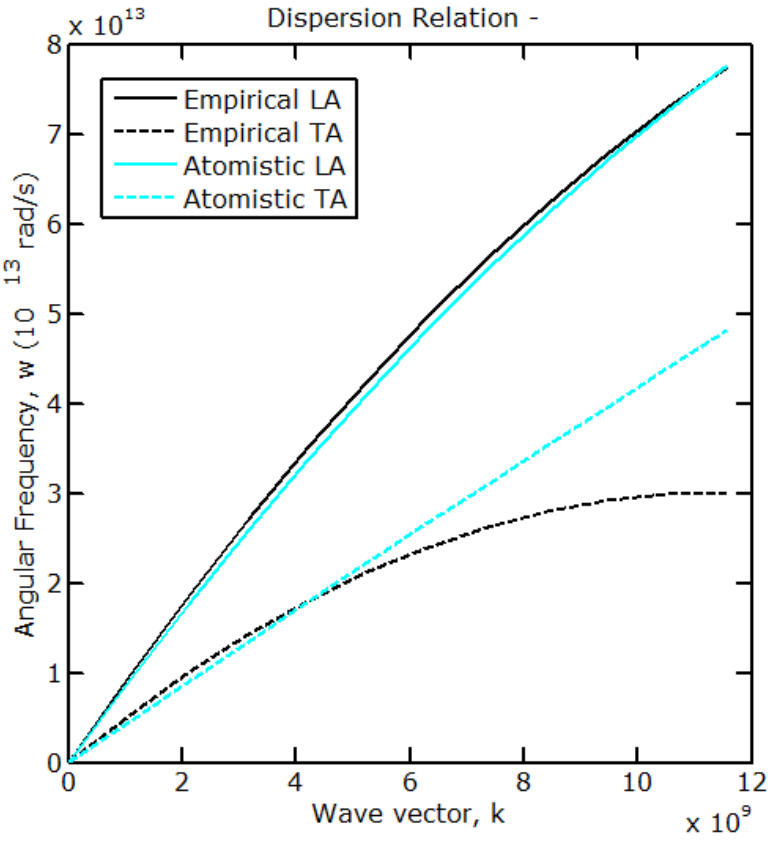

Figure 4.14 Empirical and Atomistic dispersion relations for both LA and TA branches

Since the group velocity and number of phonons are bi-products of dispersion relation it is vital to investigate the dispersion relation with utmost care. Figure 4.14

elucidates the differences between the atomistically computed dispersion and empirically computed dispersion. It can be observed from Figure 4.14 that the atomistically computed transverse acoustic (TA) branch falls in line with the empirically fitted TA near the Brillouin Zone center and fails to flatten out as it moves towards the zone edge thereby creating a $\Delta \sim 7$ % between the empirically and atomistically computed curves. Hence it is evident that the KVFF model does not completely capture the TA mode.

Abhijeet Paul,Klimeck et al [74]., 2010 have modified the existing KVFF method for the same reason. In their paper [74] they have claimed that KVFF model overestimates the TA frequency near the zone edge especially near X and L valleys, which is quite similar to our claim. The following Figure 4.15, [74] has been published in their paper which exemplifies the need to replace KVFF model with MVFF model and all the underlying issues. The $\Delta \sim 7\%$ and the lack of flatness in TA curve mainly arises from missing co-planar interactions. Also the paper claims that the KVFF model describes the LA, LO and TO frequencies reasonably well. This TA issue is mainly pertaining to Zinc-Blende crystal structure only. Hence computing the dispersion from MVFF approach would be a task for future modifications. It can be seen from Figure 4.15 that KVFF model that for Bulk Silicon KVFF model overshoots the experimental values. Also observed from the figure is the corrected dispersion results computed by employing MVFF model.

So as to decouple the increase in thermal conductivity due to the inability of the KVFF model to capture the flatness in TA branch and actual atomistic dispersion a hybrid approach has been adopted.

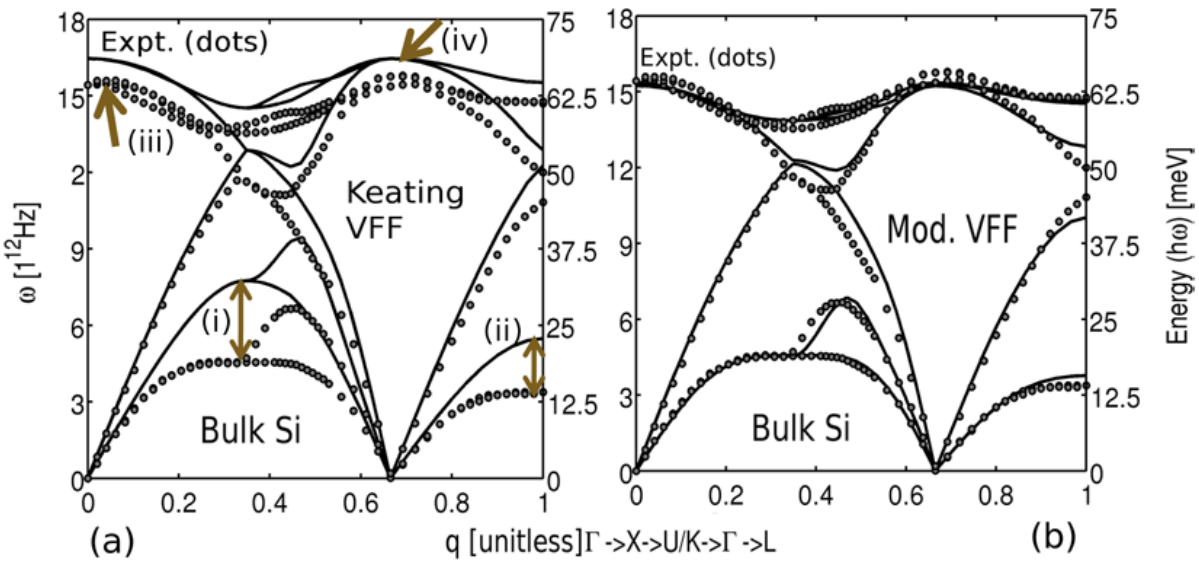

Figure 4.15 [74] illustrates the phonon bandstructure for Bulk Silicon

Since it has been exemplified that the KVFF model captures LA, LO and TO branches perfectly, the hybrid approach utilizes the LA frequency from the KVFF based molecular mechanics dispersion and TA frequency from the empirically fitted curves so as to iron out the issues caused by KVFF TA model. Figure 4.16 plots the hybrid dispersion model that is being adopted. In Figure 4.16 the Hybrid TA branch is not seen because it is overlapped by its empirical analogue. Since the TA branch is compensated for, the 2 major entities (group velocity, v_g and # of phonons) governing the thermal conductivity are again computed with this hybrid model.

Figure 4.17 illustrates the group velocity (v_g) profile for the hybrid model. It can be seen that the LA v_g still decreases for $\omega < 5 \,.\, 10^{13}$ and increases for higher frequencies when compared to that of the empirically computed LA v_g. Figure 4.18 plots the number of phonons in the medium at hot and cold cellules using hybrid approach and compares with the empirical results.

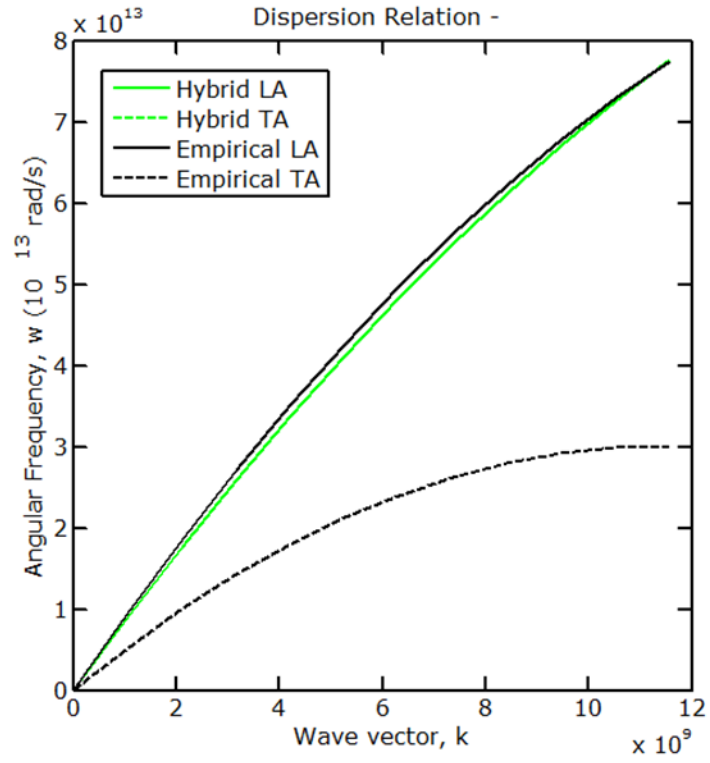

Figure 4.16 Dispersion relation for Hybrid Model (Atomistic LA and Empirical TA)

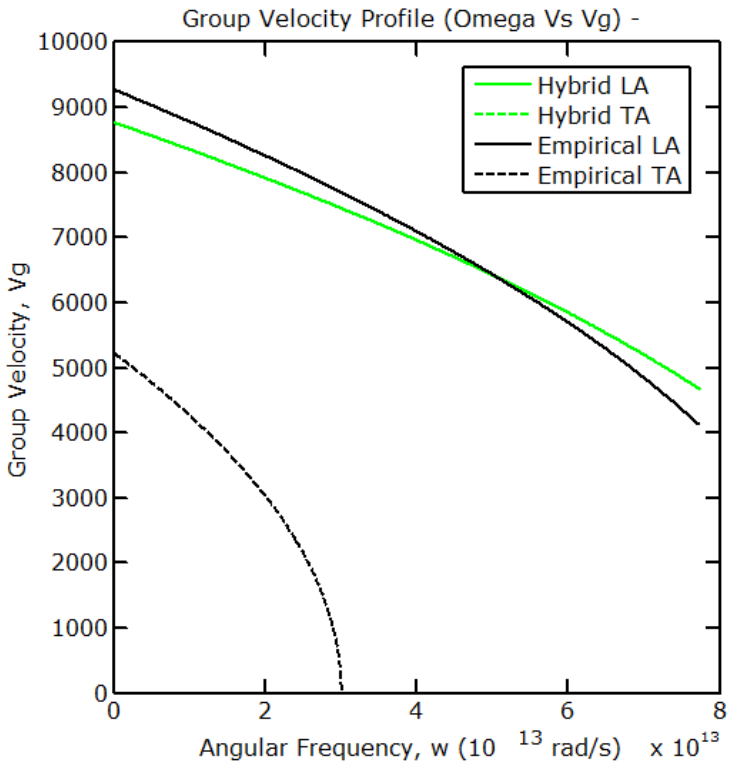

Figure 4.17 Group velocity profile for Hybrid Model (Atomistic LA and Empirical TA)

On comparing Figure 4.13 and 4.18 it can be observed that the reduction in the number of phonons at both hot and cold temperatures recovers to reasonably match the empirical numbers. Also observable from the figure is that hybrid model recovers to an extent that it edges out the empirically computed phonon numbers.

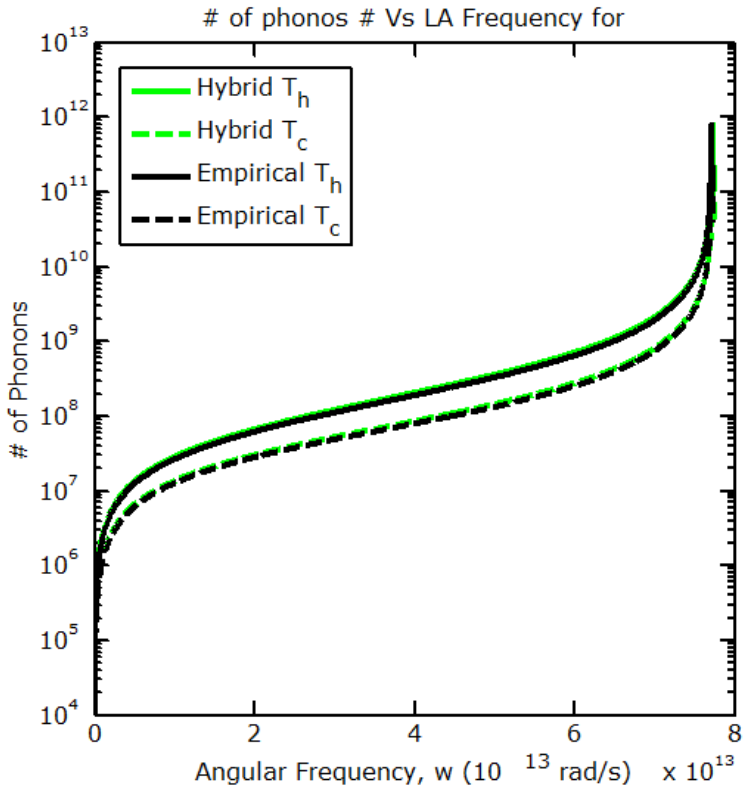

Figure 4.18 computes the total number of phonons initialized at the hot and cold cellules for both hybrid and empirical computations

This recovery of number of phonons and correction to the TA group velocity helped in mitigating the thermal conductivity. Figure 4.19 shows the thermal conductivity profiles plotted using hybrid and empirical approaches. It can be inferred from the figure that despite the reduction in thermal conductivity due to correction to the TA branch

there exists a net increase of ~28 W/m-K in thermal conductivity computed using hybrid approach. This increase is mainly attributed to the atomistic correction adopted for the LA branch.

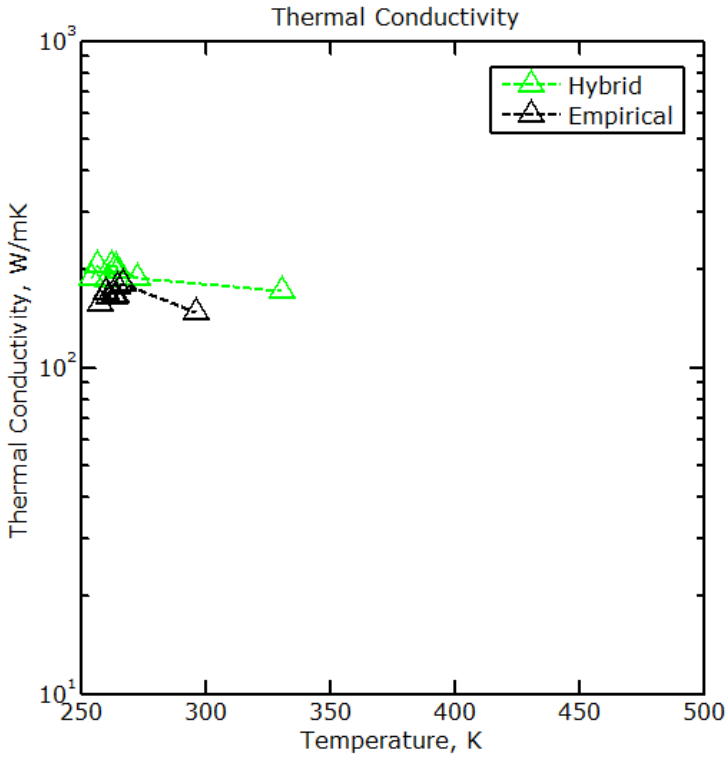

Figure 4.19 illustrates the thermal conductivity computed using hybrid and empirical approaches.

From Figure 4.18 it can be observed that still the thermal conductivity computed using hybrid model is greater than its empirical analogue by ~17% thereby emphasizing the need to include the an-harmonicity in calculation of the material thermal conductivity.

4.4 Materials of Interest

Materials of interest are selected based on the applications that are to be simulated in this work. In this work it is planned to study 2 device applications each

having its own significance. First, a thermoelectric refrigerator to employ the use of atomistically computed thermal conductivity to accurately model the Thermoelectric Cooler (TEC). Second application is AlN-GaN disk-in-wire LED to understand the effects of heating over Internal Quantum Efficiency of the LED. In order to realize these devices it is vital to understand the thermal conductivity of 2 major materials namely Bi_2Te_3 and GaN for the purpose of TEC and LED respectively.

4.4.1 Bismuth Telluride (Bi_2Te_3)

Bi_2Te_3 is an excellent thermoelectric device since it offers very narrow thermal conductivity and hence can be used for Thermoelectric Coolers. Figure 4.20 illustrates the thermal conductivity of bulk Bi_2Te_3 obtained using MCPT, the inset shows the thermal conductivity of Bi_2Te_3 measured by *Mavrokefalos et al* in [76]. It can be seen that the thermal conductivity computed using MCPT falls in line with the experimental observation.

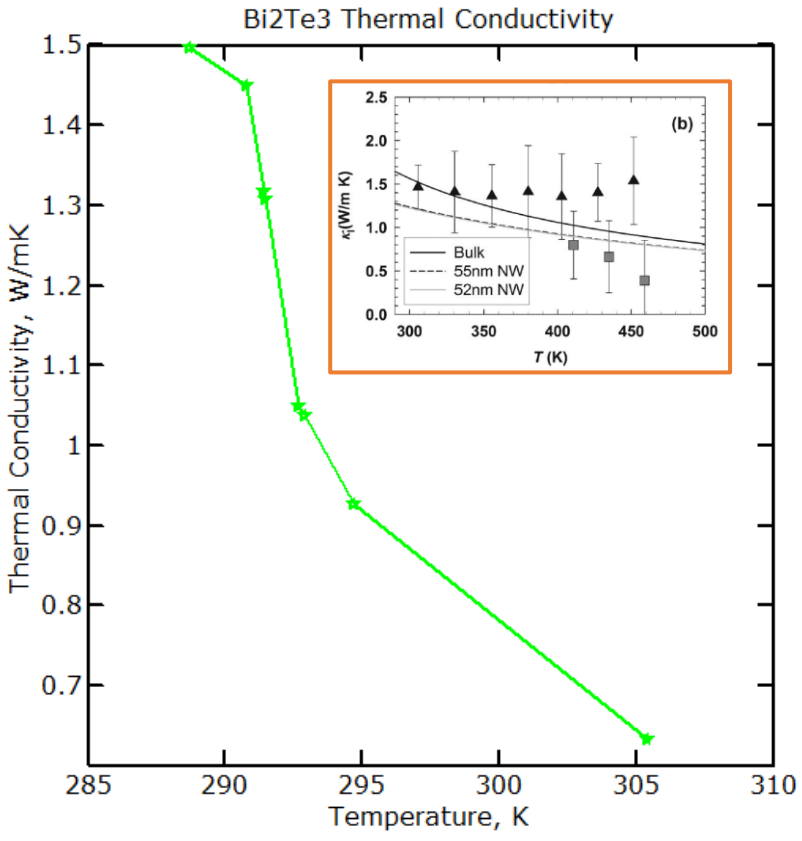

Figure 4.20 Plots Bi_2Te_3 thermal conductivity for bulk; the inset shows Bi_2Te_3 thermal conductivities experimentally by *Mavrokefalos et al* [76]

4.4.2 Gallium Nitride (GaN)

Recently, light emitters using nanostructured GaN/AlN active regions have attracted much attention due to several potential advantages, such as, wide range of emission frequencies (ultraviolet to red), high quantum efficiency, low noise, and high color gamut, higher temperature stability of the threshold current and the luminescence, and low sensitivity to ionizing radiation [77]. The impacted markets include energy, digital information, healthcare and biotechnology, instrumentation, communications, and security.

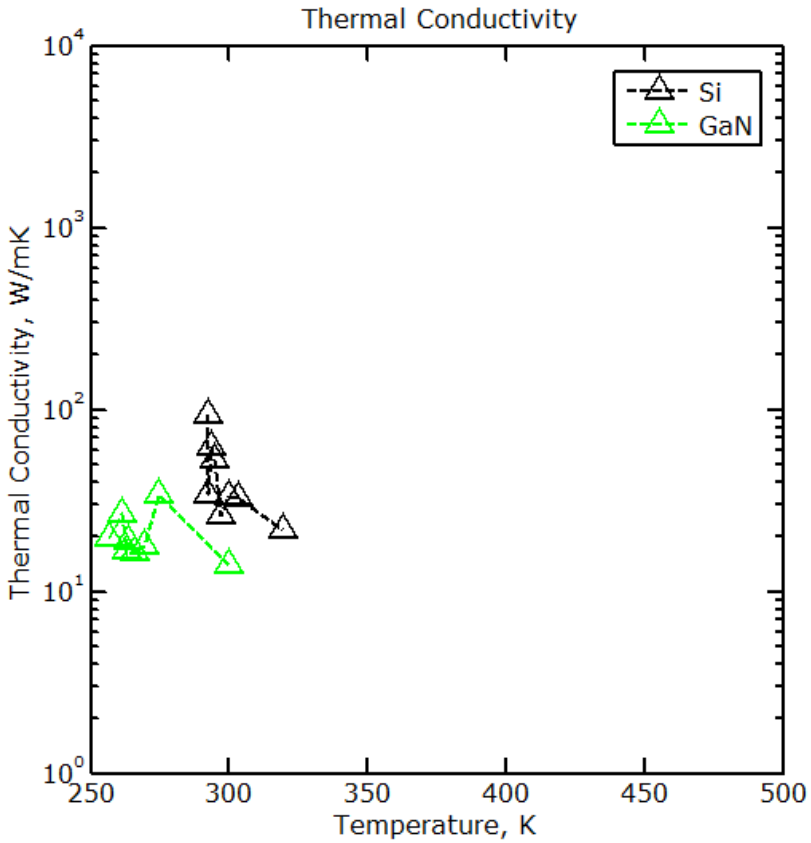

Figure 4.21 computes thermal conductivity of Si and GaN

Owing to the excellent optical properties of GaN, they are extensively used in LED applications. In this work the effect of temperature related degradation on the Internal Quantum Efficiency of LED is investigated. For this purpose the Figure 4.21 computes the thermal conductivity of GaN and Silicon.

4.5 Device Integration – Thermoelectric Coolers

The concept of thermoelectric cooling employs the use of Peltier effect to create heat flux between the junctions of two different types of materials. Thermoelectric cooling device comprises of two sides, and when DC current flows through the device, the electrons carries heat from one end to the other, and hence one side gets cooler while the other gets hotter. The "hot" side is attached to a heat sink so that it remains at ambient temperature, while the cool side goes below room temperature thereby effectively creating a refrigeration system. Figure 4.22 illustrates the schematic of the simulated TEC device. In Figure 4.22 I_Q represents the flow of charges carrying the heat.

The amount of heat extracted from the cold side is given by the following equation,

$$Q_c = \pi_n \frac{I}{A} - \kappa \frac{dT_L}{dx} - \frac{I^2 R_n}{2A} \left(\frac{W}{m^2}\right) \tag{4.3}$$

Where the first term represents the heat pumped by peltier effect, the second term heat diffusing down the thermal gradient and the third and final term represents the heat generated by joule heating. This work employs the use of Thermo-Electric Cooler

(TEC) simulator developed by *Afsana et al* [80]. Figure 4.23 compares the cooling efficiency of Silicon modeled with empirical and atomistic thermal conductivities. This figure gives an insight on % of degradation occurring due to atomistic thermal conductivity. Also noticeable in the figure is that after reaching the minima the temperature starts to increase again this occurs due to joule heating at higher currents.

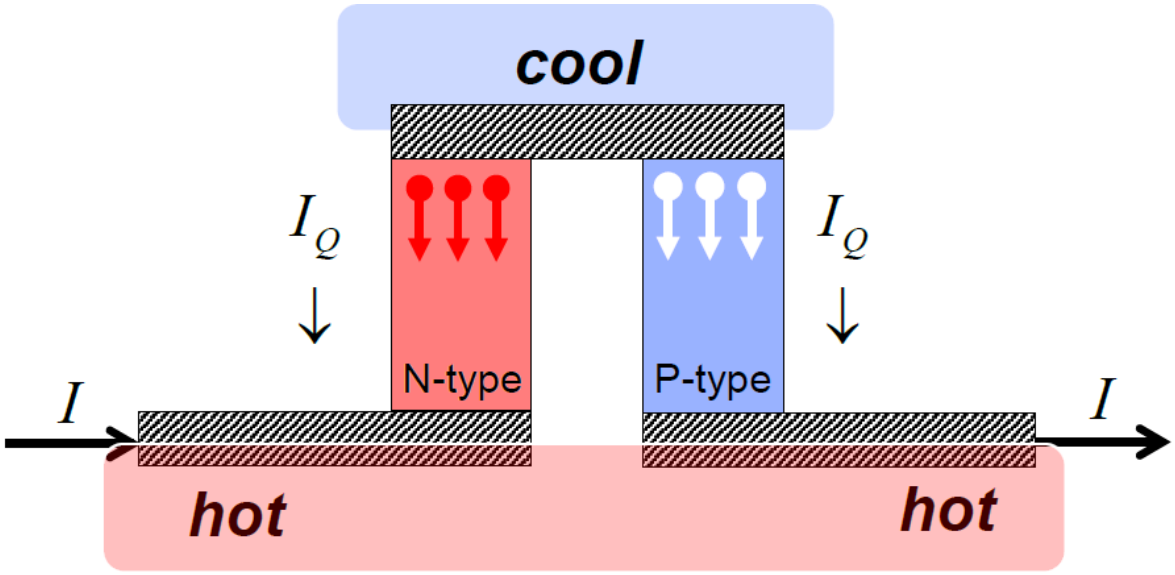

Figure 4.22 represents the schematic of a thermoelectric cooling device [78]

Since Silicon is not a thermoelectric material the cooling efficiency is very poor, but this above experiment was done just to analyze the percentage degradation of cooling efficiency due to thermal conductivity obtained atomistically. Figure 4.24 compares the cooling efficiency of Silicon and Bismuth Telluride. Since Bi2Te3 is an excellent thermoelectric device the temperature drop is significantly more.

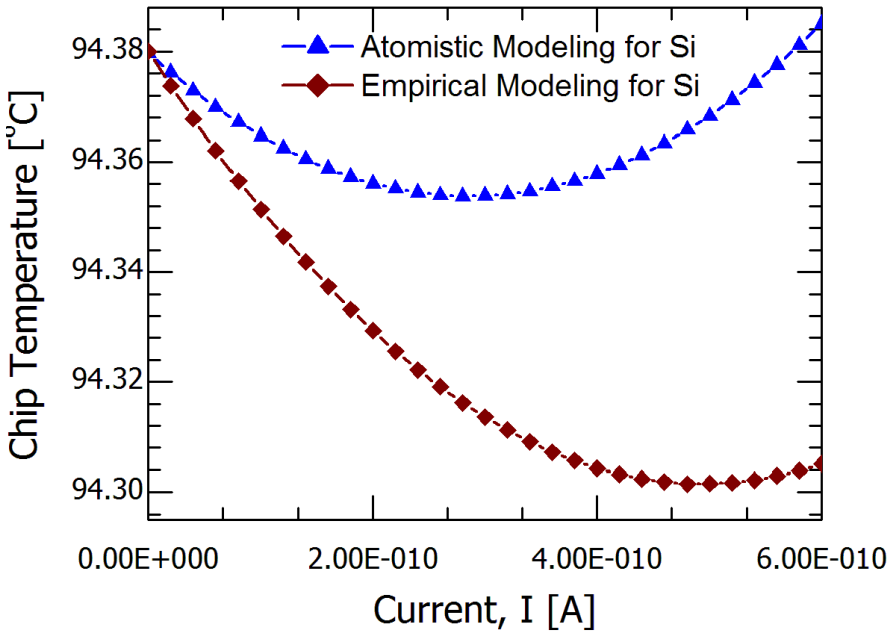

Figure 4.23 Plots the cooling efficiency modeled using atomistic and empirical thermal conductivities

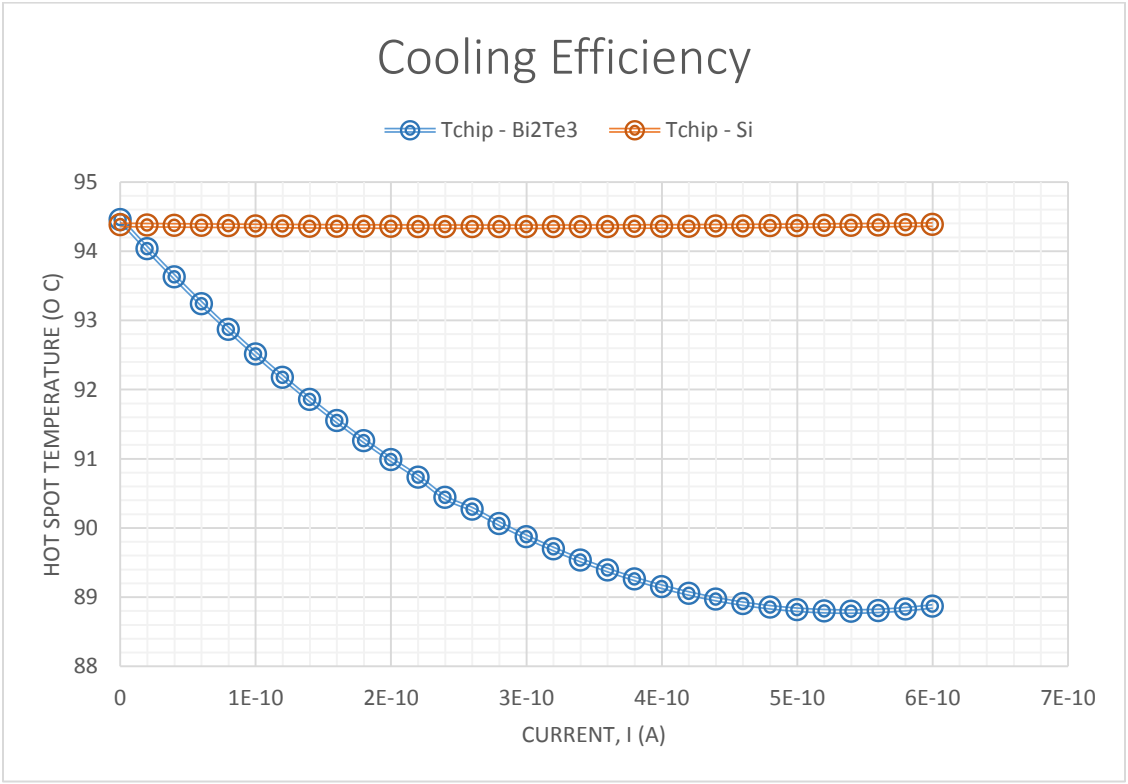

Figure 4.24 illustrates the cooling efficiency for Silicon and Bismuth Telluride

4.6 Device Integration – LED

Synopsys's Sentaurus TCAD [79] tool is employed to simulate the device physics, electrical and optical characteristics of disk-in-wire LEDs. In order to obtain the realistic device structure, process information and electrical information, Synopsys's 3 core TCAD tools are used namely, Sentaurus Structure Editor – 2D and 3D geometric modeling of physical structure, Sentaurus Device – electrical, thermal and optical characterization of silicon-based and compound semiconductor and Tecplot or Inspect – Powerful visualization tool for 2D and 3D structures. Sentaurus Device includes optional models for the comprehensive simulation of Light Emitting Diodes (LEDs) which solves Drift-diffusion or hydrodynamic or thermodynamic transport equations for the carriers, the Schrödinger equation for quantum well gain, optical rate equations, and the Helmholtz equations self-consistently in the quasi-stationary and transient modes [79]. Sentaurus Device considers 3 major aspects for LED simulations, (1) The Helmholtz equation must be solved to determine the optics of the device, (2) Spontaneous and Stimulated rate equation must be included to couple the electronics to the optics, and (3) The carrier-scattering processes at the quantum wells or quantum dots must be treated differently because it is no longer in the drift-diffusion regime. Synopsys prohibits the use of standard time domain electromagnetic methods such as finite difference and finite element methods which are computationally complex. Alternatively, Synopsys uses the raytracing method which approximates the optical intensity inside the device as well as the amount of light that can be extracted from the device thereby

making it computationally less complex. Photon recycling is another important model incorporated by Synopsys to predict the light rays are trapped within the device by total internal reflection. Hence, Sentaurus Device performs the electro-thermal-optical simulation of the disk-in-wire LED.

Figure 4.25 (a) depicts the schematic of the simulated structure and Figure 4.25 (b) exemplifies the dimensions of the disk-in-wire structure.

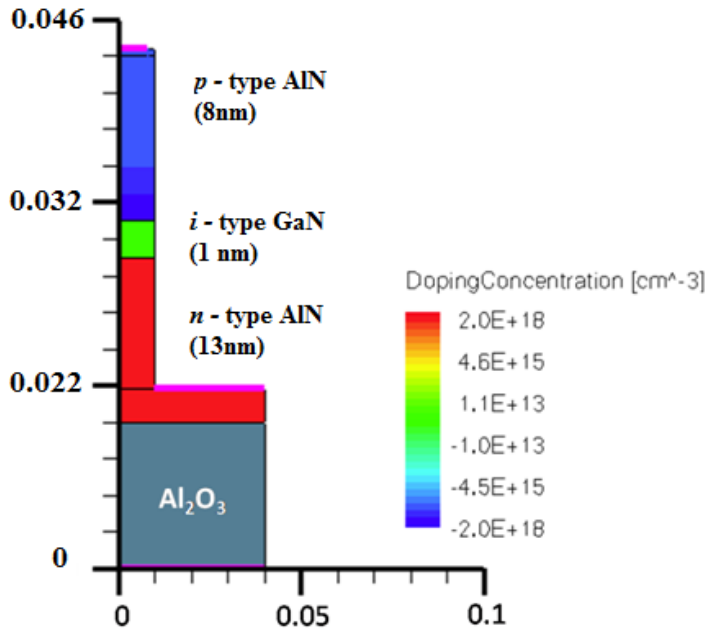

(a)

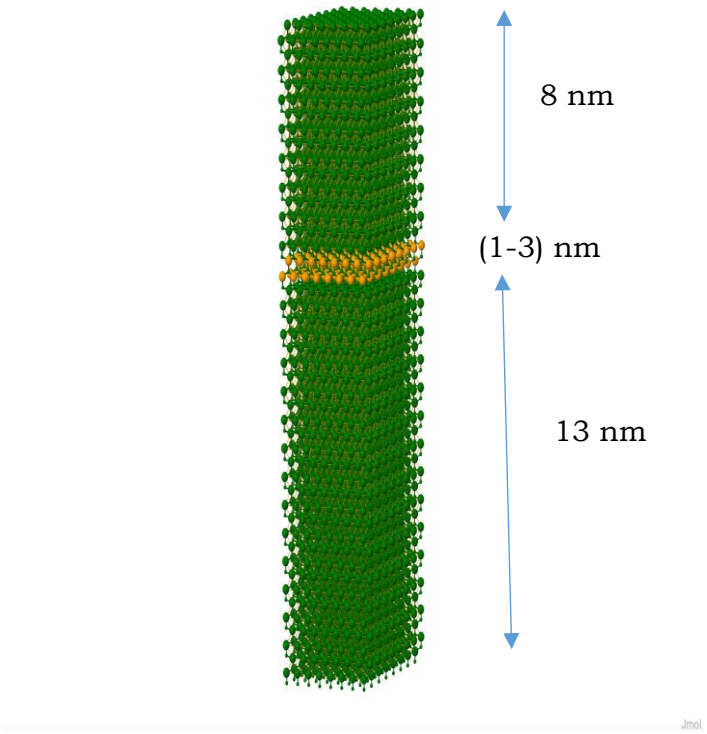

(b)

Figure 4.25 (a) shows the schematic of the simulated LED. (b) Shows the dimensions of the simulated disk-in-wire structure

Figure 4.25(a) shows the simulated disk-in-wire LED with its doping profiles. The core active region of the device comprises of an undoped 1-3 -nm thick GaN disk grown in the [0001] direction. The GaN disk is sandwiched between an n-doped AlN buffer region and a p-doped AlN cap layer both having base length, b~10 nm and height, h~8 nm & 13 nm respectively. The disk-in-a-wire system is grown on a 20-nm thick sapphire substrate. Figure 4.26 illustrates the Internal Quantum Efficiency (IQE) for varying disk thickness.

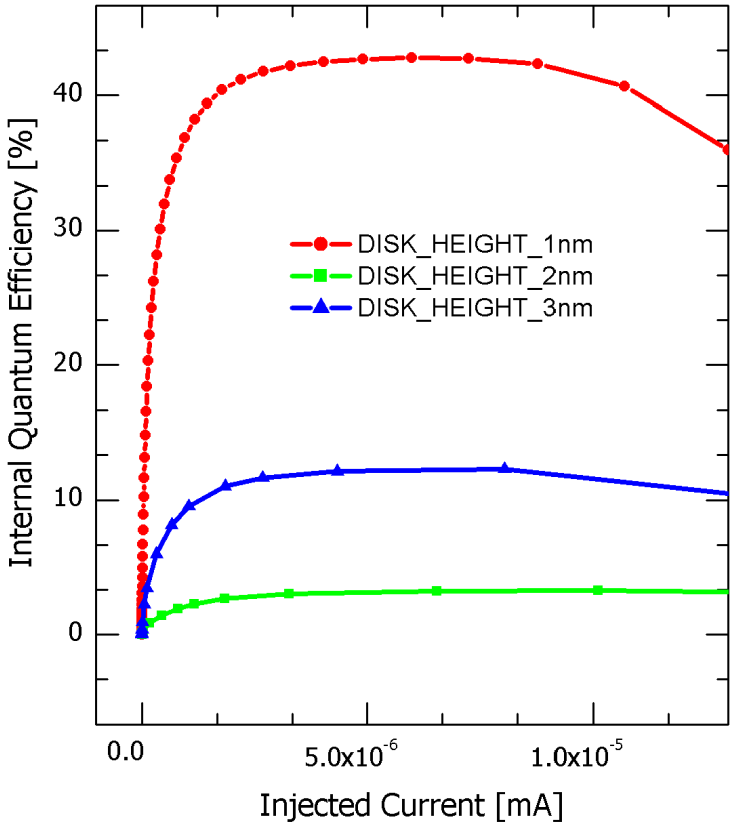

Figure 4.26 illustrates the IQE for varying disk thickness

The thermal conductivity obtained using Monte Carlo Transport kernel is used as an input for Synopsys to solve for spontaneous emission rate and hence the Internal Quantum Efficiency, so as to determine the terminal electrical and optical characteristics of LED. Figure 4.27 shows the atomistically corrected IQE for a disk-in-wire LED with disk thickness ~2 nm. It can be observed from the figure that the atomistically corrected curve shows increased IQE compared to its counterpart.

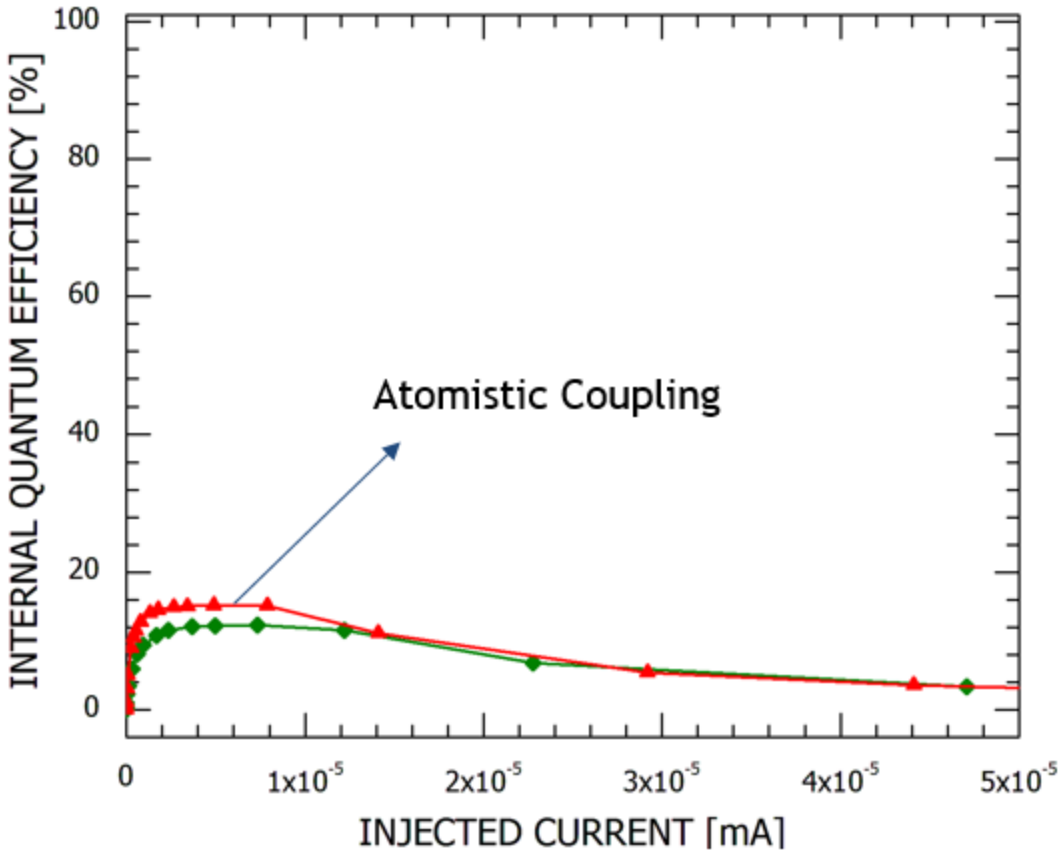

Figure 4.27 illustrates the IQE for a disk-in-wire LED with disk thickness ~2nm for both with and without atomistic correction.

CHAPTER 5

CONCLUSION

Accurate modeling of non-equilibrium heat transport calls for proper description of dispersion relation, such that it accounts for the anharmonic effects like thermal expansion, interaction of lattice waves, effect of strain on spring stiffness, and accurate phonon-phonon interactions. A 17% increase in thermal conductivity demonstrated for a Silicon nanowire, solely due to atomistic corrections in LA branch in this work stands as a testimony to the aforementioned statement. The device level implications for both thermal management (Light Emitting Diode) and thermoelectric (Thermo-Electric Cooler) applications were observed to be significantly influenced by atomistic correction and anharmonic effects. The simulation results in case of thermal management applications for a GaN based Light Emitting Diode yielded ~3% correction (increase) in optical efficiency in optical efficiency and a Si based Thermo-Electric Cooler employed in case of thermoelectric application resulted in ~0.08 C degradation in Cooling temperature on accounting for atomistic corrections.

The need for proper description of atoms, simulating a realistically sized device, different transport time and length scales of phonon and electron transport renders accounting for anharmonic effects a computationally mammoth task. Hence, a computationally less complex multi-scale quasi-anharmonic framework for phonon transport, which is capable of coarsely addressing anharmonic effects with the ability to describe non-equilibrium heat transport at different time and length scales is developed.

This work employs a Monte Carlo based statistical approach to solve Boltzmann Transport Equation (BTE), so as to predict the thermal conductivity of specified material

geometry. An atomistically computed phonon dispersion relation based on Keating-VFF model is used to determine the properties of phonons. In order to circumvent the inability of KVFF approach to qualitatively account for 7% mismatch in TA branch of Si at the Brillion zone edge a hybrid approach was adopted in this work, which eliminates the ambiguity in trusting KVFF model.

The coupling between Molecular Mechanics module and Monte Carlo Transport kernel enables more accurate prediction of thermal conductivity, since it accounts for the anharmonic contributions. A non-deterministic approach adopted in this work provides satisfactory results in what concerns phonons transport in both ballistic and diffusive regimes to understand the heat transport at varied length scales.

REFERENCES

[1] K. Fushinobu, K. Hijikata, and A. Majumdar, “Heat Generation and Transport in Submicron Semiconductor Devices,” J. Heat Transfer, vol. 117, no. 1, pp. 25–31, Feb. 1995.

[2] http://spectrum.ieee.org/computing/hardware/moores-law-meets-its-match

[3] http://www.more-than-moore.com/more-than-moore/what-is-more-than-moore/

[4] Karthik Sankaranarayanan, “Thermal Modeling and Management of Microprocessors”, PhD Dissertation University of Virginia.

[5] M. Arik, C. A. Becker, S. E. Weaver, and J. Petroski, “Thermal management of LEDs: package to system,” 2004, vol. 5187, pp. 64–75.

[6] http://www.extremetech.com/computing/116561-the-death-of-cpu-scaling-from-one-core-to-many-and-why-were-still-stuck

[7] http://www.legitreviews.com/intel-core-i7-990x-extreme-edition-hex-core-processor-performance-review_1604/12

[8] E. Pop, S. Sinha, and K. E. Goodson, “Heat Generation and Transport in Nanometer-Scale Transistors,” Proceedings of the IEEE, vol. 94, no. 8, pp. 1587–1601, Aug. 2006.

[9] J. Lai and A. Majumdar, “Concurrent thermal and electrical modeling of sub-micrometer silicon devices,” Journal of Applied Physics, vol. 79, no. 9, pp. 7353–7361, May 1996.

[10] SIA. International Technology Roadmap for Semiconductors, 2006, http://www.itrs.net/links/2006Update/2006UpdateFinal.htm

[11] S.-C. Lin and K. Banerjee, “Cool Chips: Opportunities and Implications for Power and Thermal Management,” IEEE Transactions on Electron Devices, vol. 55, no. 1, pp. 245–255, Jan. 2008.

[12] R. H. Dennard, F. H. Gaensslen, V. L. Rideout, E. Bassous, and A. R. LeBlanc, “Design of ion-implanted MOSFET’s with very small physical dimensions,” IEEE Journal of Solid-State Circuits, vol. 9, no. 5, pp. 256–268, Oct. 1974.

[13] D. J. Frank, “Power-constrained CMOS scaling limits,” IBM Journal of Research and Development, vol. 46, no. 2.3, pp. 235–244, Mar. 2002.

[14] S. Borkar, “Design challenges of technology scaling,” IEEE Micro, vol. 19, no. 4, pp. 23–29, Jul. 1999.

[15] SIA. International Technology Roadmap for Semiconductors, 2012, http://www.itrs.net/Links/2012ITRS/2012Chapters/2012Overview.pdf

[16] S. Borkar, T. Karnik, S. Narendra, J. Tschanz, A. Keshavarzi, and V. De, “Parameter variations and impact on circuits and microarchitecture,” in Design Automation Conference, 2003. Proceedings, 2003, pp. 338–342.

[17] Y. Taur and T. H. Ning Fundamentals of Modern VLSI Devices 1998, Cambridge Univ. Press

[18] K. Banerjee, S.-C. Lin, A. Keshavarzi, S. Narendra, and V. De, “A self-consistent junction temperature estimation methodology for nanometer scale ICs with implications for performance and thermal management,” in Electron Devices

Meeting, 2003. IEDM ’03 Technical Digest. IEEE International, 2003, pp. 36.7.1–36.7.4.

[19] The Market for Thermal Management Technologies, BCC Research, http://www.bccresearch.com/market-research/semiconductor-manufacturing/thermal-management-technology-smc024f.html

[20] http://www.businesswire.com/news/home/20111019006068/en/Companiesandmarkets.com-Miniaturization-Driving-Force-Thermal-Management-Technologies#.UyKVy_ldVH1

[21] A. I. Boukai, Y. Bunimovich, J. Tahir-Kheli, J.-K. Yu, W. A. Goddard Iii, and J. R. Heath, “Silicon nanowires as efficient thermoelectric materials,” Nature, vol. 451, no. 7175, pp. 168–171, Jan. 2008.

[22] M. Zebarjadi, K. Esfarjani, M. S. Dresselhaus, Z. F. Ren, and G. Chen, “Perspectives on thermoelectrics: from fundamentals to device applications,” Energy & Environmental Science, vol. 5, no. 1, p. 5147, 2012.

[23] A. J. Minnich, M. S. Dresselhaus, Z. F. Ren, and G. Chen, “Bulk nanostructured thermoelectric materials: current research and future prospects,” Energy & Environmental Science, vol. 2, no. 5, p. 466, 2009.

[24] G. Chen, M. S. Dresselhaus, G. Dresselhaus, J.-P. Fleurial, and T. Caillat, “Recent developments in thermoelectric materials,” International Materials Reviews, vol. 48, no. 1, pp. 45–66, Feb. 2003.

[25] R. Venkatasubramanian, E. Siivola, T. Colpitts, and B. O'Quinn, "Thin-film thermoelectric devices with high room-temperature figures of merit," Nature, vol. 413, no. 6856, pp. 597–602, Oct. 2001.

[26] A. Paul, S. Salamat, C. Jeong, G. Klimeck, and M. S. Lundstrom, "An Efficient Algorithm to Calculate Intrinsic Thermoelectric Parameters Based on Landauer Approach," Birck and NCN Publications, 2011.

[27] A. Majumdar, "THERMOELECTRIC DEVICES Helping chips to keep their cool," Nature Nanotechnology, vol. 4, pp. 214–215, 2009.

[28] K. Fukutani and A. Shakouri, "Design of bulk thermoelectric modules for integrated circuit thermal management," IEEE Transactions on Components and Packaging Technologies, vol. 29, pp. 750–757, 2006.

[29] T. C. Harman, P. J. Taylor, M. P. Walsh, and B. E. LaForge, "Quantum Dot Superlattice Thermoelectric Materials and Devices," Science, vol. 297, no. 5590, pp. 2229–2232, Sep. 2002.

[30] F. J. DiSalvo, "Thermoelectric Cooling and Power Generation," Science, vol. 285, no. 5428, pp. 703–706, Jul. 1999.

[31] IDTechEX, http://www.idtechex.com/research/articles/thermoelectric-generators-a-750-million-market-by-2022-00004631.asp

[32] J. Callaway. Model for lattice thermal conductivity at low temperatures. Phys. Rev., 113(4):1046 - 1051, Feb. 1959.

[33] M. G. Holland. Analysis of lattice thermal conductivity. Phys. Rev., 132(6):2461 - 2471, Dec 1963.

[34] M. G. Holland. Phonon scattering in semiconductors from thermal conductivity studies. Phys. Rev., 134(2A):A471 - A480, Apr 1964.

[35] A. Majumdar. Microscale heat conduction in dielectric thin films. Journal of Heat Transfer, 115(7):7{16, 1993.

[36] I. Errea, M. Calandra, and F. Mauri, “Anharmonic free energies and phonon dispersions from the stochastic self-consistent harmonic approximation: application to platinum and palladium hydrides,” arXiv:1311.3083 [cond-mat], Nov. 2013.

[37] http://www2.warwick.ac.uk/fac/sci/physics/current/postgraduate/regs/mpags/ex5/phonons/

[38] http://www.chembio.uoguelph.ca/educmat/chm729/phonons/intro.htm

[39] http://en.wikipedia.org/wiki/Phonon#Interpretation_of_phonons_using_second_quantization_techniques

[40] Timothy S. Fischer, “Basic Thermal Properties,” in Thermal Energy at the Nanoscale, WORLD SCIENTIFIC, 2013, pp. 61–86.

[41] Timothy S. Fischer , “Lattice Structure, Phonons, and Electrons,” in Thermal Energy at the Nanoscale, WORLD SCIENTIFIC, 2013, pp. 1–35.

[42] Tubino, R., L. Piseri, G. Zerbi, J. Chem. Phys. 56 , 1972, 1022-1039.

[43] http://www2.physics.ox.ac.uk/sites/default/files/2011-10-04/crystalstructure_handout9_pdf_17283.pdf

[44] http://www.physics.iisc.ernet.in/~aveek_bid/PH208/Lecture%208%20phonons-thermal%20properties.pdf

[45] Balandin, Alexander A., Evghenii P. Pokatilov, and D. L. Nika. "Phonon engineering in hetero-and nanostructures." Journal of Nanoelectronics and Optoelectronics 2.2 (2007): 140-170.

[46] Shaikh Ahmed, Krishnakumari Yalavarthi, Vamsi Gaddipati, Abdussamad Muntahi, Sasi Sundaresan, Shareef Mohammed, Sharnali Islam, Ramya Hindupur, Dylan John, And Joshua Ogden, “Quantum Atomistic Simulations of Nanoelectronic Devices using QuADS,” Nano-Electronic Devices: Semiclassical and Quantum Transport Modeling, Springer, Book Edited by D. Vasileska and S. M. Goodnick, pp. 405, 2011.

[47] K. Yalavarthi, S. Sundaresan, and S. Ahmed, “Multiscale modeling of wurtzite InN/GaN quantum Dot LEDs,” in 2011 11th IEEE Conference on Nanotechnology (IEEE-NANO), 2011, pp. 881 –886.

[48] F. Grosse and J. Neugebauer, “Limits and accuracy of valence force field models for InxGa1-xN alloys,” Phys. Rev. B, vol. 63, no. 8, p. 085207, Feb. 2001.

[49] http://en.wikipedia.org/wiki/Molecular_mechanics

[50] www.tau.ac.il/~ephraim/MM+MD.doc

[51] http://vergil.chemistry.gatech.edu/courses/chem6485/pdf/molmech-lecture.pdf

[52] David Lai Gwai Cheung, “Structures and Properties of Liquid Crystals and Related Molecules from Computer Simulation,” Ph.D Thesis, University of Durham

[53] http://en.wikipedia.org/wiki/Force_field_(chemistry)

[54] http://www.ks.uiuc.edu/Training/Tutorials/namd/namd-tutorial-html/node25.html

[55] S. L. Altmann, A. Lapiccirella, K. W. Lodge, and N. Tomassini, “A valence force field for the silicon crystal,” J. Phys. C: Solid State Phys., vol. 15, no. 27, p. 5581, Sep. 1982.

[56] D. Camacho and Y. M. Niquet, “Application of Keating’s valence force field model to non-ideal wurtzite materials,” Physica E: Low-dimensional Systems and Nanostructures, vol. 42, no. 5, pp. 1361–1364, Mar. 2010.

[57] http://www.hsctut.materials.unsw.edu.au/Bonding/bonding4a.htm

[58] D. Lacroix, K. Joulain, and D. Lemonnier, “Monte Carlo transient phonon transport in silicon and germanium at nanoscales,” Phys. Rev. B, vol. 72, no. 6, p. 064305, Aug. 2005.

[59] Basil T. Wong, Mathieu Francoeur, and M. Pinar Menguc, “A Monte Carlo Simulation for phonon transport within silicon structures at nanoscales with heat generation”, International Journal of Heat and Mass Transfer 54 (2011) 1825-1838.

[60] Arprit Mittal, “Monte-Carlo Study of Phonon Heat Conduction in Silicon Thin Films”, PhD Dissertation Ohio State University.

[61] Q. Hao and G. Chen, “Frequency-Dependent Monte Carlo Simulations of Phonon Transport in Nanostructures,” in Applications of Monte Carlo Method in Science and Engineering, S. Mordechai, Ed., ISBN: 978-953-307-691-1, InTech, DOI: 10.5772/15475. InTech, 2011.

[62] Edwin Ramayya, "Thermoelectric properties of ultrascaled silicon nanowires," UW Madison 2010, Proquest, Umi Dissertation, 2011.

[63] S. Mazumder and A. Majumdar. Monte carlo study of phonon transport in solid thin films including dispersion and polarization. Journal of Heat Transfer, 123(4):749-759, 2001.

[64] T. I. Brown, “A Statistical phonon transport model for thermal transport in cyrstalline materials from the diffuse to ballistic regime,” Theses, May 2012.

[65] B.N. Brockhouse, Lattice vibration in silicon and germanium, Phys. Rev. Lett. 2 (6) (1959) 256–258.

[66] “Density of states,” Wikipedia, the free encyclopedia. 22-Dec-2013.

[67] Timothy M. fischer, “Thermal Energy at Nanoscale”, nanohubU, online course - http://nanohub.org/groups/u/spring2013_thermal_energy_at_the_nanoscale.

[68] Mazumder, S. and Majumdar, A., Monte Carlo study of phonon transport in solid thin films including dispersion and polarization, ASME J. Heat Transfer, 123, 749 (2001).

[69] Mark Lundstrom (2011), "Near-Equilibrium Transport: Fundamentals and Applications," http://nanohub.org/resources/11763.

[70] M.G. Holland, Analysis of lattive thermal conductivity, Phys. Rev. 132 (6) (1963) 2461–2471.

[71] Thermal conduction in doped single-crystal silicon films

[72] Asheghi, M. and Kurabayashi, K. and Kasnavi, R. and Goodson, K. E., Journal of Applied Physics, 91, 5079-5088 (2002), DOI:http://dx.doi.org/10.1063/1.1458057.

[73] A. Mittal and S. Mazumder, “Monte Carlo Study of Phonon Heat Conduction in Silicon Thin Films Including Contributions of Optical Phonons,” J. Heat Transfer, vol. 132, no. 5, pp. 052402–052402, Mar. 2010.

[74] A. Paul, M. Luisier, and G. Klimeck, “Modified valence force field approach for phonon dispersion: from zinc-blende bulk to nanowires,” J Comput Electron, vol. 9, no. 3–4, pp. 160–172, Dec. 2010.

[75] D. Vasileska, K. Raleva, and S. M., “Heating Effects in Nanoscale Devices,” in Cutting Edge Nanotechnology, D. Vasileska, Ed. InTech, 2010.

[76] A. Mavrokefalos, A. L. Moore, M. T. Pettes, L. Shi, W. Wang, and X. Li, “Thermoelectric and structural characterizations of individual electrodeposited bismuth telluride nanowires,” Journal of Applied Physics, vol. 105, no. 10, p. 104318, May 2009.

[77] M.S. Shur, R. Gaska, “Deep-Ultraviolet Light-Emitting Diodes,” IEEE Trans. Electron Devices, vol. 57, 1, pp. 164–173, 2010.

[78] Mark Lundstrom “Near Equilibrium Transport Lectures”

[79] K. Yalavarthi, S. Sundaresan, and S. Ahmed, “Multiscale modeling of wurtzite InN/GaN quantum Dot LEDs,” in 2011 11th IEEE Conference on Nanotechnology (IEEE-NANO), 2011, pp. 881–886.

[80] Afsana Sharmin “Embedded Cooling of High-Performance ICs Using Novel Nanostructured Thermoelectrics”, Thesis, Southern Illinois University Carbondale.

VITA

Graduate School
Southern Illinois University

Sasi S. Sundaresan

sasi@siu.edu

Anna University, Chennai, India
Bachelor of Engineering, May 2008

Southern Illinois University Carbondale
Master of Science in Electrical and Computer Engineering, May 2010

Special Honors and Awards:
Student Travel Award in International Workshop on Computational Electronics (IWCE) 2012

Dissertation Title:
ATOMISTIC MODELING OF PHONON BANDSTRUCTURE AND TRANSPORT FOR OPTIMAL THERMAL MANAGEMENT IN NANOSCALE DEVICES

Major Professor: Dr. Shaikh S. Ahmed

Publications:

Sasi Sundaresan, Krishna Yalavarthi, and Shaikh Ahmed, “Effects of atomicity and internal polarization on the electronic and optical properties of GaN/AlN quantum dots: Multimillion-atom coupled VFF MM-sp3 d5 s∗ tight-binding simulations,” Computational Electronics (IWCE), 2012 15th International Workshop on, vol., no., pp.1-4, 22-25 May 2012.

Krishna Yalavarthi, Sasi Sundaresan, Shaikh Ahmed, "Multiscale Modeling of Wurtzite InN/GaN Quantum Dot LEDs, "Technical Proceedings of IEEE NANO 2011 Conference (978-1-4577-1515-0/11/), August 15-18, 2011, Portland, Oregon, USA.

Sasi Sundaresan, Krishna Yalavarthi, and Shaikh Ahmed, “Electronic Structure and Optical Transitions in AlN/GaN Quantum Dots: Multimillion-Atom sp3d5s* TightBinding Modeling,” International Journal of Numerical Modeling (Submitted).

Sasi Sundaresan, Sharnali Islam, and Shaikh Ahmed, "Built-In Electric Fields in InAs/GaAs Quantum Dots: Geometry Dependence and Effects on the Electronic Structure," Technical Proceedings of IEEE Nanotechnology Materials and Devices Conferences (NMDC) 2010, October 12-15, pp. 30-35, California, USA